# Rapid Fabrication Techniques for Anatomically-Shaped Calcium Polyphosphate Substrates for Implants to Repair Osteochondral Focal Defects

by

Christina (Yi-Hsuan) Wei

A thesis
presented to the University of Waterloo
in fulfillment of the
thesis requirement for the degree of
Master of Applied Science
in
Mechanical Engineering

Waterloo, Ontario, Canada, 2007

# Author's Declaration for Electronic Submission of a Thesis

I hereby declare that I am the sole author of this thesis. This is a true copy of the thesis, including any required final revisions, as accepted by my examiners.

I understand that my thesis may be made electronically available to the public.

Christina (Yi-Hsuan) Wei

# Abstract

The purpose of the present study is to develop techniques for manufacturing anatomically-shaped substrates of implants made from calcium polyphosphate (CPP) ceramic. These substrates have tissue-engineered cartilage growing on their top surfaces and can be used as implants for osteochondral focal defect repair. While many research groups have been fabricating such substrates using standard material shapes, e.g., rectangles and circular discs, it is considered beneficial to develop methods that can be integrated in the substrate fabrication process to produce an implant that is specific to a patient's own anatomy (as obtained from computer tomography data) to avoid uneven and/or elevated stress distribution that can affect the survival of cartilage. The custom-made, porous CPP substrates were fabricated with three-dimensional printing (3DP) and computer numerically controlled (CNC) machining for the first time to the best of the author's knowledge.

The 3DP technique was employed in two routines: indirect- and direct-3DP. In the former, 3DP was used to fabricate molds for pre-shaping of the CPP substrates from two different powder size ranges (<75 μm and 106-150 μm). In the latter, CPP substrates were produced directly from the retrofitted 3DP apparatus in a layer-by-layer fashion from 45-75 μm CPP powder with a polymeric binder. The prototyped samples were then sintered to obtain the required porosity and mechanical properties. These substrates were characterized in terms of their dimensional shrinkage and density. Also, SEM images were used to assess the particle distribution and neck and bond formations. The substrates produced using the indirect-3DP method yielded densities (<75 μm: 66.28 ± 11.62% and 106-150 μm: 65.87 ± 6.12%), which were comparable to the substrates used currently and with some success in animal studies. Geometric adjustment factors were devised to compensate for the slight expansion inherent in the 3DP mold fabricating process. These equations were used to bring the plaster molds into true dimension. The direct-3DP method has proven to be the ultimate choice due to its ability to produce complex anatomically-shaped substrates without the use of a chemical solvent. In addition, it allows for precise control of both pore size and internal architectures of the substrates. Thus, the direct-3DP was considered to be superior than the indirect-3DP as a fabrication method.

In the alternative CNC machining approach to fabrication, the ability to machine the CPP ceramic was feasible and by careful selection of the machining conditions, anatomically-shaped CPP substrates were produced. To develop strategies for optimizing the machining process, a mechanistic model was developed based on curve fitting the average cutting forces to determine the cutting coefficients for CPP. These cutting coefficients were functions of workpiece material, axial depth of cut, chip width, and cutter geometry. To explore the utility of this modelling approach, cutting forces were predicted for a helical ball-end mill and compared with experimental results. The cutting force simulation exhibits good agreement in predicting the fundamental force magnitude and general shape of the actual forces. However, there were some discrepancies between the predicted and measured forces. These differences were attributed to internal microstructure defects, density gradients, and the use of a shear plane model in force prediction that was not entirely appropriate for brittle materials such as CPP.

The present study successfully developed 3DP and CNC fabrication methods for manufacturing anatomically-shaped CPP substrates. Future studies were recommended to explore further optimization of these fabrication methods and to demonstrate the utility of accurate substrates shapes to the clinical application of focal defect repair implants.

# Acknowledgements

I would like to take this opportunity to acknowledge the support of a number of individuals without whom this thesis would not have been possible. I would like to thank my supervisors, Dr. Ehsan Toyserkani, Dr. Kaan Erkorkmaz, and Dr. John B. Medley not only for giving me a once in my lifetime opportunity to go further distance, but for their guidance and insight throughout this project, as well as their enthusiasm for research. As well, I wish to thank my examination committee, Dr. Fathy Ismail and Dr. Naveen Chandrashekar for their time and insight.

I would also like to express my sincere appreciation to our collaborators, Dr. Pilliar, Dr. Kandel, and Dr. Grynpas at the University of Toronto for the opportunity to take on an exciting project. Many individuals have contributed their time and expertise during different phases of this study. In particular, I would like to show my gratitude to Robert Wagner for all his knowledge and invaluable wisdom on machining; Dr. Yuquan Ding for SEM imaging; Svitlana Prada, Dr. Lu Gan, and Dr. Jason Hung for their assistance on sintering. They were always supportive and took time from their busy schedule to help me out.

I would like to express thanks to every individual in my research group for friendship and support. My peers and colleagues have been of significant importance to me and they have provided an enjoyable social atmosphere in the lab. My mechie and chemie friends, thank you all for your support and friendship. I would not be able to do this without you guys.

In closing, I would like to dedicate this thesis to my family who have supported me through more than two decades of my academic career. Their love and persistent support have always been my inspiration to achieve my goals. Lastly, I could not complete this thesis without plentiful support and love from Harry Leung, thank you!

# Table of Contents

# List of Figures

# List of Tables

# Nomenclature

| | |
|---|---|
| $a$ | Axial depth of cut |
| $\beta$ | Helix angle |
| $c$ | Feed per tooth |
| $D$ | Cutter diameter |
| $F_t(\phi)$, $F_r(\phi)$, $F_a(\phi)$ | Tangential, radial, and axial cutting force acting on the cutting edge |
| $\overline{F_{\mathrm{x}}}$, $\overline{F_{\mathrm{y}}}$, $\overline{F_{\mathrm{z}}}$ | The average cutting force per tooth period in the x-, y-, and z-direction. |
| $F_x$, $F_y$, $F_z$ | The total force in the feed (X), normal (Y), and axial (Z) direction. |
| $h$ | Instantaneous chip thickness |
| $K_{\mathrm{tc}}$, $K_{\mathrm{rc}}$, $K_{\mathrm{ac}}$ | Milling shear component of cutting force coefficients in tangential, radial, and axial directions |
| $K_{\mathrm{te}}$, $K_{\mathrm{re}}$, $K_{\mathrm{ae}}$ | Milling edge component of cutting force coefficients in tangential, radial, and axial directions |
| $N$ | Number of flutes |
| $\phi$ | Angular immersion of the cutting edge |
| $\phi_p$ | Cutter pitch angle |
| $\phi_{\mathrm{st}}$ | Start angle of a cut |
| $\phi_{\mathrm{ex}}$ | Exit angle of a cut |

# Chapter 1

# Introduction

## 1.1 An Implant Concept

Synovial joints of the body can withstand an astonishing amount of repetitive applied load and motion. Even though joints are susceptible to many problems including injuries, structural degradation, and diseases, they usually serve the body well throughout a long lifetime of use. If the articular surface of a synovial joint, namely the articular cartilage, is damaged, function can be permanently impaired because articular cartilage has limited self-repair capacity [1][2]. When the damaged area exceeds a critical size, the healing process fails and osteoarthritis destroys the joint. This long-term joint deterioration can be treated by a surgical procedure known as total joint arthroplasty. In this procedure, the synovial joint surfaces are replaced with implant components fabricated from metal, ceramic, and polymer materials that are inert and, in bulk, biocompatible. Total joint arthroplasty has allowed millions of people with severely damaged joints to live longer and more active lives. However, in terms of function, even the most reliable implants have been shown to suffer inadequacies. For a group of patients receiving total hip replacement from 1986 to 1995, Söderman *et al.* [3] reported clinical failure rates as high as 20% after 10 years. In this study, clinical failure was defined as poor outcomes according to scoring systems as well as revision surgery.

The invasive nature of total joint arthroplasty, the reported relatively high clinical failure rates at 10 years, and the potential need for subsequent revision surgery have motivated efforts to develop new treatment strategies. One such approach involves the concept of osteochondral focal defect repair using tissue-engineered cartilage anchored in the subchondral bone by a biodegradable substrate that serves as a template first for *in vitro* tissue generation then for the *in vivo* defect repair (Figure 1-1). This approach to repair defects introduces the potential advantages for early joint restoration before the often inevitable progression to severe osteoarthritis [4][5]. During the past decade, a number of important studies have been completed to investigate this novel approach [5][6][7][8]. As demonstrated in a recent animal study [5], focal defects have been repaired with some success using 4 mm diameter biphasic implants consisted of *in vitro*-formed cartilage on porous biodegradable calcium polyphosphate (CPP) bone-substituting substrates. The implants appeared to be securely integrated in the femoral condyles of sheep knees by 3 months and remained intact for periods up to 9 months. Tissue engineered implants may represent a new paradigm in restoring joint function.

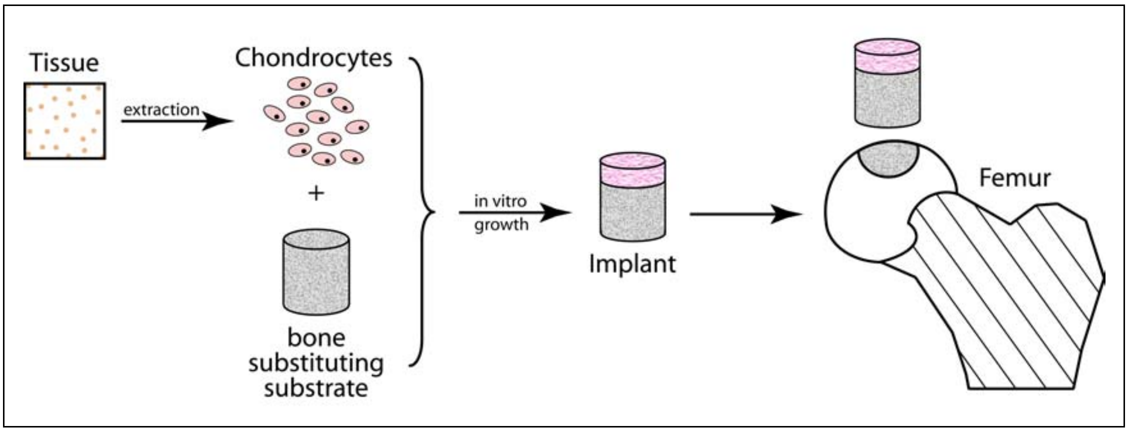

Figure 1-1: Tissue engineering approach for repairing an osteochondral focal defect in the cartilage of a synovial joint.

The present thesis is based on an on-going collaboration with a research team at the University of Toronto which is investigating and developing the above approach to repair osteochondral focal defect [4][5] as explained subsequently.

## 1.2 Bone Substituting Substrates

The bone substituting substrates is one of the key components of the tissue engineering treatment of focal defects mentioned above. Various materials have been developed and used to repair bone defects. In general, these materials can be differentiated into those that are derived from naturally occurring materials and those that are manufactured synthetically.

Currently, the most extensively used natural bone substitutes are autografts and allograft. An autograft (or autogenous bone graft) is tissue transplanted from one part of the body to another part in the same individual [9]. This approach eliminates the problem of host rejection and disease transmission but it is limited in availability and causes damage at the harvesting site. This can cause increased patient recovery time, local sensory loss, mobility restriction, and lead to chronic pain. In addition, there may not have sufficient bone of suitable quantity to meet the need [9].

Allograft is the tissue taken from one individual (often deceased) and transplanted into another individual [9]. This method is particularly useful when the defect is large and requires more structural support [10]. Allograft is available from “bone banks” and this simplifies surgery compared with autograft. However, it increases the risk of disease transfer and tissue rejection due to adverse immune response [11].

The limitations of autograft and allograft suggest the need to have alternative treatment methods. A variety of *synthetic* bone grafts have been developed to fill bone defects. Lewandrowski *et al.* [12] noted that 10% of bone graft procedures performed in the United States used a synthetic material. The ideal synthetic bone graft should be:

- *Biocompatible and non-toxic* to minimize chronic immune response from the host site.
- *Biodegradable* at a specific and predicable rate so that it can eventually be replaced by newly formed bone tissue [13]. This is facilitated by an open-pore structure with pore size ranging form 100 to 300 μm to allow bone ingrowth [14].

- *Functionally weight-bearing* to withstand applied loads during early post-implantation period and before sufficient bone ingrowth and replacement [13].
- *Mechanically compatible* to have sufficient strength, elastic modulus, and fracture toughness to function in place of the cancellous bone it replaces [10]. The strength can vary over a considerable range. For example, Bartel *et al.* [15] has reported that the strength of the cancellous bone of the femur is between 0.56 to 22.9 MPa.
- *Osteoconductive* to allow bone to "communicate" and grow over its entire surface [10].
- *Osteoinductive* in that it can induce differentiation of pluriopotential stem cells to an osteoblastic phenotype [10].
- *Osteointegrative* in that it can chemically bond to the surface of the bone without forming an intervening fibrous tissue layer [10].
- *Osteogenesis* in that it can form new bone from osteoblastic cells present within the graft material [10].
- *Readily available* in large quantity.

Calcium polyphosphate has been considered as a promising synthetic bone substitute material by a research team at the University of Toronto [13][16]. With a chemical composition similar to bone mineral, CPP exhibits superior biocompatibility and is well accepted by the host body [16]. It demonstrates good degradation characteristic due to its dissolution property in biological environment [17]. Furthermore, with appropriate selection of sintering conditions, starting powder particle sizes, and degree of polymerization, the degradation characteristic can be tailored and controlled [13][17]. This material has proven to be osteoconductive in that it allows rapid bone formation [13]. In addition to the mentioned benefits, CPP has been used in the development of tissue-engineered cartilage [18] where chondrocytes are able to maintain their phenotype and form cartilaginous tissue on porous CPP substrates [19].

## 1.3 Surface Geometry of Substrates

Tissue engineering involves the reconstruction of living tissues. Hung *et al.* [20] reported successful cartilage reconstruction using tissue engineering for a specific pre-determined shape [20]. They documented the *in vitro* cultivation of anatomically-shaped bilayered constructs consisted of anatomically-shaped trabecular bone blocks with chondrocyte cell-laden agarose *in vitro*. Despite the use of relatively large implant (area = 1170 $cm^2$), Hung *et al.* reported success in maintaining the chondrocytes to remain firmly on the bony substrate. Chen *et al.* [21] regenerated bone graft in the shape of a human mandibular condyle by seeding marrow-derived osteogenic cells in natural coral scaffolds and implanted them into nude mice. Different biopolymers, including poly $_{\text{DL}}$-lactic-co-glycolic acid (PLGA) [22], polyethylene-glycol-based hydrogel [23], and poly-$_{\text{L}}$-lactice acid (PLA) [24], were used to tissue engineer bone in the shape of the mandibular condyle *in vitro* and *in vivo* from mesenchymal stem cells that act as osteogenic supplements. This method proposed a better treatment method in the clinical setting where stem cells could be harvested from a patient’s own body and cultured on an engineered bony substrate for implantation back into to the patient’s body.

Information on the importance of surface geometry of the bone graft material on cartilage survival in focal defect repair is negligible or proprietary, and still requires further investigation [21]. Although Kandel *et al.* [5] report success in their studies of a focal defect repair implant in a sheep model; they have noted that the geometric mismatch, as a result of implant shape and placement between the implant substrate and the surrounding articular cartilage seems to be related to cartilage erosion in some repairs (Figure 1-2). It is likely that the erosion occurred because the cartilage tissue was sensitive to the elevated contact stresses at the mismatched edges. Additionally, the low cartilage-to-CPP interfacial shear strength compared with the native osteochondral interface contributes to cartilage erosion [25] and this problem will be made more acute by a poor surface geometry. Thus, it is likely to be biomechanically desirable to blend the surface of the implant substrates at the recipient site with the surrounding subchondral bone surface to achieve the most normal stress environment [26].

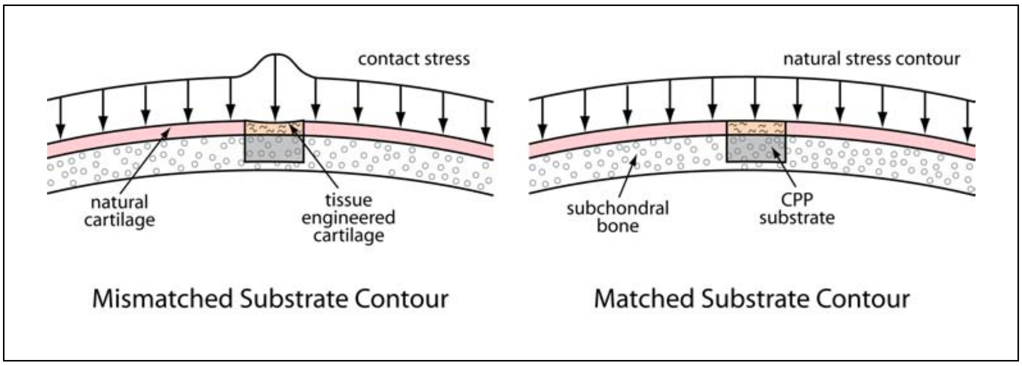

Figure 1-2: Elevated stress distribution as a result of implant geometry mismatch.

## 1.4 Objectives of the Thesis

The current study is an initial development of methods to manufacture anatomically-shaped bone-substituting substrates of implants from calcium polyphosphate (CPP) bioceramics specifically for the previously mentioned research team at the University of Toronto. The primary objective is to investigate two fabrication technologies: three-dimensional printing (3DP) and computer numerically controlled (CNC) machining.

## 1.5 Outline

The present thesis is organized in the following order. In Chapter 2, background information on calcium phosphate ceramics is first introduced. Following that, a review of literature on rapid prototyping (RP) and CNC machining is presented by beginning with a general overview on process and applications. Subsequently, contributions of each technology to biomedical engineering, particularly the bone-substituting substrates are discussed. Chapter 3 describes the material preparation, methodology, and the experimental results of the two rapid prototyping methods employed to fabricate CPP substrates. The first method, indirect-3DP involves the use a negative mold made with 3DP whereas in the second method, CPP substrates are fabricated directly from the 3DP apparatus. This chapter also includes an investigation into the dimensional accuracy of the fabricated molds that can be achieved using the 3DP apparatus. In Chapter 4, the CNC machining of CPP is described including both setup and data acquisition. Then, a mechanistic model is presented that can be used to predict cutting forces. Lastly, Chapter 5 offers conclusions and recommendations for future work.

# Chapter 2

# Literature Review

## 2.1 Calcium Phosphates for Synthetic Bone Substitutes

Due to growing interests and needs for synthetic bone substitutes, a considerable amount of research has been devoted to the development and characterization of suitable biomaterials. The most widely investigated synthetic bone substitutes can be categorized into two groups: bioceramics and biopolymers [10]. Bioceramics are the best choice for many applications including tissue engineered focal defect repair implants because of their high compressive strength. Bioceramics can be further classified as nonresorbable (relatively inert), bioactive (semi-inert), and biodegradable (resorbable) [29]. Nonresorbable bioceramics include fully dense or porous $Al_2O_3$, $ZrO_2$, and $Si_3N_4$. This type of ceramic remains permanently in the host body upon implantation and is often required to provide structural support in applications such as femoral heads, bone plates, and bone screws. In addition, they can be used in non-structural support applications such as sterilization and drug delivery devices [29]. Bioactive semi-inert ceramics include fully dense glass ceramics, bioglass, and fully dense hydroxyapatite. Upon implantation, they form strong bonds with the adjacent tissue and so one of the major applications of these bioactive semi-inert ceramics is in surface coating of metallic implants to develop bone ingrowth fixation. However, due to the brittleness of these materials, delamination is a recurring problem. Biodegradable or resorbable ceramics, as their name suggests, degrade upon implantation with the intention that they will be replaced by natural bone tissues. This type of ceramics is often made from calcium phosphates.

Biodegradable ceramics are often preferred because they leave a natural bone structure and do not stay around to permanently alter stress distribution and influence adjacent bone integrity. Bone typically consists of 25% water, 15% organic material, and 60% mineral by weight [30]. The mineral portion consists mainly of calcium and phosphate ions, with traces of magnesium, carbonate, hydroxyl, chloride, fluoride, and citrate ions. Due to its chemical composition, calcium phosphate (CaP) ceramics appear to be the most biocompatible synthetic materials available. There are a large number of CaP ceramics (Table 2-1). These ceramics are non-toxic and the degradation products are simply calcium and phosphate ions, which are well tolerated and eliminated the possibility of an inflammatory response to the host body.

Table 2-1: Calcium phosphate ceramics family [30].

| Ca : P | Chemical Formula | Chemical Name | Mineral Name |
|---|---|---|---|
| 0.5 [35] | $Ca(PO_3)_2$ | Calcium polyphosphate | --- |
| 1.0 | $CaHPO_4$ | Dicalcium phosphate (DCP) | Monetite |
| 1.0 | $CaHPO_4 \cdot 2H_2O$ | Dicalcium phosphate dehydrate (DCPD) | Brushite |
| 1.33 | $Ca_8(HPO_4)2(PO_4)_4 \cdot 5\ H_2O$ | Octocalcium phosphate (OCP) | --- |
| 1.43 | $Ca_{10}(HPO_4)(PO_4)_6$ | --- | Whitelockite |
| 1.5 | $Ca_3(PO_4)_2$ | Tricalcium phosphate (TCP) | --- |
| 1.67 | $Ca_{10}(PO_4)_6(OH)_2$ | --- | Hydroxyapatite |
| 2.0 | $Ca_4P_2O_9$ | Tetracalcium phosphate | --- |

CaP ceramics have been demonstrated to exhibit osteoconductive capability when implanted in bone [30]. Several research groups have shown the clinical success of using CaP ceramics to repair bony defects [31][32][33][34]. However, they do have relatively low strength, fracture toughness, and fatigue resistance [30]. As a result, they are not appropriate for many weight-bearing applications particularly those involving torsional or tensile stresses imposed to the body [9].

The chemical composition, degree of crystallization, and porosity all contribute to the physical characteristics of the bone substitute implant *in vivo*. The degradation of CaP ceramics when in contact with the biological milieu is governed by a two-step process: physicochemical dissolution followed by disintegration of bulk implant into small particles [36][37]. The physical changes can cause reduction in density and changes in substrate size and shape. The chemical changes can include elevation of calcium and phosphate ions in the surrounding milieu and changes in the pH level. The overall rate of physicochemical dissolution depends on several factors such as surface area per unit weight of the material, crystallinity of the material, solubility and the extent of changes in both pH and chemical composition of the incubating fluid.

Denser crystalline structures can be obtained for CaP ceramics by altering the sintering parameters. Sintering is a heat treatment process that causes powder particles to fuse together by means of a solid-state diffusion (Figure 2-1). Depending on the sintering time and temperature plus the particle size distribution, a porous or fully dense shape can be produced [36]. For example, a less porous (more dense) crystalline structure can be obtained by applying a higher temperature and longer dwell time during sintering. Also, the extent of crystallization has a remarkable effect on the strength and the degradation characteristic of the bone substitutes. With both a higher density and a higher extent of crystallization, the substrates exhibit improved mechanical strength but they undergo a slower degradation process [9][35].

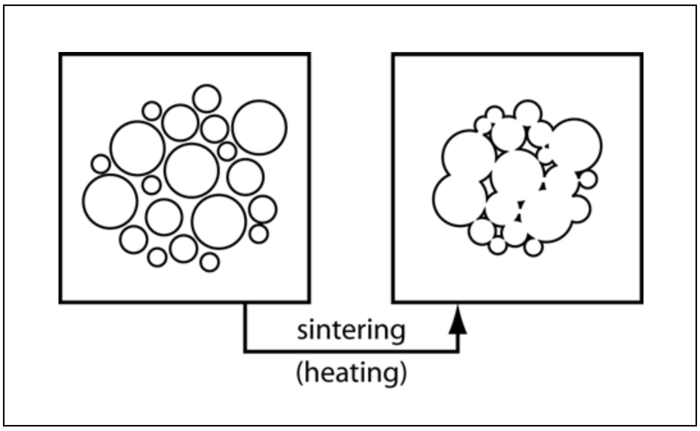

Figure 2-1: Simplified process of sintering particles as adopted from van Noort [38].

The surface area per unit weight of the material has a strong correlation with microporosity. These open pores are desirable in the interior of the bone substitutes to encourage new bone formation. The number of open pores can be determined by controlling the sintering temperature and/or the sintering time [37]. At higher temperatures and longer sintering times, the degree of microporosity decreases. As the degree of porosity increases within the internal architecture of the substrate, the surface area exposed to the degradation media is also increased. It has been mentioned previously that the CaP ceramics can have insufficient mechanical properties in some applications and with the addition of open pores, the mechanical properties are further reduced. Two of the most widely used CaP ceramics are hydroxyapatite and tricalcium phosphate. Also, there has been a recent interest in calcium polyphosphate.

### *Hydroxyapatite*

The primary crystalline component of the bone is hydroxyapatite (HA) and with a chemical formula of $Ca_{10}(PO_4)_6(OH)_2$, it can be classified as a calcium phosphate bioceramic. Specifically, it is a member of the calcium orthophosphates family and it has relatively high calcium to phosphate ratio of 1:1.67 [13]. This material has become available in the 1970s where it was used as dental implants, void fillers, and in maxillofacial reconstruction [10]. More importantly, it began to be used as a bioactive coating to enhance chemical bonding for orthopaedic, dental, and maxillofacial prostheses [10][30].

The commercial methods to prepare HA are by aqueous precipitation of a calcium salt and an alkaline phosphate or calcium hydroxide or conversion from calcium hydroxide or calcium carbonate and phosphoric acid [29][30]. Other methods are also available to prepare HA, which include solid-state reactions, hydrolysis, and hydrothermal conditions [39]. HA ceramics remain more permanent in the host body. They are known to be osteoconductive but lack intrinsic osteogenic potential [9].

*Tricalcium Phosphate*

According to Tas *et al*. [40], tricalcium phosphate (TCP), represented by the chemical formula $Ca_3(PO_4)_2$, is the most common resorbable calcium phosphate and its stoichiometry is similar to the amorphous biologic precursors of bone [9]. TCP is also a member of the calcium orthophosphates family and it has a calcium to phosphate ratio of 1:1.5 [30]. TCP has been used as a bioactive coating to provide a mechanical interlock with ingrown bone for titanium prostheses [41]. This material has also been used in the form of bone substitute with approximately 35 to 50% porosity and pores ranging from 100-300 μm [9].

Tricalcium phosphate exists in two different phases, beta-tricalcium phosphate (β-TCP) and alpha-tricalcium phosphate (α-TCP). β-TCP is stable up to 1120°C and α-TCP is stable up to 1470°C [42]. The difference in calcium to phosphate ratios, resulting in differences in degradability, has set TCP apart from HA [43].

### 2.1.1 Calcium Polyphosphate

There has been a recent interest [13][16][17] in a member of the condensed phosphate family known as calcium polyphosphate (CPP) that has a chemical formula of $[Ca(PO_3)_2]_n$. It has a calcium to phosphate ratio of 0.5 and is formed by repeated condensation of oxygen bridge phosphate tetrahedral $(PO4)^{3-}$ group into a linear chain network structure [13]. CPP powder can be randomly arranged to produce amorphous phosphate glasses or crystalline structures depending on the processing parameters and the starting components used. The theoretical full density of CPP is 2.85 $mg/mm^3$ [13].

CPP glass powder can be prepared according to methods described by Pilliar *et al.* [13]. The initial procedure is to calcine (to heat a substance so that it oxidizes or reduces) the precursor powder, calcium phosphate monobasic monohydrate, $Ca(H_2PO_4)_2 \cdot H_2O$, at 500°C for 10 h in an air furnace to produce CPP through the following chemical reaction,

$$n\ \mathrm{Ca(H_2PO_4)_2}\text{廈}_2\mathrm{O} \xrightarrow{500\ ^\circ\mathrm{C}} [\mathrm{Ca(PO_3)_2}]_n + 3n\ \mathrm{H_2O}$$

The resulting powder is then melted at 1100°C to produce an amorphous glass and held under the same temperature for 1 h to induce chain lengthening [35]. The molten CPP is then quenched in distilled water to be rapidly cooled in order to form an amorphous frit. This frit is milled and screened to produce CPP powder in different particle sizes. The porous CPP substrates are prepared by gravity sintering. Using the standard protocol, the 75-106 μm powder is poured into cylindrical platinum molds followed by light shaking to assist in packing the powders without causing any significant separation of different powder size fractions. Final porous structures are produced by sintering the samples at 950°C for 2 h in an air muffle furnace at a heat-up rate of 10°C/min. Under this protocol, the samples have approximately 35 to 40 vol% porosity, interconnected pores in the 100 to 250 μm range, and an average pore size of 75 μm [13][18][44]. A diamond wafering blade is then used to cut the CPP rods into required length for subsequent experiments.

Back in the 1960s, the hydrolytic degradation of glassy calcium polyphosphate was investigated by Brown *et al.* [45] and Huffman and Fleming [46]. These investigations were conducted to explore the potential use of various condensed CaP ceramics as fertilizers [47]. The solubility of CPP in aqueous-based solution is fairly low [46]. Nevertheless, it is subject to hydrolysis degradation upon contact with water [48]. In pure aqueous media, the rate of degradation depends on the specific phosphate being considered, as well as the pH level, temperature, and concentration of the media [48].

CPP shows potential as a material for biodegradable synthetic bone substitute applications [4][5][13][14][16]. Studies have been conducted on their biocompatibility, rate of degradation, and the extent of bone ingrowth *in vitro* [13] and *in vivo* [49]. The crystalline structure CPP demonstrates degradability that is fourfold that of the amorphous CPP [35]. According to Baksh and Davies [16], three-dimensional (3D) scaffolds with interconnected macropores can be fabricated using a polyurethane sponge method within the structure. They have reported bone ingrowth in both *in vitro* and *in vivo* studies, thus demonstrating that CPP can be used successfully for bone scaffolds.

In addition, cartilage tissue can be formed on CPP substrates and has been tested in *vitro* [18] and upon mechanical stimulation [50][51]. These results show the ability of chondrocytes to maintain their phenotype and form cartilaginous tissue when cultured on porous CPP substrates [19]. Most recently, Kandel *et al*. [5] have studied the biochemical and biomechanical properties along with the morphology of in *vitro*-formed biphasic constructs 3 and 9 months after the implantation in sheep models. The mechanical properties of the cartilage improve significantly after implantation suggesting that cartilage can mature *in vivo* after implantation. These investigations confirm the potential of calcium polyphosphate to be used as a bone-substituting substrate for a tissue engineered implant for focal defect repair.

## 2.2 Rapid Prototyping

In recent years, intensive research have been concentrated on the additive rapid prototyping (RP) or solid freeform fabrication (SFF) processes, in which 3D objects are built by successively layering of two-dimensional (2D) slices of a solid as shown in Figure 2-2. The specific RP methods include stereolithography (SLA), selective laser sintering (SLS), three-dimensional printing (3DP), and fused deposition modeling (FDM). These technologies are fundamentally different from traditional subtractive methods such as milling, grinding, and drilling where materials are removed to achieve desired objects. With the introduction of new materials and processes, these RP methods have been contributing to many applications such as investment casting, tooling design, anatomical models, surgical implant prototyping and various other reconstructive surgery aids [52].

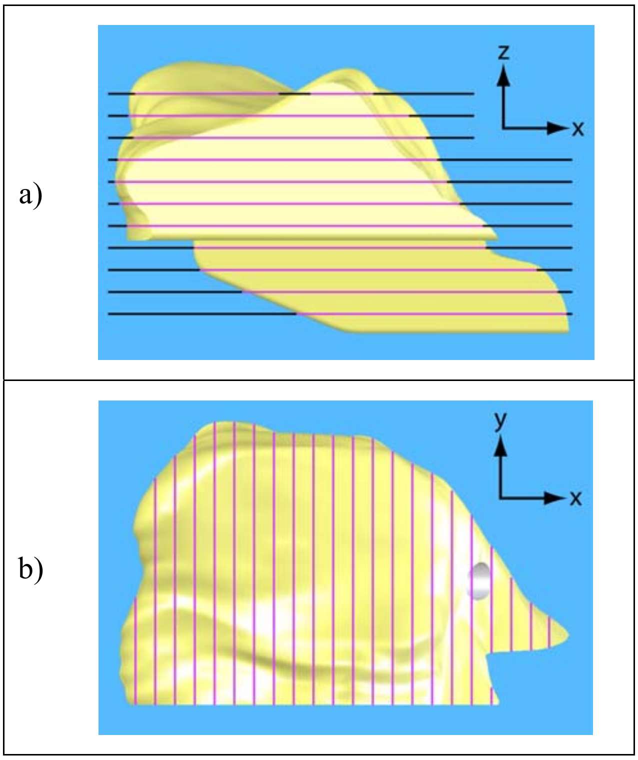

Figure 2-2: Two-dimensional slicing algorithm and working principle of rapid prototyping. a) sliced layers in the z-direction of predetermined thickness and, b) trajectories in the x-y plane.

The fundamental process of RP begins with sectioning a 3D object of computer-aided design (CAD) model into 2D cross-sectional layers of predetermined thickness (Figure 2-2a) followed by paths generated in the x-y plane (Figure 2-2b). This geometric information is then transferred to the RP apparatus to produce the physical model. The object is formed from the bottom to the top by incremental material built-up of the cross-sectional layers and the use of a laser beam or a binder injection system. Post processing may require the removal of temporary supporting structures.

The main advantages of RP include the opportunity to create complex objects with conformal passages from a CAD model faster and usually at a lower cost than conventional methods. Without much human intervention during the operation, precision parts can be produced. RP technologies can also be used to create three-dimensional models that have been beneficial to different industries for product development in three aspects: design engineering, manufacturing, and marketing [53]. Design engineers can visualize and thus work towards optimizing a design, thus reducing model iteration and developing time. In terms of manufacturing, a physical model made by RP methods from a prototype material can speed up the final product's process planning and tooling design, as well as avoiding misinterpretation of blueprint on the shop floor. Furthermore, sales consultant can utilize the model to demonstrate the design concept and the feasibility of the design, and also gain customers' feedback on the design.

## 2.3 Rapid Prototyping for Tissue Engineering Scaffolds

The development of RP for fabricating biomedical engineering devices has become an escalating field of research during the last several years. Its diversified potential is very attractive to industry. Complex parts that have conformal passages and heterogeneous properties can be made quickly with zero wastage of material. These medical devices can be categorized into external and internal. The external devices include those that are in contact with the human body including hearing aid shells and dental fixtures such as crowns, caps, and bridges. These devices are often cast from RP-fabricated molds made to have the negative impressions of the desired objects. Mass customization is possible such as the Invisalign orthodontic custom braces by Align Technology Inc., which has been reported to have treated more than 100,000 patients [54]. In this process, the company uses stereolithography to make the orthodontic devices from impressions obtained by dentists.

While the external devices benefit from the capabilities of RP, the internal devices are another market that can profit from custom shape fabrication. The internal devices include permanent surgical implants, degradable tissue engineering scaffolds, and regenerated tissues. Particularly in the permanent implant market, namely orthopaedic implants including those used in craniofacial joint and spinal reconstruction, there is a requirement to design and manufacture directly from medical images such as computer axial topography (CAT) or magnetic resonance imaging (MRI). Rapid prototyping can also be used as a preoperative planning tool, in which the physical model of a impaired area can be built and used for guidance during surgery [55][56]. Also, such models can be used in patient education and surgeon training.

In recent years, RP methods have been receiving a great interest to construct porous tissue-engineered scaffolds using synthetic biomaterials. RP is clearly the primary candidate for fabricating these scaffolds due to its ability to rapidly fabricate complex exterior geometry and porous internal microstructures [54][57]. It offers a means to precisely control the matrix architecture, including size, shape, geometry, orientation, interconnectivity, and branching. As a result, RP can provide a biomimetic structure with various design and material composition features that enhance the mechanical properties, biological responses, and degradation characteristics of the scaffolds [57]. According to Hollister and Bergman [54], these "scaffolds represent the most risky, but at the same time most exciting venture with the largest potential payoff for biomedical integrated additive/subtractive manufacturing applications over the next 10 to 30 years". The following sections discuss three different RP methods that have been used for making tissue engineering scaffolds.

### 2.3.1 Stereolithography

Stereolithography (SLA) was presented by Hull [58] and later described as the first commercialized RP technology [59] (introduced in 1988 by 3D Systems Inc., Rock Hill, SC, USA, www.3dsystems.com). In this process, a low-power ultraviolet (UV) light is used to scan over a bath of liquid photo-polymeric resin following the cross-sectional profiles carried by computer slice data. The UV light causes polymerization and creates a solid plastic layer at, and just below the surface of the bath. This process is repeated in a line-by-line and layer-by-layer sequence to create the desired object [59]. Once the process is completed, the platform is raised out of the vat to allow draining of excess liquid. The part is then cured in a UV oven and finished by smoothing the surface irregularities. The accuracy achieves by SLA is approximately 0.1% of the overall dimension, however, when the size of the object increases, the accuracy deteriorates up to 0.5% [53].

A number of research groups fabricated polymer-based scaffolds using SLA. Cooke *et al.* [60] reported success in producing constructs having an overall dimension of 50 mm in diameter and 4 mm in thickness with well-defined holes, slots, and protrusions. These constructs were made from polypropylene fumarate (PPF) could potentially be used as 3D biodegradable scaffold for bone ingrowth [60][61]. Matsuda and Mizutani [62] demonstrated the feasibility of using SLA to build such a scaffold using a novel biodegradable acrylate copolymer endcapped with poly-ε-caprolactone-co-trimethylene carbonate. They were able to produce a microtubes with an inner diameter of 2.0 mm, a width of 0.2 mm, and a height of 5.0 mm. Porter *et al.* [35] formulated suspensions of calcium polyphosphate and photosensitive monomer for forming constructs using SLA. These substrates were then sintered at 585°C or 600°C for 1 h to yield an amorphous or crystalline structure, respectively. It was observed that with a sintering temperature of 600°C, the constructs exhibited a superior bend strength and toughness with an average porosity of 22.9%. However, they did not investigate the prototyping of complex CPP substrates and there was no report on the process parameters used for the RP machine.

### 2.3.2 Selective Laser Sintering (SLS)

Selective laser sintering (SLS) was first developed by Deckard and Beaman [53] and commercialized by DTM Corporation (Austin, TX, USA, www.dtm-corp.com). SLS begins with powder deposition onto the surface of the work platform by a levelling drum or a counter-rotating roller mechanism. As shown in Figure 2-3, the workspace is usually heated to just below the glass transition temperature of the powder to minimize thermal distortion and assist fusion [63]. In addition, the workspace is filled with an inert gas to avoid oxidation and burning of the powder [64]. During SLS, a carbon dioxide ($CO_2$) laser selectively scans over the surface of the workspace by galvanometer driven mirrors in the x/y pattern, following the 2D design boundary of an object. Upon activation of the laser, the temperature of the powder rises just above its glass transition temperature, thus causing the powder particles to bond. Subsequent layers are built directly on the previous sintered layer after new layer of powder are deposited. The powder that is not scanned by the laser remains in place and serves as a support, which reduces distortion of the scaffold. The average accuracy ranges from ±0.13 mm to ±0.38 mm for a part with a diameter of 305 mm and a height of 381 mm [53].

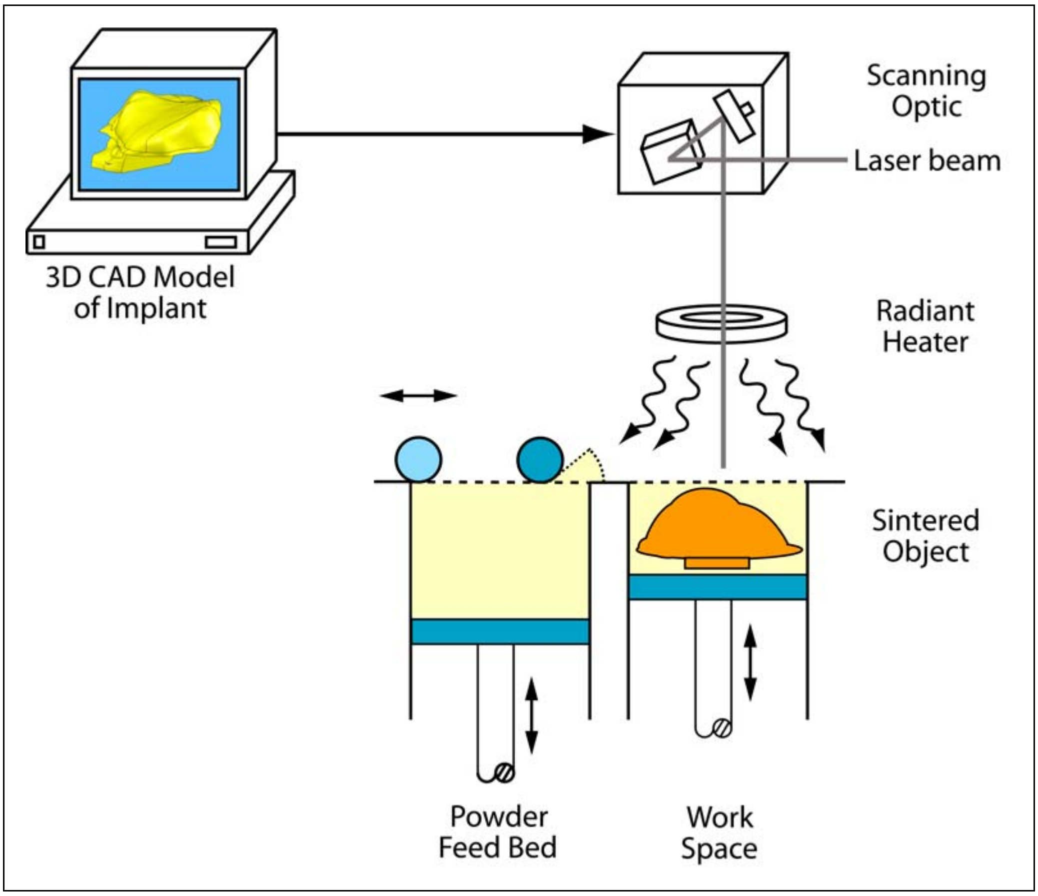

Figure 2-3: Schematic layout of SLS.

From the research done on SLS in the medical field, material selection included ceramic with polymeric binder [65][66], pure polymer with or without bioactive cells [67][68][69], and pure polymer [70] For ceramic with a polymer binder, Vail *et al*. [65] reported SLS fabrication of an implant with a diameter of 8.9 mm and a height of 8.9 mm from calcium phosphate ceramic powder and poly(methyl methacrylate-co-n-butyl methacrylate) copolymer. The copolymer, with a low glass transition temperature, melted first upon laser activation and served as an adhesive to bond the ceramic powder particles into a contiguous object during processing. These implants were tested in pre-clinical trials in dogs. Histological evaluation suggested that mineralized bone was formed in the macro pores of the implant and the change in implant contour indicated implant degradation and bone resorption.

For pure polymer SLS, a biopolymer such as polyetheretherketone (PEEK) [67], polycaprolactone (PCL) [68], or polyvinyl alcohol (PVA) [69] could be blended with a bioactive cell such as hydroxyapatite (HA) to stimulate bone ingrowth. The scaffolds fabricated by Williams *et al.* [68] possessed mechanical properties within the lower range of trabecular bone, thereby suggesting that they might be able to withstand loading upon implantation. In addition, they demonstrated the feasibility to fabricate complex scaffold in the shape of a mandibular condyle. Rimell and Marquis [70] have reported the use of polymer powder, ultra high molecular weight polyethylene (UHMWPE) as the third scenario. UHMWPE is widely used for producing many of the current implant devices and is also readily available in powder form. Consequently, it was hypothesized to be a good material candidate. They observed that solid liner continuous bodies could be fabricated, but material shrinkage occurred when a sheet-like structure was desired. In addition, the porosity of the structure formed and degradation kinetics were concerns that needed to be solved in order to apply SLS to the fabrication of UHMWPE devices [70].

### 2.3.3 Three-Dimensional Printing

Three-dimensional printing (3DP) is one of the latest and vastly-expanding techniques in the RP industry. It came into the foreground as a very competitive process due to its flexibility, precision, and the sub-millimetre fine feature it can provide [52][71][72]. This “powder-based additive” approach offers remarkable flexibility in part materials and geometry. The 3DP process was invented by Emmanuel Sachs and Michael Cima at the Massachusetts Institute of Technology (MIT) laboratory [31][73] and was licensed to different companies for further development of variety of printers.

Three dimensional printing is an additive process in which 3D objects are built in a layer-by-layer fashion from a CAD file. As shown in Figure 2-4, a 3DP machine consists of three subsystems: a raw binder injection system, a particle delivery system, and a positioning system [74]. The build compartment is usually heated to assist fusion of the powder particles. During 3DP, the ink-jet printhead selectively deposits the liquid binder onto the surface of the workspace, following the contour as defined by the 2D sliced data. The interaction of the binder with the powder particles causes the particles to bond to each other and to the printed cross-section one level below to form a solid mass. Subsequent layers are then built directly on top of the previously layers after new layers of powder are being deposited by a roller. This process is repeated until the part is completed. Once the part is completed, the unbound powder particles are removed by an air jet. The finished part can be infiltrated with substances such as wax or superglue.

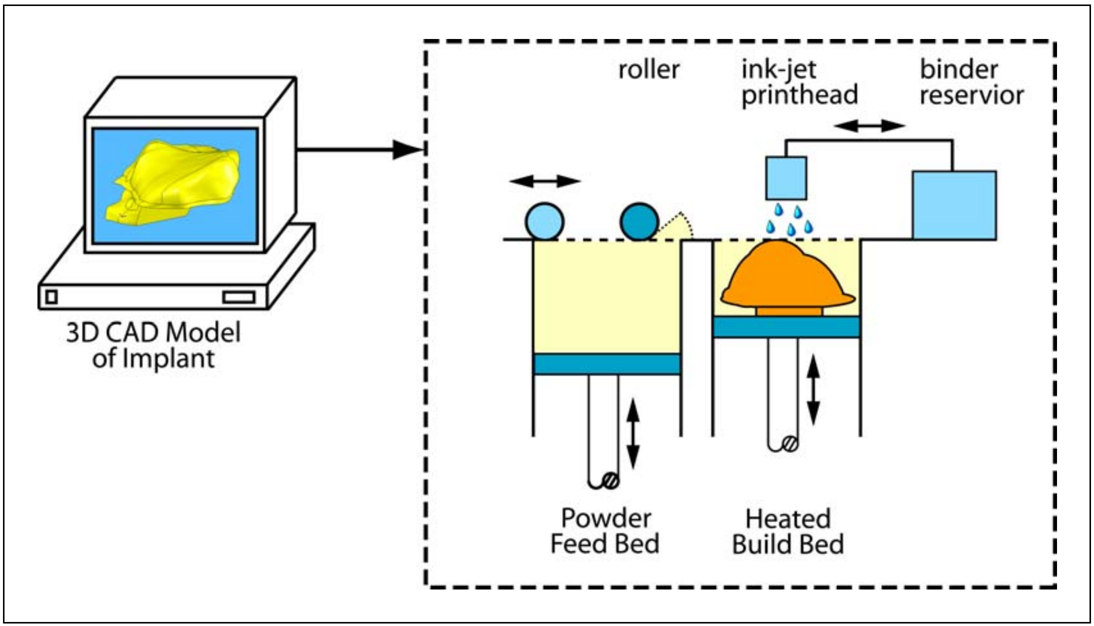

Figure 2-4: Schematic layout of 3DP.

Several different 3DP systems are available commercially and can be categorized by the powder and ink material as shown in Figure 2-5 [75]. Generally, the process is classified by the binder used in the powder bonding process, which can be incorporated either i) in the aqueous ink or ii) blended with the powder. In the first category, the binder in ink systems can be employed for two types of powders: ceramics [71] or metal [75]. The binder can be inorganic such as colloidal silica or organic such as polymer resin or an emulsion (latex or acrylic copolymers) [75]. The finish parts usually possess inadequate mechanical properties and thus post treatments such as sintering are required to give proper strength and stable geometric integrities. The 3D printers developed by

Extrude Hone (Irwin, PA, USA) employ different metal powders such as stainless steel and aluminum but the ones developed by Soligen (Northridge, CA, USA) use alumina powder.

When the binder is blended with the powder, the binding process is activated upon the deposition of the aqueous or organic ink. The system supplied by Therics Company (Princeton, NJ, USA) and uses chloroform as an organic ink. A printer (ZPrinter® from Z-Corporation, Burlington, MA, USA) has one of the most widely applied of the 3DP technologies. These printers utilize Hewlett-Packard's ink-jet technology to deposit aqueous binder to bond organic or inorganic powders. BMT (Koblenz, Germany) introduced Deskmodeler$^{TM}$ that utilizes poly(vinyl alcohol) (PVA) powders which can be bonded by dispensing an aqueous ink.

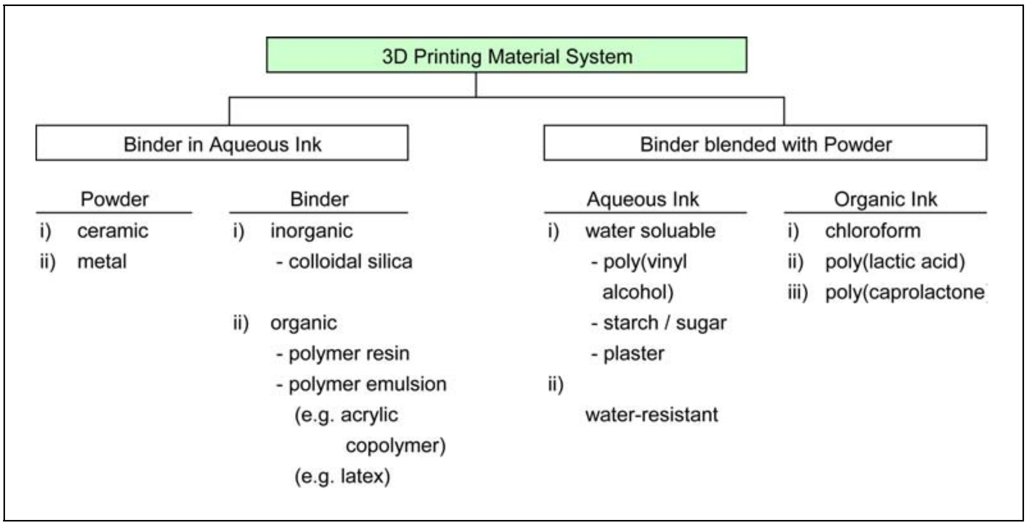

Figure 2-5: Overview of the different material systems used in 3DP processes as adopted from [75].

The three main advantages of 3DP compared to most RP systems are high speed, lower cost of part fabrication, and its suitability for ceramic-based powder such as CPP, and HA. The high process speed can be attributed to the fact that no phase change, including melting and/or solidifying, is involved in the process. The lower cost is a result of the material, equipment, and speed [76]. Moreover, the process does not require supporting structures for overhang geometries since the part is supported by surrounding powder within the work envelope.

On the other hand, quite a number of problems stand in the way of the widespread use of 3DP, namely the available materials, surface finish, and the accuracy. These factors make 3DP a weaker fabrication technique when compared with SLA and SLS [77]. The accuracy of the printer is limited by the nozzle size, the precision of the position controller that defines the movement of the printhead, and the powder particle size that governs the layer thickness. In addition, the materials used for tissue engineering scaffolds usually exist in non-powder forms and require special processing for 3DP [57][78].

Irsen *et al*. [78][79] developed a 3D printing apparatus for direct production of ceramic-based porous scaffolds using spray-dried hydroxyapatite granulates and a polymeric binder consisting of water and Schelofix. They fabricated two types of test parts: rectangle grid parts of $7.8 \times 7.8\ \mathrm{mm}^2$ with wall thickness of 330 μm and cylindrical parts with a diameter of 7.8 mm and rectangle channels ranging between $447 \pm 37\ \mu\mathrm{m} \times 559 \pm 33\ \mu\mathrm{m}$. The achieved channel resolution was close to the optimum channel size. The achieved wall thickness was not sufficient to mimic spongiosa of human bone, but was a good structure resolution for the fabrication of highly macroporous scaffolds for tissue engineering applications [79]. The sintered samples had pores in the range of 10 to 30 μm and the particles had a good connection through sintering.

Sherwood *et al*. [80] designed and tested a cartilage-bone scaffold with two distinct materials having different porosity, pore sizes, and mechanical properties using the TheriForm$^{\mathrm{TM}}$ process. The bone part of the scaffold, composed of NaCl/calcium phosphate tribasic (TCP)/$_{\mathrm{L}}$-PLGA had a porosity of 55% and a pore size of > 125 μm. It was in a cloverleaf shape to allow for adequate contact between the scaffold and the surrounding subchondral bone for sufficient bone ingrowth. In addition, the leaves channels were designed for bone marrow derivatives to contact a larger surface area. The authors suggested that the method could be used to repair articular defects *in vivo* and could be expanded to repair large regions of articular joint and potentially the whole joint surface.

#### 2.3.3.1 Accuracy of Three-Dimensional Printing Accuracy

The achievable dimensional and geometric accuracy of the 3DP system are not clearly defined even in the most successful case studies. Other publications stated only a superficial view on this issue without a detailed analysis of the problem [52]. Although for a wide variety of applications, the question of accuracy is not applicable. In other applications such as fit and function and molding, knowing the degree of accuracy is mandatory.

The research directly related to the accuracy of 3DP is limited with only a few journal papers investigating the achievable accuracy of this technology [52]. However, in terms of layer based manufacturing, the research available spans from build process optimization to inaccuracy of prediction and correction. The most in depth and recent research performed by Dimitrov suggested that the dimensional accuracy depends on the material, the printer axes responsible, and the magnitude of the nominal dimension [52]. In a previous case study, he reported that the dimensional error is in general 1% of the required nominal values [81].

Curodeau *et al.* [71] have conducted a comprehensive study on the process and machine constraints of 3DP. They reported a dimensional variation of the machine structure is approximately 5 to 10 μm in all three axes. Along the scanning x-axis, the accuracy depends on the droplet certainty of the actual printhead controller and the drop merging effects. The inaccuracy can add up to an off-center distance of -65 to -5 μm. Along the scanning y-axis, the accuracy is mainly depended on the jet radial stability and can contribute to a ±8 μm of variation. Along the z-axis, Lee *et al.* [82] suggested that the accuracy is related to powder compaction over the full depth of the powder bed and the offset was estimated to be ±15 μm.

### 2.3.4 Indirect Rapid Prototyping

In addition to fabricating the scaffolds directly from a 3D printing apparatus, the use of a negative mold based on a scaffold design to cast the scaffold using desired polymeric and/or ceramic biomaterials is one emerging method.

Wilson *et al.* [83] created calcium phosphate scaffolds by casting hydroxyapatite slurry in the fugitive wax molds produced by a SLA apparatus. These scaffolds have defined and reproducible three-dimensional porous architectures. They report ectopic bone formation on all scaffolds. In addition, they suggest that the mold texture, which was impressed onto the scaffold during casting, is an important factor for the budding of bone formation away from the scaffold surface [83]. Taboas *et al.* [84] have developed a series of porous polymer-ceramic scaffolds by using indirect 3DP and conventional sponge scaffold fabrication. The scaffolds have locally and globally porous internal architecture with channels ranging from 500 to 800 μm.

## 2.4 Computer Numerically Controlled Machining

Milling operation, conducted on computer numerically controlled (CNC) machine tools, has become one of the most widely used technologies in manufacturing industries to produce components with desired shapes and dimensions. For example, ball-end milling has been used extensively in manufacturing of complex freeform surfaces in molds and dies, turbines, and aircraft components; while, face milling has been used in manufacturing of automotive components. The major feature that distinguishes machining from rapid prototyping is the material subtraction, where material is removed from a workpiece using cutters. This technique allows for productivity and accuracy. In order to better control the part quality and manufacturing efficiency, planning of the machining process parameters becomes very important. These parameters include cutter geometry, cutting setup, workpiece and tool materials, as well as the performance of the CNC unit. In terms of controlling the dimensional accuracy and the surface finish, the static and dynamic deformations of the tool excited by the cutting forces calls for a tremendous amount of attention [85]. As a result, the ability to predict the cutting forces, torque, and the power demand, leads to the ability to optimize the machining process and mechanics.

### 2.4.1 Mechanics of Orthogonal and Oblique Cutting

Orthogonal cutting is a simple case of two-dimensional cutting where material is removed by a cutting edge that is perpendicular to the direction of the cutting velocity as shown in Figure 2-6 [86]. Thus, the cutting forces are only exerted in the directions of the velocity and the uncut chip thickness, which are referred to as tangential ($F_t$) and feed ($F_f$) forces respectively. The material removal is assumed to be uniform with a constant width of cut $b$ and a depth of cut $h$, without side spreading of the material. Whereas, in three-dimensional oblique cutting, the cutting edge is inclined at an acute angle $i$, normal to the plane of cutting edge as shown in Figure 2-7. This produces a third force ($F_r$) that acts in the radial direction. Due to the rather complex geometry in oblique cutting, cutting forces are predicted by kinematics and geometrical transformation from orthogonal data [87]. Many practical oblique cutting operations including turning, drilling, and milling, can be evaluated using this method.

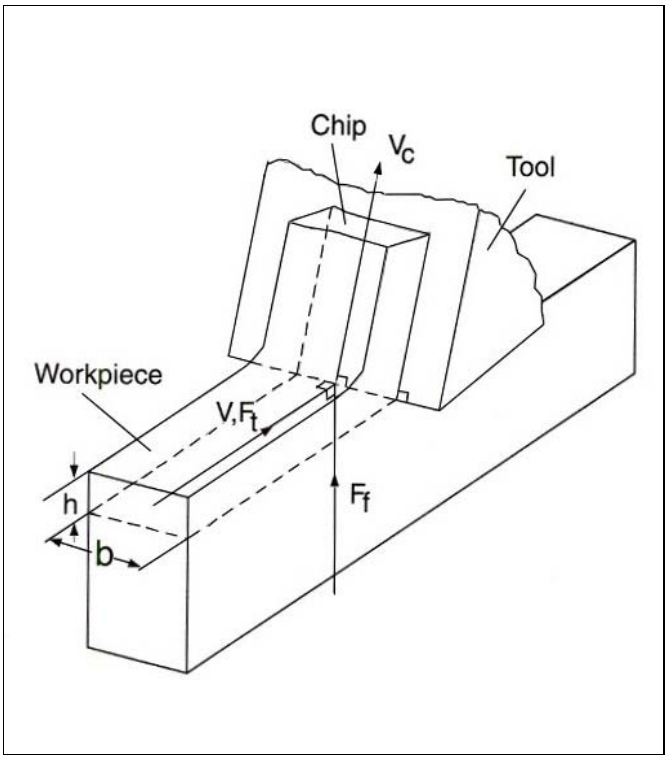

Figure 2-6: Schematic representation of orthogonal cutting process [86].

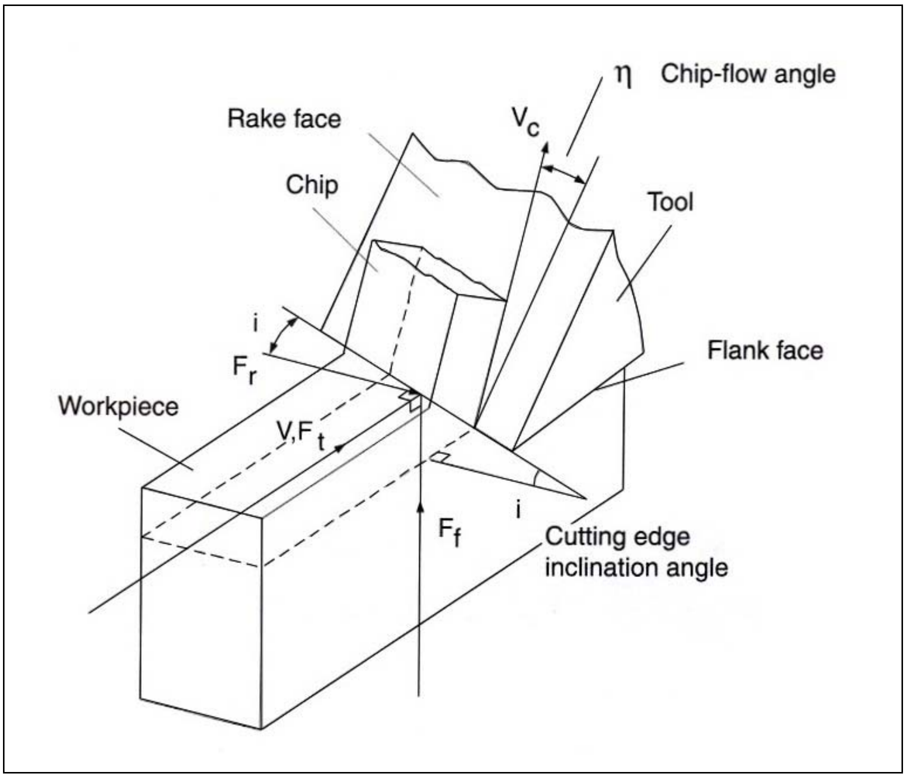

Figure 2-7: Schematic representation of oblique cutting process [86].

### 2.4.2 Kinematics of Milling

There are two type of milling operations used in practice: face and peripheral milling. Peripheral milling is also referred to as end milling which includes both up- and down-milling operations. In up-milling, as the cutting edge enters the workpiece, the chip thickness increases as shown in Figure 2-8. The entry angle is zero and cutting edge moves against the feed direction. On the contrary, in down-milling, chip thickness decreases as the cutter edge moves in and along the same direction as the workpiece.

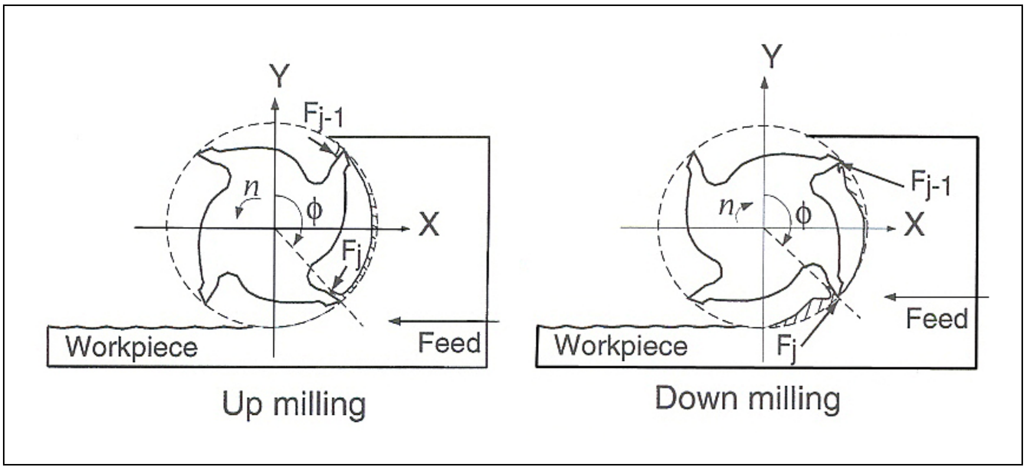

Figure 2-8: Up- and down-milling operations [86].

#### 2.4.2.1 Cutting Forces Modeling for Milling Process

It is important that cutting forces are maintained at the optimal values since they support both product quality as well as machining efficiency. This is achieved through careful modeling of the physical phenomenon that generates the forces. There are, in general, two most widely used force modelling systems: i) mechanistic model and ii) unified mechanics of cutting.

In the mechanistic model, cutting forces are calculated based the average cutting force data and the cutting coefficients. These coefficients are functions of workpiece material, axial depth of cut, chip width, as well as cutter geometry, which includes helix angle, rake angle, and relief angle. Therefore, they need to be derived from experimental milling tests for a specific cutter and tool-workpiece material combination using curve fitting techniques. Following that, instantaneous force components and their fluctuations over a cutter revolution can be computed. The mechanistic cutting force prediction model was first introduced by Kline and DeVor to examine cornering cuts [88] and cutter run-out [89]. Their model establishes a relationship between chip load, cutter geometry, and elemental tangential and radial force components in end milling. This process was further improved by Sutherland and DeVor for flexible flat-end milling systems [90]. The model used in this thesis was developed and formulated by Budak *et al.* [87] into the following equations,

$$\left.\begin{aligned} F_{\mathrm{t}}(\phi) &= K_{\mathrm{tc}} a h(\phi) + K_{\mathrm{te}} a \\ F_{\mathrm{r}}(\phi) &= K_{\mathrm{rc}} a h(\phi) + K_{\mathrm{re}} a \\ F_{\mathrm{a}}(\phi) &= K_{\mathrm{ac}} a h(\phi) + K_{\mathrm{ae}} a \end{aligned}\right\} \tag{2.1}$$

where $F_{\mathrm{t}}(\phi)$, $F_{\mathrm{r}}(\phi)$, $F_{\mathrm{a}}(\phi)$ are tangential, radial, and axial cutting force acting on the cutting edge respectively. $a$ is the edge contact length, $h$ is the instantaneous chip thickness, and $\phi$ is the angular immersion along the cutting edge. The subscripts c and e in Equation (2.1) represent cutting and edge force components, respectively. $K_{\mathrm{tc}}$, $K_{\mathrm{rc}}$, and $K_{\mathrm{ac}}$ are due to shearing at the shear plane and the friction at the rake face in the tangential, radial, and axial directions respectively. $K_{\mathrm{te}}$, $K_{\mathrm{re}}$, and $K_{\mathrm{ae}}$ are due to ploughing at the flank of the cutting edge in the tangential, radial, and axial direction respectively.

Despite the usefulness of the mechanistic model, the time and expense involved in conducting cutting tests empirically for each cutter design may be considered as impractical. An alternative technique is called the unified mechanics of cutting, where all the tool and cut geometric variables are incorporated. In this model, the coefficients are determined by modelling the tooth elements under oblique cutting conditions from an orthogonal cutting database [86]. Hence, these coefficients are functions of shear stress, shear angle, and friction angle [87]. This approach demonstrates its usefulness in general applications using different cutters. Nevertheless, one shortcoming is the time and effort required to prepare an appropriate orthogonal cutting database, which involves conducting cutting tests at various combination of cut thickness, rake angle, and cutting speeds [87].

### 2.4.3 Machinable Ceramics

Even with the wide use of machining in many industries and of many materials, machining of ceramics is rather difficult. Hitherto, there are three main classes of machinable ceramics: machinable glass-ceramics [91][92][93], machinable multiphase ceramics, and machinable $Ti_3SiC_2$ ceramics. The glass ceramics can be further classified into mica-containing or without mica. Glass ceramics containing mica, such as MACOR® (Corning Inc., Corning, NY, USA), have been developed since the 1970s [91] and have been known to show good machinability. The ease of machining of these ceramics is a result of the cleavage of the precipitated crystals within the laminate of the glass [91][92]. In contrast, glass ceramics without mica crystals such as $CaO\text{-}Al_2O_3\text{-}Y_2O_3\text{-}SiO_2$ and $CaO\text{-}P_2O_5\text{-}Al_2O_3\text{-}TiO_2\text{-}SiO_2$ [93] have also been reported to be machinable. However, the exact mechanism for the machinability is not well understood.

Most of the reported works on machining of ceramics have concentrated on development and improvement of machinability from a material characterization point of view. The machining part of the research often lacks detailed documentation. Kasuga *et al.* [92] produced glass ceramic blanks containing a large amount of calcium pyrophosphate ($Ca_2P_2O_7$) powders by sintering. The machinability was assessed by drilling experiments conducted with a conventional carbide tool with a diameter of 1.5 mm at a spindle speed of 1800 rpm under a 19.6 N load. Although their achieved drilling rate of 250-300 μm/min was not higher in comparison with that of the MACOR®, their work represented an important contribution in machining of calcium phosphate materials. Wang and James [93] developed a $40.5CaO\text{-}39.3P_2O_5\text{-}6.8Al_2O_3\text{-}5.6TiO_2\text{-}7.8SiO_2$ (in mol%) glass and showed the machinability by a drilling test using a 2.5 mm tungsten carbide drill bit operating at 3800 rpm at a load of 2.5 kg. The samples could also be turned and threaded with a highly polished surface.

In terms of the mica-based ceramics, MACOR® has demonstrated its machining tolerance up to 0.0127 mm (0.0005") with a surface finish of less than 0.00508 mm (0.00002"). This material can be milled using a carbide tool to achieve the optimal cutting speed of 6.1 to 10.7 m/min, at a feed of 0.05 mm/tooth, and a depth of cut of 3.8 to 5.1 mm [94]. Zhang *et al.* [91] fabricated a fluoramphibole glass-ceramic and evaluated the machinability by drilling tests. Their glass ceramic has a hardness slightly above 5.0 GPa, which is in the scope of hardness that glass-ceramics can be machined. The machining results showed that this material has good machinability, where thin walls of 0.8 mm and intact screws could be milled.

### 2.4.4 Biomedical Engineering Applications

Advanced engineering ceramics are well used in industrial components including valves, spark plugs, and turbine blades. In the medical field, ceramics are applied in significant quantities in artificial joints, dental prosthetics, and artificial heart valves [34][38]. Even with the wide use of machining in many industries and of many materials, machining of ceramics is rather difficult and machining of ceramics for biomedical applications has been relatively limited. This often is a result of high costs, surface damage, and the extremely high hardness and brittle nature of the materials. In recent years, the use of ceramics or ceramic composites in the oral cavity has become more popular due to the increased need of aesthetic appearance and the biological incompatibility of metallic dental bridges. Some examples of the dental ceramics include leucite reinforced porcelain, glass-infiltrated porous alumina, glass ceramics, and tetragonal zirconia polycrystals (TZP) [95]. However, many of them have not yet been used for all-ceramic dental bridges due to difficulties in shaping by convention techniques including casting, sintering, and hot pressing. Filser *et al.* [95] demonstrated a direct ceramic machining (DCM) process whereby machining a soft pre-sintered ceramic blank and followed by sintering to yield full density. No cracks were found in the machined framework and the microstructure of the sintered framework appeared to be homogeneous without flaws and exaggerated grain growth. Al-Shammery *et al.* [96] developed a novel machinable mica-based glass ceramic. To demonstrate the feasibility, they machined dental crowns using theirs and a leading commercial material (Vitabloc by Vita Zahnfabrik) for comparison.

To the best of the author's knowledge, no work has been reported for producing tissue engineering scaffolds directly by machining from a sintered ceramic blank to obtain the exterior implant shape. However, machining has been employed in several studies as a mean to fabricate molds with anatomically-shaped surfaces for preparation of the scaffolds or to shape trabecular bone blocks into proper surface contour and topography [20].

## 2.5 Summary

In this chapter, three major review of literature studies have been presented. Foremost, information on various calcium phosphate ceramics is introduced to provide an overview on their development as bone-substituting substrates. Following that, a survey of academic literature and biomedical practices relevant to rapid prototyping has been presented. Three RP technologies have been discussed: stereolithography, selective laser sintering, and three-dimensional printing. These technologies have demonstrated their feasibility in fabricating substrates using different ceramics and polymers to yield different porosity, pore sizes, and mechanical properties. Lastly, general theories of CNC machining have been introduced, followed by a discussion of machining applications for biomedical engineering. To the best of the author's knowledge, no work has been reported on fabricating calcium polyphosphate substrates with complex freeform surfaces that match the subchondral bone curvatures at the defect site using three-dimensional printing. In addition, there have not been reports on the fabricating process details including machine and process parameters used in fabricating substrates using the other RP techniques. In terms of CNC machining, there is a lack of use of this technique in fabricating complex CPP substrates.

# Chapter 3

# Indirect- and Direct-3DP for Fabrication of CPP Substrates

## 3.1 Overview

Three dimensional printing (3DP) is one of the most emerging rapid prototyping (RP) or solid freeform fabrication (SFF) techniques. Its ability to build complex parts with conformal passages and specified internal architectures offers great potentials for the biomedical field, in particular, tissue-engineering substrates. This chapter first examines the two methods, indirect- and direct-three-dimensional printing, employed to fabricate calcium polyphosphate bone-substituting substrates with any pre-determined shape. For each method, the material preparation and fabrication procedure are described in details. Subsequently, experimental results are presented to quantify dimensional shrinkage and percent of theoretical full density, along with scanning electron microscopy images to show sintered microstructures. Additionally, the 3DP process in terms of the achievable dimensional and geometric accuracy is investigated. It is necessary to understand the resolution of the 3DP process in order to confidently adopt this technique in the fabrication of tissue engineering substrates.

## 3.2 Indirect Three-Dimensional Printing

As the name suggests, the 3DP method is employed indirectly to fabricate CPP substrates when indirect-3DP method is implemented. This involves the production of polymeric molds using the default 3DP system and material. These molds, which are the inverse of the desired shapes, are used to pre-shape CPP samples.

### 3.2.1 CPP Substrate Fabrication Process using Indirect-3DP

The indirect-3DP method involved a six-step procedure as presented in Figure 3-1 and is listed below:

i) CAT scan image representing the area of interest
ii) Development of the substrate CAD model
iii) Development of CAD model of a mold
iv) Fabrication of the mold
v) Pre-shaping of CPP substrate
vi) Binder removal and sintering

#### 3.2.1.1 CAT Scan Image and Development of Substrate CAD Model

Clinical planning, evaluation, and diagnosis are often supported by medical imagining. In customized tissue reconstruction, the imaging modalities that provide adequate information on anatomy is often the interest. These imagining techniques include computer axial tomography (CAT), magnetic resonance imaging (MRI), and ultrasound. CAT scans are also referred to as computer tomography (CT) scans. These images can be obtained by using an x-ray equipment to produce multiple images at different angles of the area of interest followed by computer processing to join these images together into cross-sectional views. They provide information about the bones, internal organs, soft tissues, to blood vessels with great clarity. Examples of some axial cross-sections derived from the CT scans of a sheep's knee can be seen in Figure 3-2.

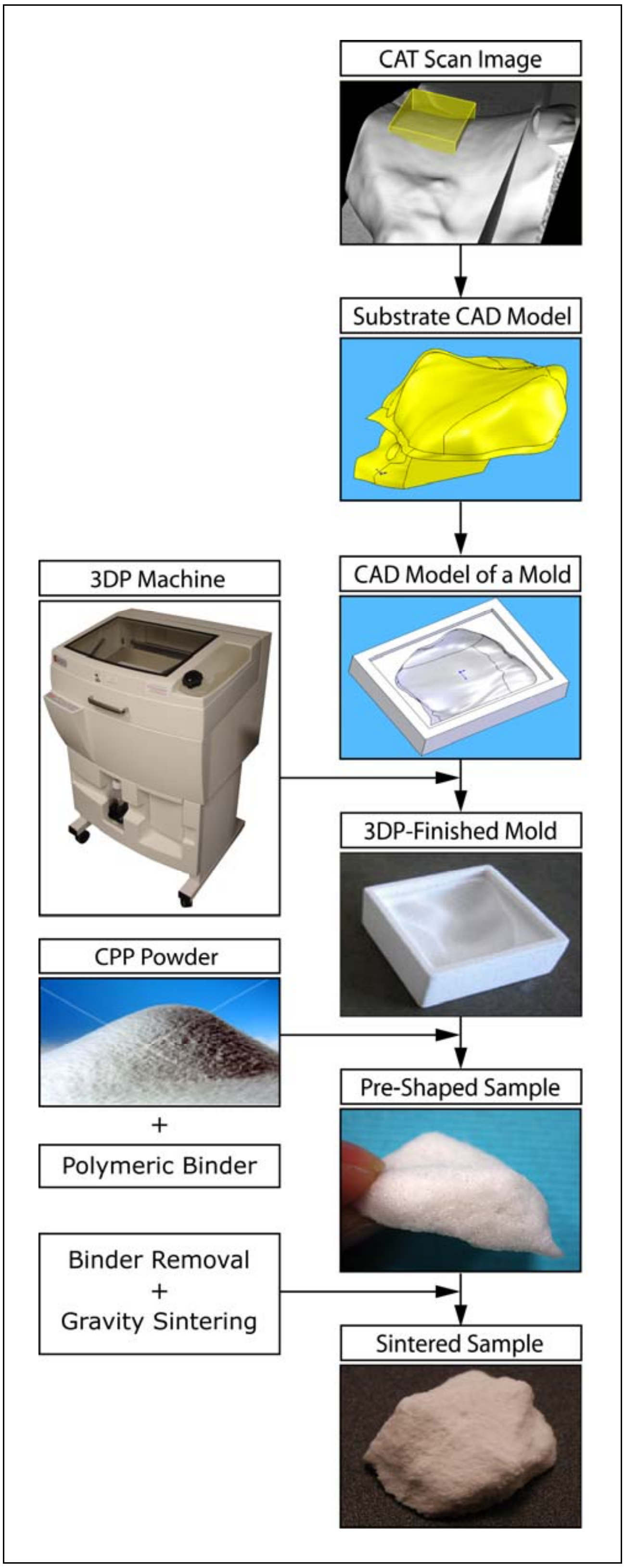

Figure 3-1: Process flowchart of indirect 3DP.

In this work, the substrate was designed by Dudi and Papini [97] by extracting freeform surfaces from computer axial tomography (CAT) scan images of sheep knees as shown in Figure 3-3. The objective of using sheep models was to verify the best CPP implant shape that can sufficiently withstand the applied load and provide a favourable mechanical environment for the cartilage layer seeded on top. Once this method is fully developed, patient-specific CAT images can then be the subject of interest. The implant consists of two main features: i) a freeform surface with the shape of an average tibial medial plateau designed using finite element analysis (FEA) to yield a desirable geometry required for cartilage and bone formation and ii) a keel with a through hole to allow surgeons to fix the implant during surgery using biodegradable screws or pins.

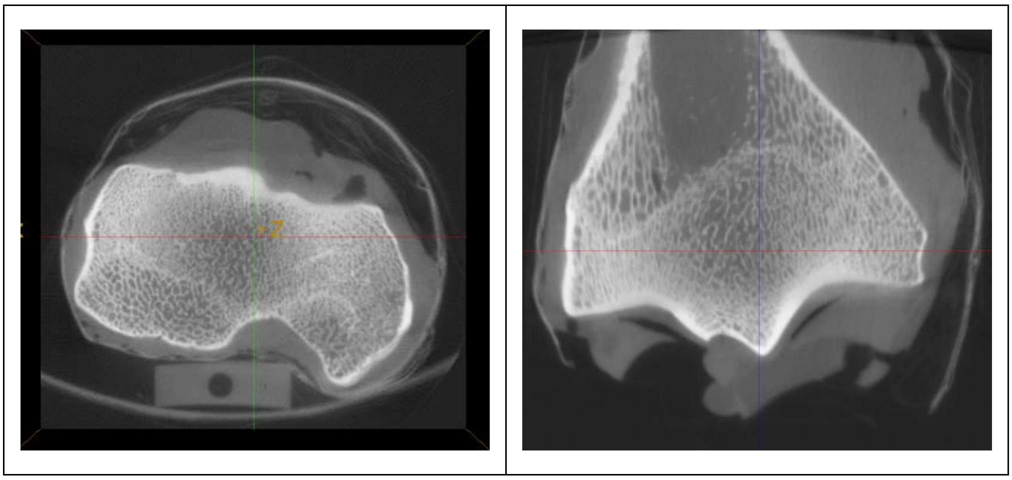

Figure 3-2: CAT scans of a sheep's tibial plateau at different orientations.

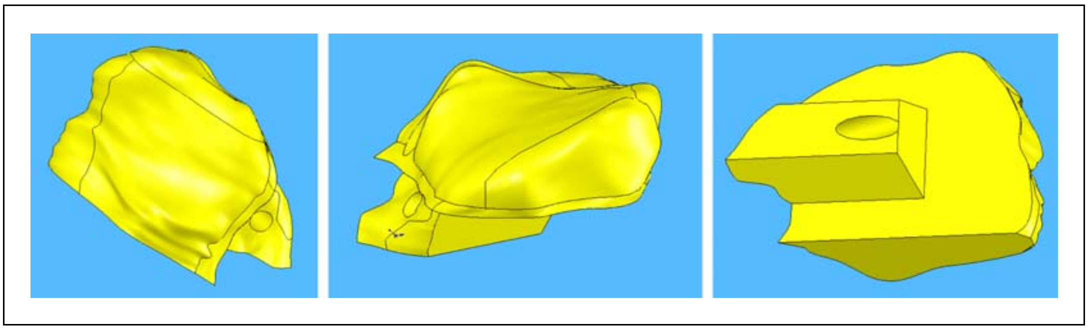

Figure 3-3: Substrate designed by Dudi and Papini [97].

### 3.2.1.2 Development of CAD Model of a Mold

After the implant design is finalized, a mold is generated to give the negative projection of the implant. The model of the mold is designed using computer-aided design (CAD) packages, SolidWorks® (SolidWorks Corp., Concord, MA, USA) and Unigraphics NX® (UGS Corp., Plano, TX, USA). Following that, the mold is sectioned to produce a multi-segment mold as shown in Figure 3-4. The multi-segment mold enables several parting directions during part ejection to overcome the restrictions of having undercuts and overhangs. This also allows for easier part removal without damaging the delicate sample.

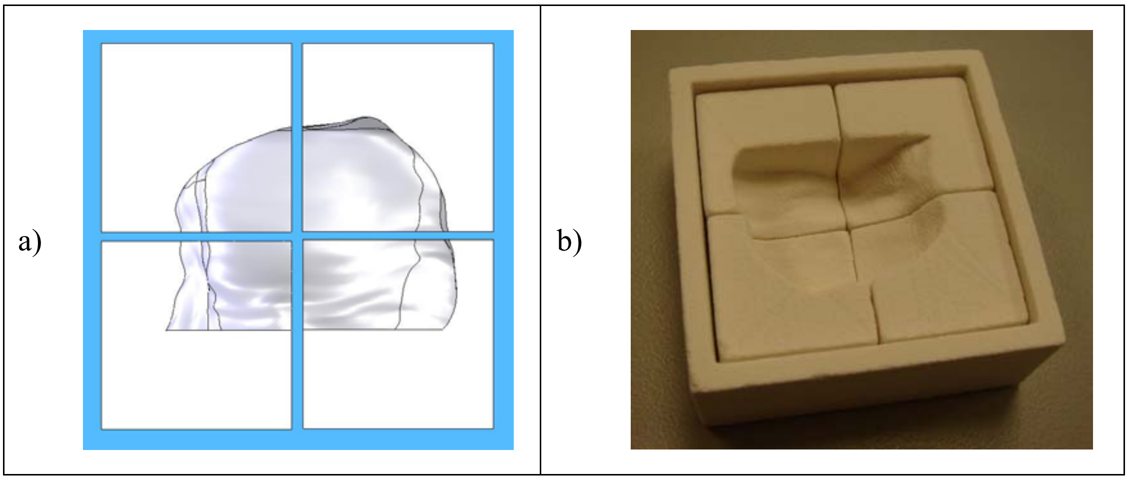

Figure 3-4: Multi-segment mold: a) CAD model and b) 3DP-fabricated.

### 3.2.1.3 Fabrication of the Mold

The CAD model is then converted to the industry-standard RP file, .STL or .VRML to comply with Z-Corporation's ZPrinter® (310 Plus, Z-Corp., Burlington, MA, USA). The default material system for this printer and the machine setup are described in the following sections.

#### 3.2.1.3.1 ZPrinter® Setup

The material used to fabricate these molds is the default printer material, which is a plaster-based powder (zp$^{TM}$130, Z-Corp.). The powder particles are joined by the application of an aqueous-based binder (zb$^{TM}$58, Z-Corp.). The process parameters used are recommended by the system manufacturer and are summarized in Table 3-1. All 3D objects are converted into 2D cross-sections with a layer thickness of 0.102 mm (0.004"). This value yields parts with optimal quality, as well as reducing production time and powder consumption. The binder saturated value represents the degree of infiltration of the binder, which is an important factor in determining the part quality. A higher concentration of binder is applied to all edges of each part, resulting in a stronger exterior as shown in Figure 3-5. The printer builds an infrastructure by printing strong scaffolding within the part's exterior walls. The remaining interiors are printed with a lower saturated value to provide part stability and yet prevent over saturation, which can cause part distortion.

Table 3-1: Recommended parameters for ZPrinter® 310 Plus and zp$^{TM}$130 [98].

| Recommended parameters | Values |
|---|---|
| Layer thickness | 0.102 mm (0.004") |
| Saturation level | 100% |
| Saturated value - shell | 1.1 (110%)* |
| Saturated value - core | 0.4 (40%)* |

* The exact binder amount is not disclosed by Z-Corporation.

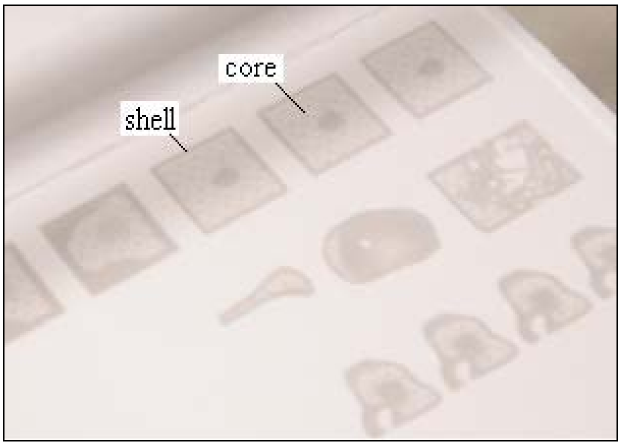

Figure 3-5: Definition of shell and core.

For ZPrinter® 310 Plus, the ink-jet printer head (HP 10 Black, Hewlett-Packard Development Co., Palo Alto, CA, USA) moves in the y-axis along a gantry. A picture illustrating the system components can be seen in Figure 3-6. This gantry is mounted onto another structure that moves horizontally across the work envelope in the x-direction. The movement in x- and y-direction are driven by two belts.

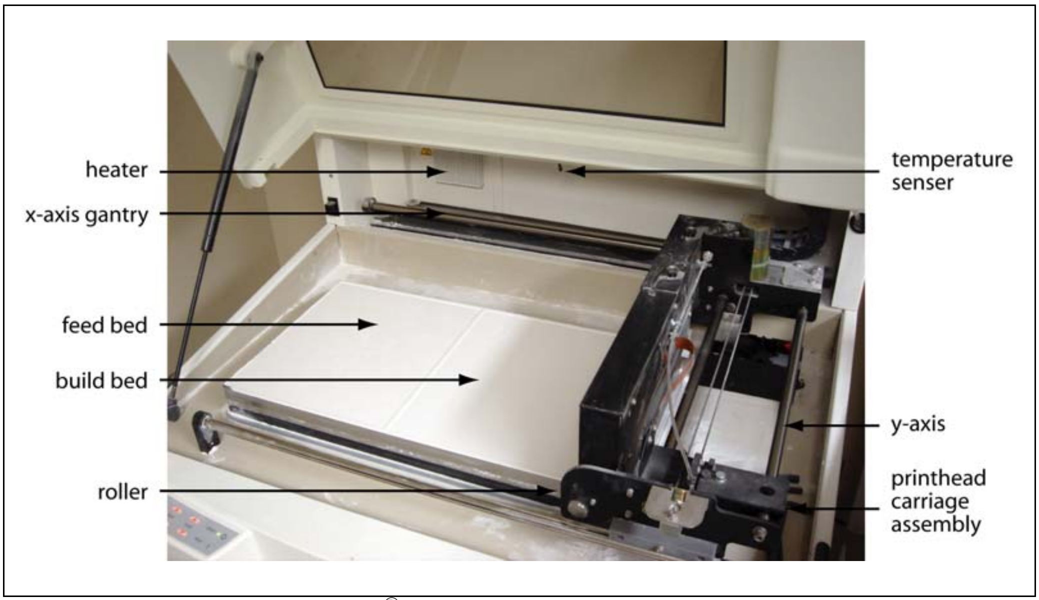

Figure 3-6: ZPrinter® 310 Plus system component illustration.

Upon fabrication, mold can be infiltrated with cyanoacrylate (Z-Bond™ 101, Z-Corp.) to increase durability and reduce loss of powder during handling.

### 3.2.1.4 Pre-shaping of CPP substrates

Subsequently, substrate sample is pre-shaped by filling the CPP paste into the mold. The procedure used to prepare the paste is presented in the next section. The paste in the mold is placed inside an electric furnace for 4h at 50°C to assist in drying and left overnight at room temperature for self-hardening. To assist in sample removal, a small amount of distilled water was used to partially dissolve the mold.

#### 3.2.1.4.1 CPP Paste Preparation

CPP glass powder used in this study is produced according to a method described previously by University of Toronto [13] (see Section 2.1.1 ). Two ranges of particle size are used: <75 μm and 106-150 μm. The polymeric liquid binder is a mixture of 7.4%w polyvinyl butyral (PVB) (Butvar® B-98, Solutia Inc., St. Louis, MO, USA) and 92.6%w pure grade ethanol.

To prepare the polymer binder, 0.1 g of PVB is mixed with 1.584 ml of ethanol using a hot plate-magnetic stirrer (PG 351, Corning Inc., Corning, NY, USA) for 3 min. Low heat is applied for 1 min to assist dissolution of PVB in ethanol. This binder is then used to prepare the paste for pre-shaping. The CPP powder is mixed with the polymeric binder in a 1.85 g to 1 ml ratio using the hot plate-magnetic stirrer for 40 min to achieve the proper consistency. During this mixing process, low heat is activated for 1 min at the 5-, 10-, 15-, 20-, and 30-min mark during a 40 min period to assist blending. Heat is turned off at the 31-minute mark to allow the paste to cool to room temperature.

### 3.2.1.5 Binder Removal and Sintering

The final step is to heat treat the pre-shaped sample. The heat treatment process includes binder removal and gravity sintering. The polymeric binder keeps the net shape of the pre-shaped sample during fabrication. However, the binder needs to be removed by heating to its decomposition temperature [35]. This was conducted in a platinum crucible using an air furnace (Thermolyne® 48000, Barnstead International, Dubuque, Iowa USA).

The final porous CPP substrate is then produced by sintering the sample in an air muffle furnace (Thermolyne® 6000, Barnstead International). The conditions for binder removal and gravity sintering processes are summarized in Table 3-2 and Table 3-3.

Table 3-2: Binder removal process for <75 μm and 106-150 μm CPP powder.

| | <75 μm | 106-150 μm |
|---|---|---|
| Temperature1 | 22°C | 22°C |
| Heat-up Rate | 10°C/min | 10°C/min |
| Temperature2 | 500°C | 500°C |
| Dwell Time | 3 h | 2 h |

Table 3-3: Gravity sintering process for <75 μm and 106-150 μm CPP powder.

| | <75 μm | 106-150 μm |
|---|---|---|
| Temperature1 | 500°C | 500°C |
| Heat-up Rate | 5°C/min | 5°C/min |
| Temperature2 | 582°C | 590°C |
| Dwell Time | 1 h | 1 h |
| Heat-up Rate | 10°C/min | 10°C/min |
| Temperature3 | 950°C | 950°C |
| Dwell Time | 1 h | 1 h |
| Heat-up Rate | Air-cooled | Air-cooled |
| Temperature4 | 22°C | 22°C |

### 3.2.2 Characterization of Sintered Sample Produced by Indirect-3DP

The following sections cover the techniques associated with characterization of the sintered CPP samples with regard to their dimensional shrinkage, density, and volume density. In addition, the sintered samples were examined with scanning electron microscopy to assess pore shapes and inter-particles sinter neck junction.

#### 3.2.2.1 Dimensional Shrinkage

To study the dimensional shrinkage for the samples made indirectly, comparable pre-shape dimensions between all samples are desired. The mold for the sample had a rectangle cavity with a dimension of 3.5 × 10.5 × 3.5 mm. According to Figure 3-7, the width is defined in the x-axis, the length is in along the y-axis, and the height is along the z-axis. Average width, length, and height were measured for each sample before and after sintering. To determine the average value, three measurements were taken at random intervals along each dimension of the sample. The dimensions were measured using a digimatic caliper (Series 500, Mitutoyo Corp., Kawasaki, Japan) accurate to ±0.01 mm.

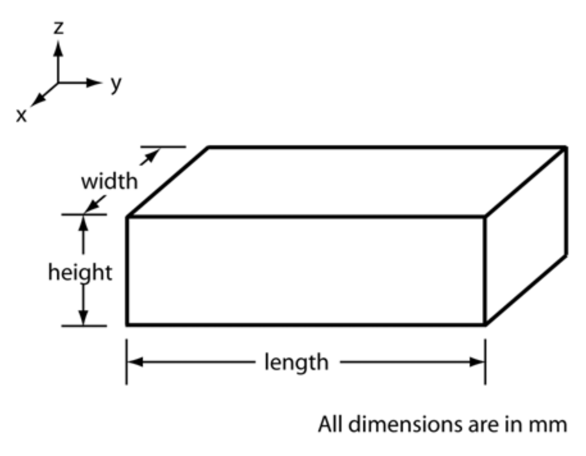

Figure 3-7: Rectangle control sample dimension.

#### 3.2.2.2 Density

The density of each sintered sample was determined by two methods. In the first method, density was measured using a density determination kit (Sartorius YDK01, The Sartorius Group, Goettingen, Germany) to a weight accuracy within ±0.0001 g. This measuring device utilizes the Archimedes' principle to determine the specific gravity of a solid [99]. The principle states that a solid immersed in a liquid is subjected to the force of buoyancy. The value of this force is the same as that of the weight of the liquid displaced by the volume of the solid. This weight is equivalent to the volume displaced multiplied by the density of the fluid. Using this equipment, the bulk density of the sample could be determined according to the following steps as summarized in Table 3-4.

Table 3-4: Procedure for determining the bulk density of sintered sample.

| | |
|---|---|
| Step 1 | Measure the dry weight, $W_d$, of the sample |
| Step 2 | Measure the submersed weight, $W_s$, of the sample in ethanol |
| Step 3 | Measure the wet weight, $W_w$, in air which contains ethanol inside the pores |
| Step 4 | Determine the density of the fluid, $\rho_{fl}$, based on liquid temperature |

Based on the measurement, three parameters need to be computed to determine the bulk density, $\rho_{bulk}$, of the sintered sample.

$$\rho_{solid} = \frac{W_d \left(\rho_{fl} - \rho_a\right)}{0.99983\left(W_d - W_s\right)} + \rho_a \text{ [99]} \tag{3.1}$$

$$V_{pores} = \frac{W_w - W_d}{\rho_{fl}} \tag{3.2}$$

$$\rho_{bulk} = \frac{W_d}{V_{pores} + V_{solid}} \tag{3.3}$$

where $\rho_{solid}$ is the density of the solid, $\rho_a$ is the density of air under standard conditions (20°C and 101.325 kPa). The liquid used for measurement was pure grade ethanol. The volume of the pores, $V_{pores}$, can be determined by the amount of ethanol inside the solid. In the second method, density was determined by the following equation,

$$\rho = \frac{M}{V} \tag{3.4}$$

where M is mass and V is volume. The mass of each sintered sample is measured using an analytical balance (Sartorius YDK01, The Sartorius Group) accurate to ±0.0001 g. The volume is obtained from Section 3.2.2.1.

### 3.2.2.3 Percent Volume Density and Porosity

To determine the percent of theoretical full density and porosity for each sample, the bulk density of the sintered sample is compared with the theoretical density of non-porous CPP (2.85 g/cm$^3$) [13], according to the following equation,

$$\text{Percent of Theoretical Density} = \frac{\rho_{bulk}}{2.85} \text{ ? } 100\% \tag{3.5}$$

$$\text{Percent of Porosity} = 1 - \frac{\rho_{bulk}}{2.85} \text{ ? } 100\% \tag{3.6}$$

### 3.2.2.4 Preparation for Scanning Electron Microscopy

Prior to taking scanning electron microscopy (SEM) images of a sample, an ultrasonic cleaner (Branson 5210, Branson, Danbury, CT, USA) was used to clean the sample for 45 min in pure grade ethanol. The solution was changed every 15 min to ensure purity and avoid cross contamination. Sintered sample was then assessed using scanning electron microscopy (JSM-6460, Jeol Ltd., Akishima, Tokyo) to determine the pore size, shape, and the inter-particle sinter neck junction dimensions. A gold coating of 10 $\eta$m was deposited onto the sample to prevent charging. To examine the cross sections of the sample, a diamond wafering blade (IsoMet® Low Speed Saw, Buehler®, Lake Bluff, IL, USA) was used to cut the sample in half.

### 3.2.3 Characterization Results

The following sections present the dimensional shrinkage, average density and average percent volume density, as well as scanning electron microscopy images of the sintered samples produced via the indirect-3DP method.

#### 3.2.3.1 Dimensional Shrinkage

Shrinkage from sintering was determined as the percentage of change in dimension from the pre-shaped samples. The results are summarized in Table 3-5 (see Appendix A for data and calculations). As can be seen, in general, the degree of shrinkage is most significant in the z-direction causing a 7.08 ± 3.86% and a 5.95 ± 4.42% difference for the <75 and 106-150 μm samples respectively. The degree of variation, as indicated by the standard deviation, was also more significant in the z-direction. By comparing the two powders used, one can observe that the finer samples (<75 μm) shrunk more in all three directions.

Table 3-5: Sintering shrinkage for the indirectly fabricated CPP samples.

| Starting powder size | | Average Pre-Shaped Sample Dimension [mm] | Average Sintered Sample Dimension [mm] | Average Shrinkage [%] |
|---|---|---|---|---|
| <75 µm (n = 44) | x | 3.60 ± 0.16 | 3.34 ± 0.16 | 6.97 ± 5.22% |
| | y | 10.47 ± 0.22 | 9.91 ± 0.30 | 5.27 ± 2.61% |
| | z | 3.46 ± 0.13 | 3.21 ± 0.13 | 7.08 ± 3.86% |
| 106-150 µm (n = 39) | x | 3.35 ± 0.13 | 3.19 ± 0.13 | 4.74 ± 2.69% |
| | y | 9.94 ± 0.16 | 9. 57 ± 0.15 | 3.74 ± 1.11% |
| | z | 3.43 ± 0.10 | 3.22 ± 0.16 | 5.95 ± 4.42% |

#### 3.2.3.2 Density and Porosity

Table 3-6 summarizes the average density and the average volume density for the two types of samples made via the indirect-3DP method (see Appendix A for data and calculations). The densities were determined using two methods, the Archimedes' principle and the dimensional analysis. It can be seen that the results from the two methods yielded considerable discrepancies, with the results acquired using the dimensional analysis being approximately 25% smaller than the results acquired using the Archimedes principle. It was observed that as a result of sintering, samples shrunk erratically across its length, width, and depth. In addition, some of the sintered samples had slightly concave sides, resulting in overestimated volumes and underestimated densities. Therefore, it was assumed that densities determined using the Archimedes' principle are more accurate.

Table 3-6: Average density and percent of theoretical full density of the sintered samples made using the indirect-3DP method.

| Starting Powder | Archimedes' Principle |  | Dimensional Analysis |  |
|---|---|---|---|---|
|  | Average Density [g/cm$^3$] | Percent of Theoretical Full Density [%] | Average Density [g/cm$^3$] | Average Volume Density [%] |
| <75 µm (n = 45) | 1.8888 ± 0.3312 | 66.28 ± 11.62% | 1.4080 ± 0.0796 | 49.40 ± 2.79% |
| 106-150 µm (n = 42) | 1.8773 ± 0.1743 | 65.87 ± 6.12% | 1.3461 ± 0.1180 | 47.23 ± 4.14% |

### 3.2.3.3 Scanning Electron Microscopy

The SEM images were taken at 20×, 50×, 800× and 1500× magnification to show the overall sample, particle distribution, and neck and bond formations. Figure 3-8 and Figure 3-11 present typical samples produced using the indirect method with <75 and 106-150 µm starting powder, respectively. Figure 3-9 and Figure 3-12 demonstrate typical cross-section of samples cut with a diamond blade for the <75 and 106-150 µm starting powder respectively. One can observe that the grains appear to be smeared and under high magnification, there are some very small debris ranging between 1 to 2 µm (Figure 3-12c and d). Figure 3-13 shows a unique pattern found under high magnification. It was noticed that when this pattern occurred, the powder appeared to have very fine grains distributed within the large grains. Figure 3-10 and Figure 3-14 exemplify cases of defects or exceptional microstructures in the <75 and 106-150 µm starting powder, respectively.

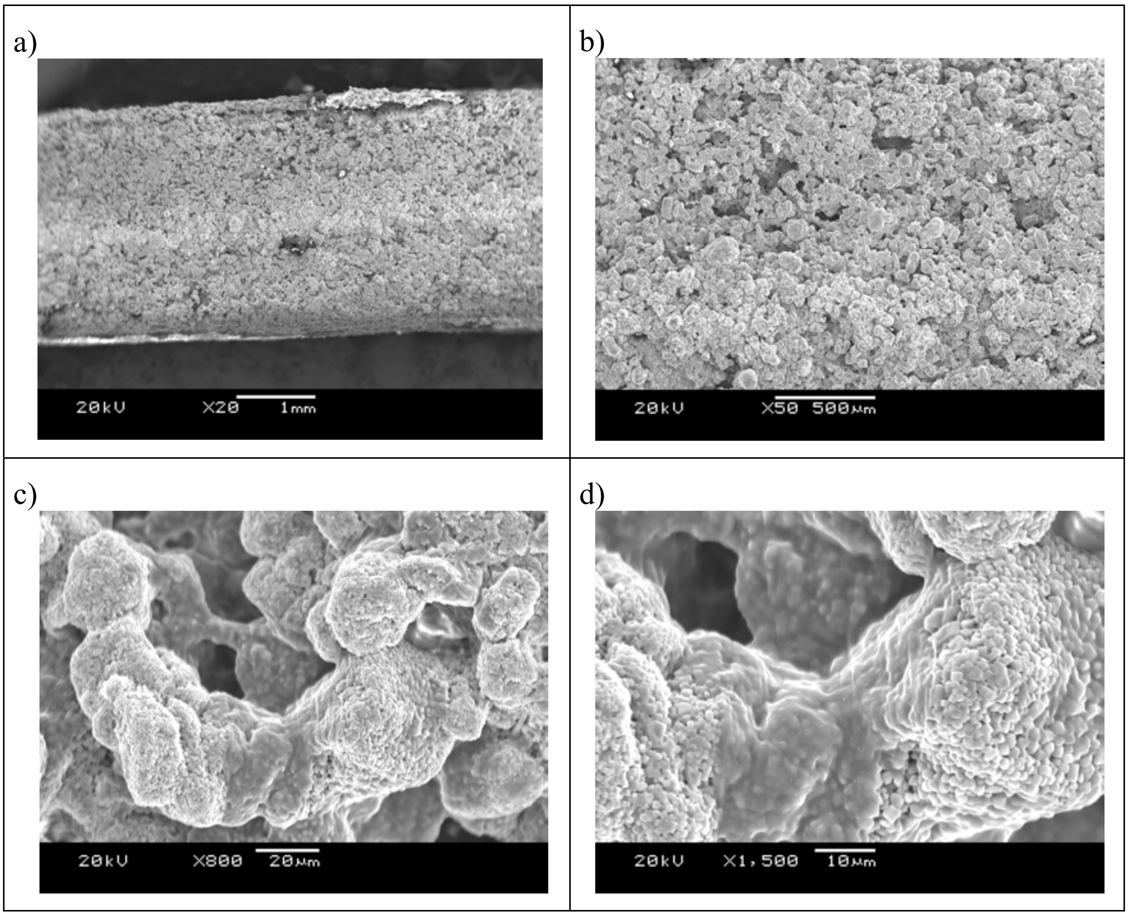

Figure 3-8: SEM images showing typical surfaces achieved in the samples produced using the indirect-3DP method with a starting powder of <75 μm: a) 20×, b) 50×, c) 800×, and d) 1500× magnification.

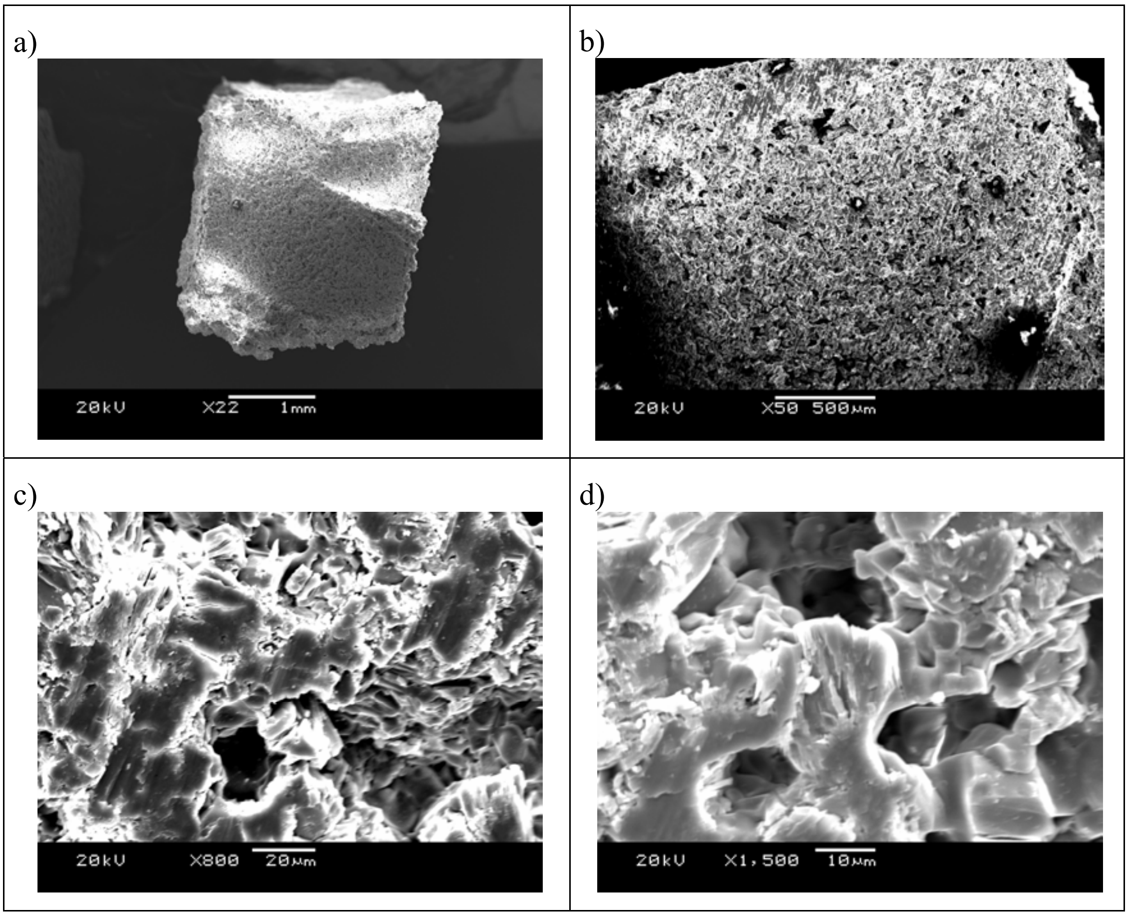

Figure 3-9: SEM images showing typical cross-sections achieved in the samples produced using the indirect-3DP method with a starting powder of <75 μm: a) 20×, b) 50×, c) 800×, and d) 1500× magnification.

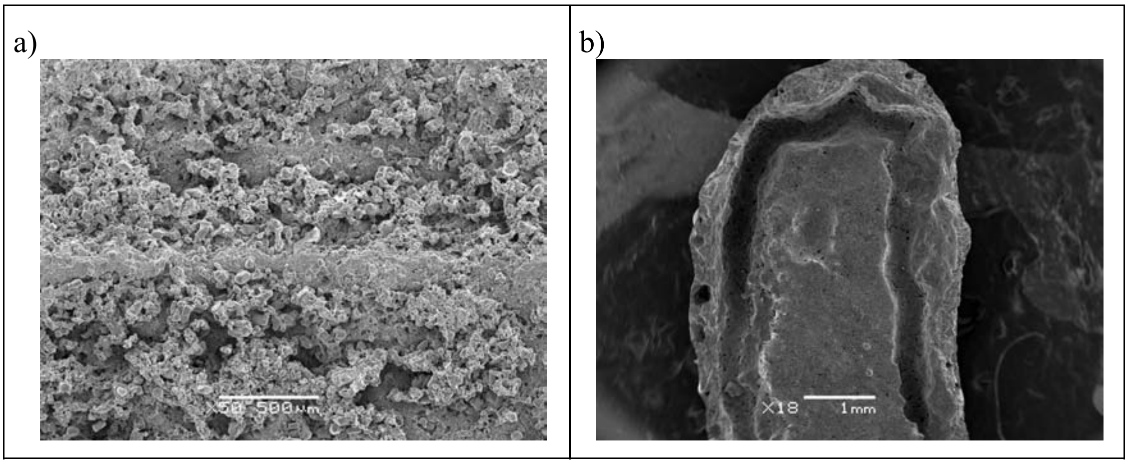

Figure 3-10: SEM images showing various defects found in the in the samples produced using the indirect-3DP method with a starting powder of <75 μm: a) 50× magnification showing fine particle distributions and b) 18× magnification showing a void.

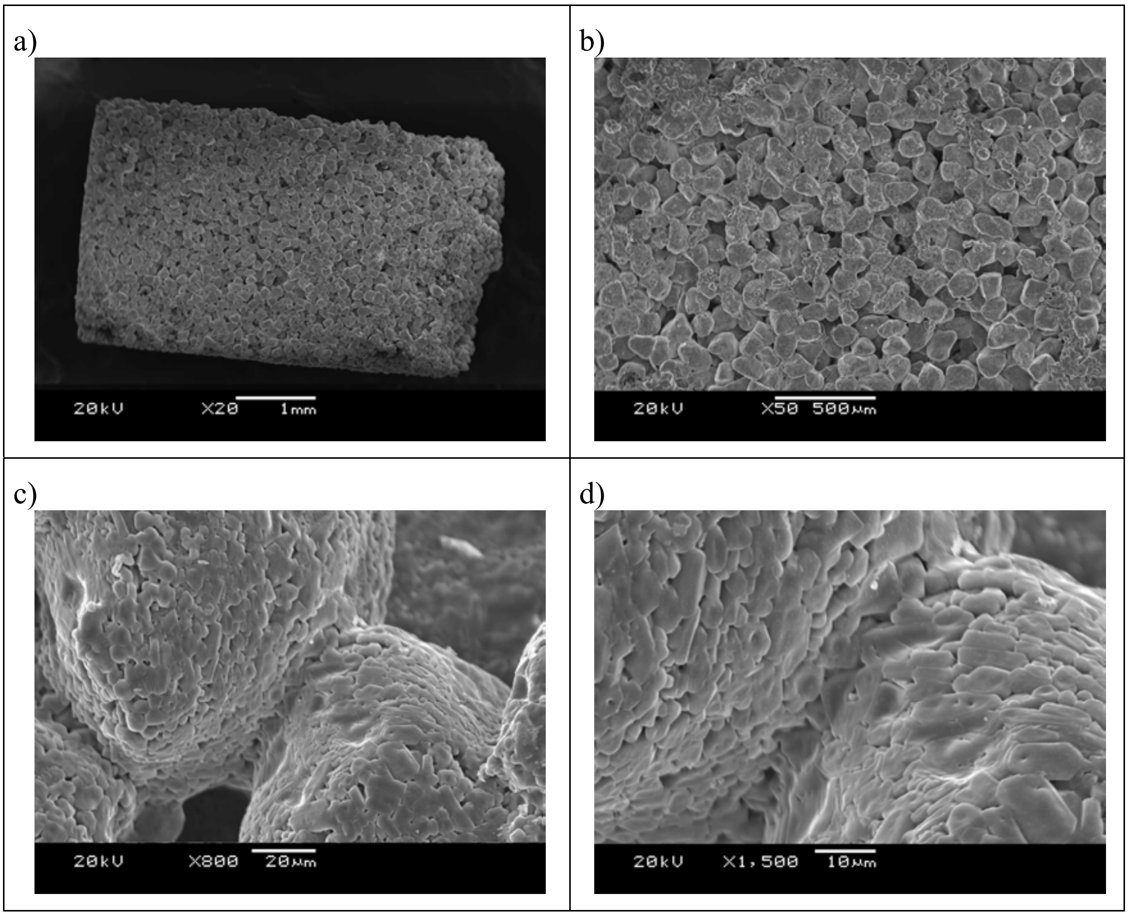

Figure 3-11: SEM images showing typical surfaces achieved in the samples produced using the indirect-3DP method with a starting powder of 106-150 µm: a) 20×, b) 50×, c) 800×, and d) 1500× magnification.

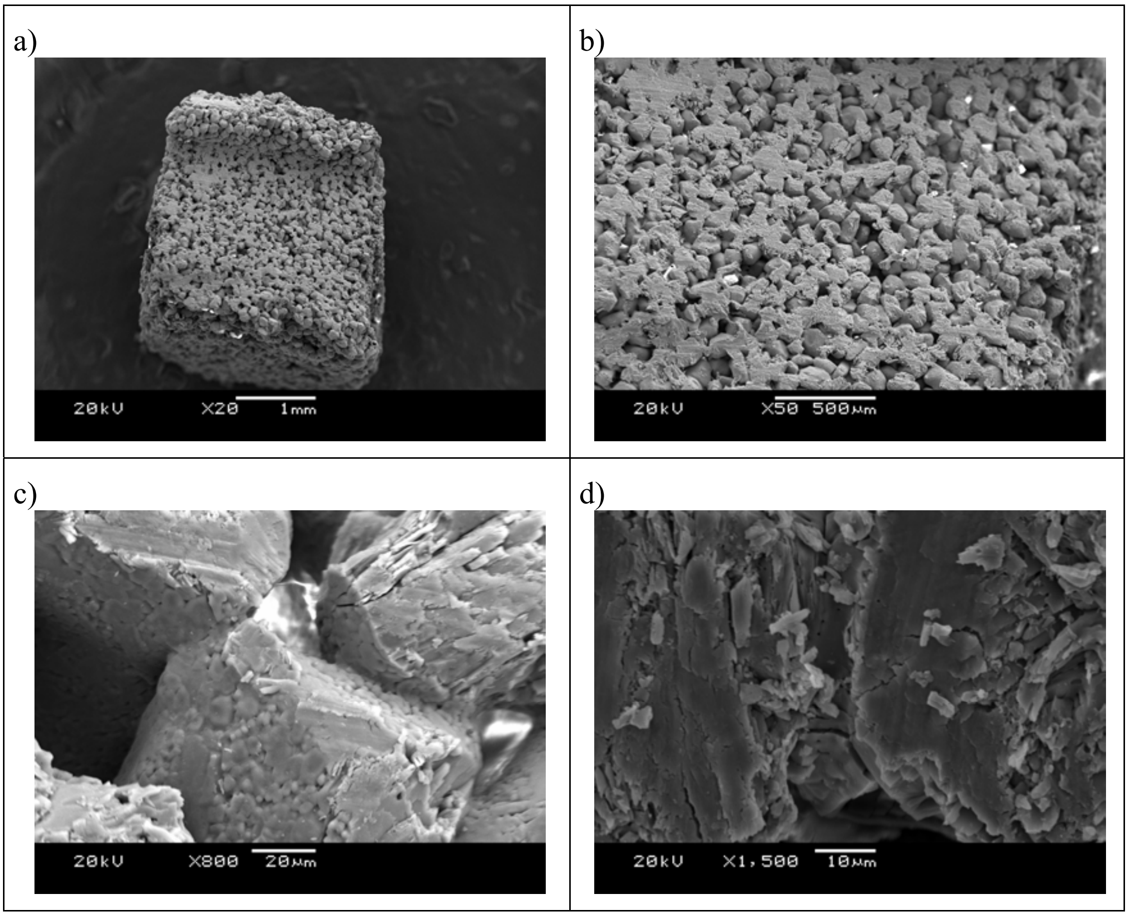

Figure 3-12: SEM images showing typical cross-sections achieved in the samples produced using the indirect-3DP method with a starting powder of 106-150 µm: a) 20× , b) 50×, c) 800×, and d) 1500× magnification.

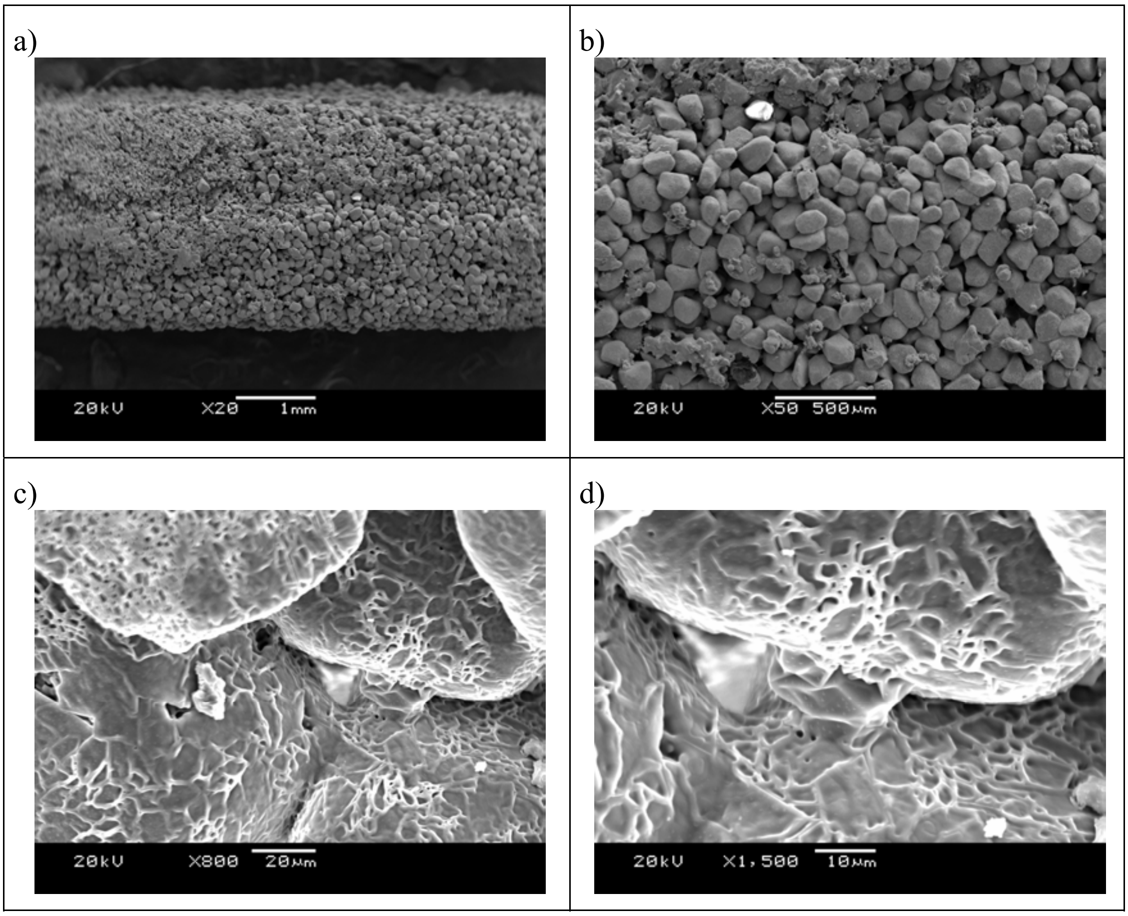

Figure 3-13: SEM images showing a unique pattern found in the samples produced using the indirect-3DP method with a starting powder of 106-150 µm: a) 20×, b) 50×, c) 800×, and d) 1500× magnification.

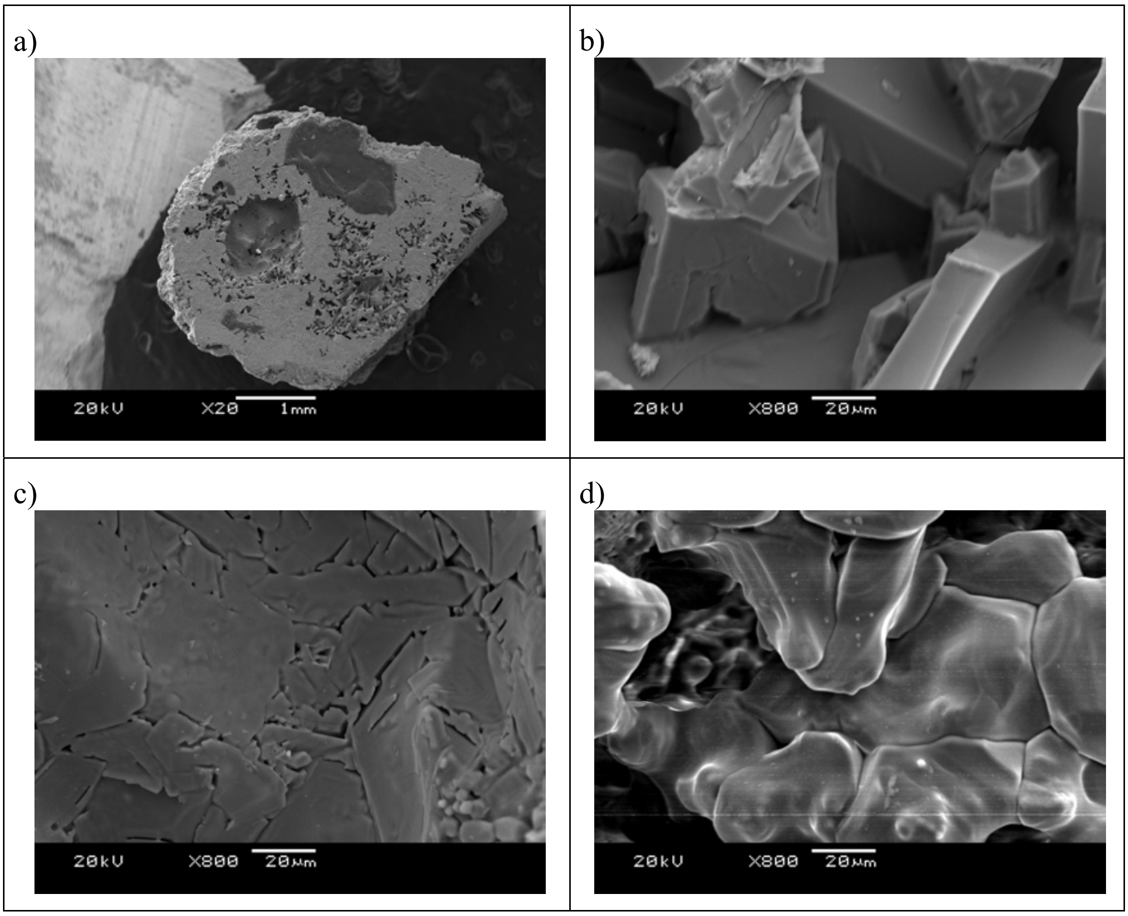

Figure 3-14: SEM images showing defects and some distinctive microstructures found in the samples produced using the indirect-3DP method with a starting powder of 106-150 µm: a) 50× magnification showing the overview of the cross section, b) 800× magnification showing a parallelogram-like microstructure, c) 800× magnification showing a void, and d) 800× magnification showing a melted-looking microstructure.

From the lower magnification (50×) SEM images of the surface (Figure 3-8b and Figure 3-11b) and the cross-sections (Figure 3-9b and Figure 3-12b) of the sintered samples, three-dimensional interconnected porosities are clearly evident for both the <75 and 106-150 CPP µm sintered samples. From this point on, this thesis will refer to the samples made with the <75 µm powder as the fine CPP samples and the samples made using the 106-150 µm powder as the coarse CPP samples. The coarse CPP samples display consistency in particle size distribution. The surface has an average particle size in the 85-175 µm range with the majority of particles in the 85-140 µm range. The structure appears to be uniform across the entire sample and without any noticeable density gradient. In addition, the particles are rounded and angular in shapes which are fairly consistent across the entire sample. Unlike the coarse samples, the <75 μm CPP samples exhibit a wide range of particle sizes and shapes, which vary between rounded spherical, angular, to oblong. It is seen that the fine samples has much rougher surface than that of the coarse sample. The wrinkles on the surface of the coarse sample in Figure 3-13c and d are suspected to be broken crystalline phase [100].

At higher magnifications (800× and 1500×), extensive particle-to-particle junctions and grain boundaries are observed, which demonstrate sufficient sintering for both of the coarse (Figure 3-11c and d) and the fine (Figure 3-8c and d) CPP samples. It is noted that the coarse samples exhibit morphological properties that are in good agreement with that of the samples produced using the standard protocol [13]. In addition, both samples show fine micro-sized crystals in the range of approximately 1 to 10 μm on the particle surfaces. This is indicative of the polycrystalline nature of the individual sintered particles [13].

### 3.2.4 Production of Tibial-Shaped Substrates using Inidrect-3DP

In order to validate the capacity of the indirect-3DP method, complex substrates were pre-shaped using the molds shown in Figure 3-4. The same methodology and material described previously in Section 3.2.1 were employed. The molds had the negative projection of only the tibial feature of the substrate in Figure 3-3. Figure 3-15 shows a complex CPP sample produced using the indirect-3DP method. These samples prove the feasibility of using indirect-3DP to produce complex, anatomically-shaped CPP substrates. In general, the dimensional and the geometric accuracy are adequate. However, the pre-shaped samples have some features that are not replicated exactly and that some samples experience inconsistent shrinkage; thus giving only a near-net shape.

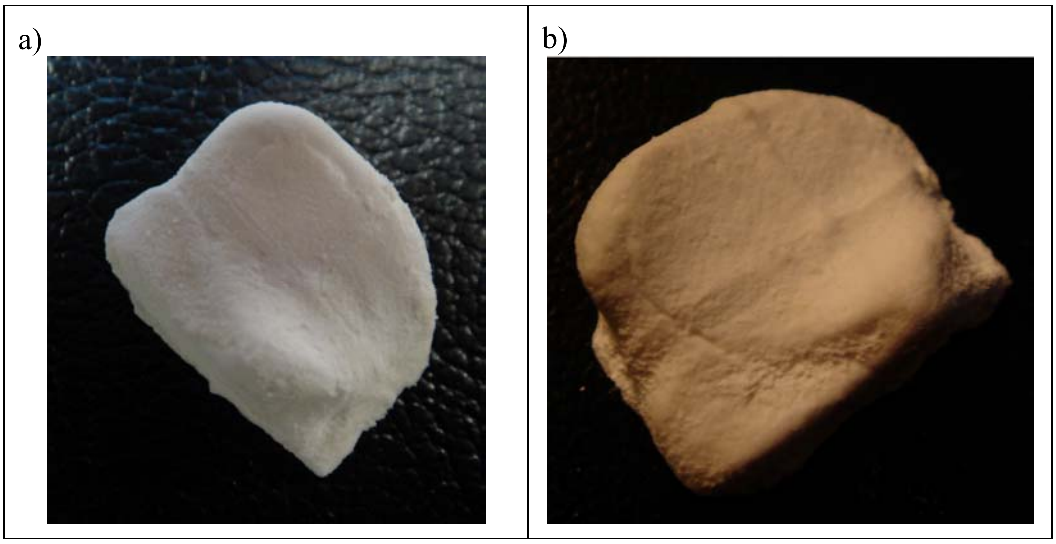

Figure 3-15: Complex CPP sample produced using the indirect-3DP method: a) pre-shaped and b) sintered.

## 3.3 Direct Three-Dimensional Printing

Using some of the findings from the indirect method and the knowledge gained by working with CPP and the PVB binder, several bioceramic and binder system were investigated in order to characterize the machine parameters required to incorporate CPP powder with a mesh size of 106-150 μm into the ZPrinter® and build CPP samples directly.

### 3.3.1 CPP Substrate Fabrication Process using Direct-3DP

The process overview for the direct-3DP method is shown in Figure 3-16. The direct method involves a four-step process.

i) CAT scan image representing the area of interest
ii) Development of the substrate CAD model
iii) Fabrication of the substrate (Section 3.3.1.1)
iv) Binder removal and sintering (Section 3.3.1.2)

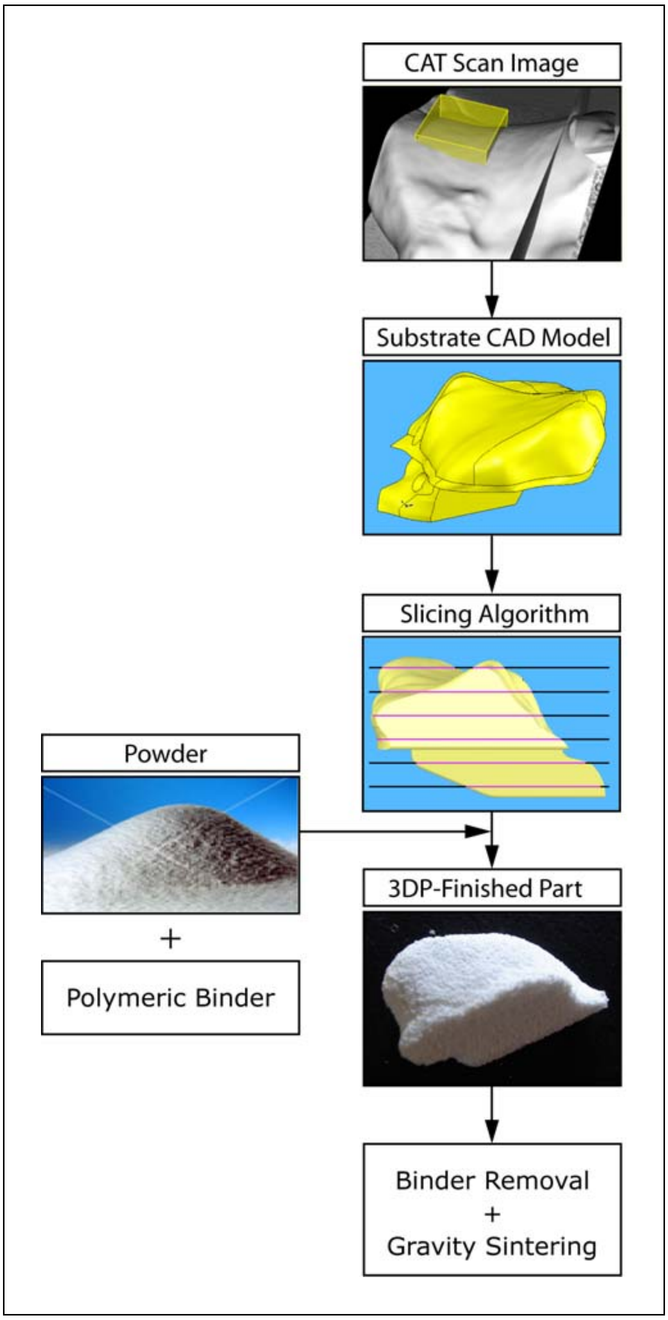

Figure 3-16: Process flowchart of direct-3DP.

The preliminary stages of the process are identical as the indirect three-dimensional printing where CAT scan images were used to design a substrate via CAD software (see section 3.2.1.1).

#### 3.3.1.1 Fabrication of CPP Substrates

A slicing algorithm is applied to generate the 2D information representing that substrate. Subsequently, the substrate is fabricated directly from the retrofitted ZPrinter by Shanjani (University of Waterloo, Waterloo, ON, Canada) as shown in Figure 3-17. The machine is modified to allow for a more efficient and easier material handling and changeover process.

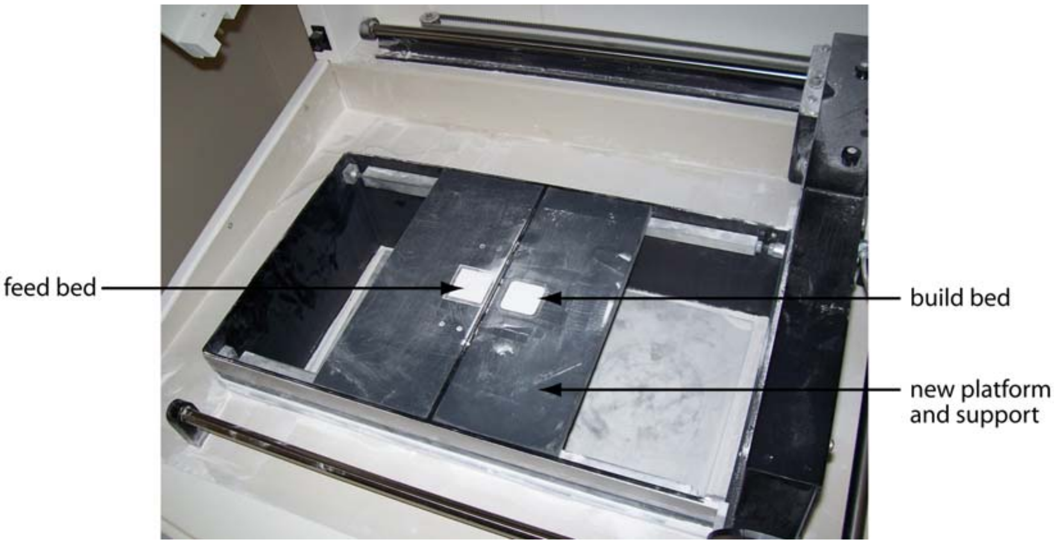

Figure 3-17: Modified ZPrinter for better and easier biomaterial handling.

#### 3.3.1.2 Binder Removal and Sintering

The directly fabricated parts using material system #1 in Table 3-9 undergoes two different heat treatment processes. Each heat treatment process is comprised of two sequential stages: binder removal and gravity sintering. The details are summarized in Table 3-7 and Table 3-8.

Table 3-7: Binder removal process for 45-75 μm CPP powder.

| | Process 1 | Process 2 |
|---|---|---|
| Temperature1 | 22°C | 22°C |
| Heat-up Rate | 10°C/min | 10°C/min |
| Temperature2 | 500°C | 300°C |
| Dwell Time | 3 h | 3 h |

Table 3-8: Gravity sintering process for 45-75 μm CPP powder.

| | Process 1 | Process 2 |
|---|---|---|
| Temperature1 | -- | 300°C |
| Heat-up Rate | -- | 10°C/min |
| Temperature2 | 500°C | 500°C |
| Heat-up Rate | 5 °C/min | 5°C/min |
| Temperature3 | 592°C | 585°C |
| Dwell Time | 1 h | 1 h |
| Heat-up Rate | 10°C/min | 10°C/min |
| Temperature4 | 950°C | 950°C |
| Dwell Time | 1 h | 1 h |
| Heat-up Rate | Air-cooled | Air-cooled |
| Temperature5 | 22°C | 22°C |

### 3.3.2 Material Preparation

Three different material systems were investigated in this study (Table 3-9). CPP glass powder with particle size of 45-75 μm was prepared by the University of Toronto. The polyvinyl alcohol (PVA) powder, 86-89% hydrolyzed, medium molecular weight (Alfa Aesar, Ward Hill, MA, USA) was grounded and sieved (U.S. standard sieve series, Sieve No. 140) to have particle size less than 106 μm. Polyvinyl butyral (PVB) powder (Butvar® B-98, Solutia Inc., St. Louis, MO, USA) was mixed with pure grade ethanol at different proportions as detailed in the table. The mixture was stirred using a hot plate-magnetic stirrer for 15 min to ensure proper consistency.

Table 3-9: Various material systems investigated for the direct-3DP method.

| System # | Powder | | Aqueous Binder |
|---|---|---|---|
| | Ceramic | Polymer | |
| 1 | CPP<br>(45-75 μm)<br>(90%w) | PVA<br>(<106 μm)<br>(10%w) | zb™58<br>default plaster-based binder |
| 2 | CPP<br>(45-75 μm)<br>(90%w) | -- | PVB (7.5%w) + ethanol (92.5%w) |
| 3 | CPP<br>(45-75 μm)<br>(90%w) | -- | PVB (15%w) + ethanol (85%w) |

### 3.3.3 Characterization Results

The following sections present the dimensional shrinkage, average density and average percent volume density, and scanning electron microscopy images of the sintered samples produced via the direct-3DP method from material #1 in Table 3-9. The methodology used to obtain these results is described in Section 3.2.2.

#### 3.3.3.1 Dimensional Shrinkage

Shrinkage results for the samples produced directly are summarized in Table 3-10 (see Appendix A for data and calculations). Similar to the results obtained for the indirect method, the degree of shrinkage is most significant in the z-direction with 22.70 ± 8.87% and 14.00 ± 1.61% for the 592°C and 585°C samples, respectively. The degree of variation, as indicated by the standard deviation, was also more extensive in the z-direction. In addition, the results suggest that samples sintered at a higher temperature exhibit more shrinkage in all three directions.

Table 3-10: Sintering shrinkage for the directly fabricated CPP samples using 45-75 μm CPP starting powder under two different processing temperatures.

| Sintering temperature | | Average Pre-Shaped Sample Dimension [mm] | Average Sintered Sample Dimension [mm] | Average Shrinkage [%] |
|---|---|---|---|---|
| 592°C (n = 8) | x | 3.30 ± 0.07 | 2.66 ± 0.12 | 19.51 ± 3.22% |
| | y | 9.96 ± 0.07 | 8.47 ± 0.18 | 14.86 ± 1.60% |
| | z | 3.06 ± 0.04 | 2.37 ± 0.27 | 22.70 ± 8.87% |
| 585°C (n = 11) | x | 3.14 ± 0.24 | 2.75 ± 0.27 | 12.42 ± 2.96% |
| | y | 10.31 ± 1.00 | 9.04 ± 0.87 | 12.31 ± 0.84% |
| | z | 3.41 ± 0.15 | 2.94 ± 0.14 | 14.00 ± 1.61% |

### 3.3.3.2 Density and Porosity

Table 3-11 summarizes the average density and the average volume density for the two types of samples made via the direct-3DP method (see Appendix A for data and calculations). The effect of sintering temperature can also be clearly distinguished, where samples sintered using a higher temperature yield higher density. Similar to the densities computed in Section 3.2.3.2, it can be seen that densities acquired using the dimensional analysis are approximately 25% smaller than the results acquired using the Archimedes' principle. With the same justifications, it was assumed that densities determined using the Archimedes principle provide more accurate results. Given this, the samples sintered at higher temperature appeared to be approximately 3% to 11% denser than the samples sintered at lower temperature.

Table 3-11: Average density and percent of theoretical full density of the sintered samples made using direct-3DP method.

| Starting Powder | Archimedes' Principle | | Dimensional Analysis | |
|---|---|---|---|---|
| | Average Density [g/cm$^3$] | Percent of Theoretical Full Density [%] | Average Density [g/cm$^3$] | Average Volume Density [%] |
| 592°C (n = 8) | 1.6909 ± 0.2355 | 59.33 ± 8.26% | 1.3515 ± 0.1632 | 47.42 ± 5.73% |
| 585°C (n = 11) | 1.4883 ± 0.1071 | 52.22 ± 3.76% | 1.0755 ± 0.0561 | 37.74 ± 1.97% |

#### 3.3.3.3 Scanning Electron Microscopy

The SEM images were taken at 20×, 50×, 800× and 1500× magnification to show the overall structure, particle distribution, and neck and bond formations. Figure 3-18 and Figure 3-21 present typical samples produced using the direct method and sintered at 592°C and 585°C, respectively. Figure 3-19 and Figure 3-22 demonstrate typical cross section of samples cut with a diamond blade for the 592°C and 585°C samples, respectively. Figure 3-20 shows a sample produced via the standard protocol with the same starting powder used in the direct method for comparison purposes. For comparison, a sample was prepared using the standard protocol (see Section 2.1.1) with a starting powder of 45-75 μm and sintered with the same condition as described in Table 3-7 and Table 3-8. SEM images of the sample are presented in Figure 3-20.

It can be seen from the lower magnification (50×) SEM images (Figure 3-18b and Figure 3-21b) that the structure is porous with three-dimensional interconnected porosity throughout the entire sample. It can also be seen that the pores are reasonably homogenous and that a good connection through sintering was achieved. Under high magnification, some of the grains seem to be fused together, giving the structure a micro-rough surface (Figure 3-19d and Figure 3-21d).

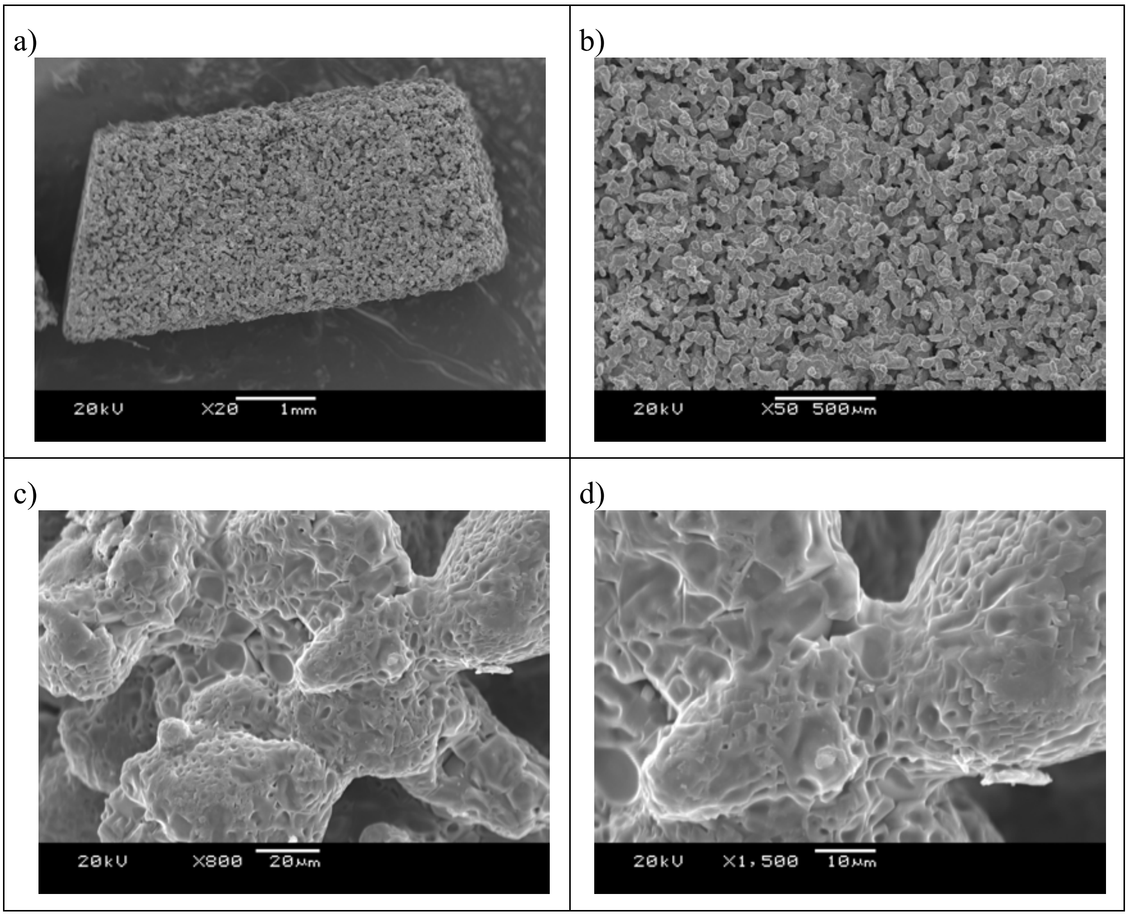

Figure 3-18: SEM images showing typical surfaces achieved in the samples produced using the direct-3DP method and sintered at 592°C: a) 20×, b) 50×, c) 800×, and d) 1500× magnification.

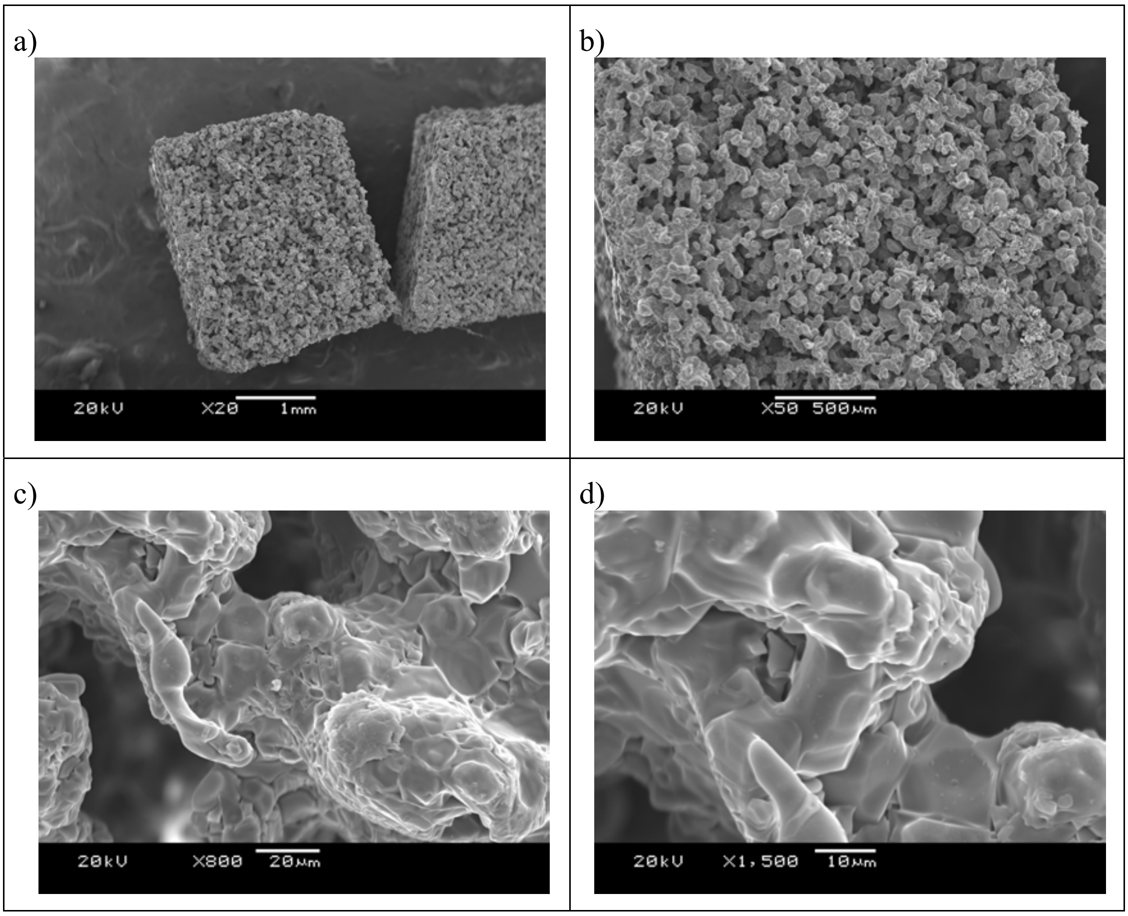

Figure 3-19: SEM images showing typical cross-sections achieved in the samples produced using the direct-3DP method and sintered at 592°C: a) 20×, b) 50×, c) 800×, and d) 1500× magnification.

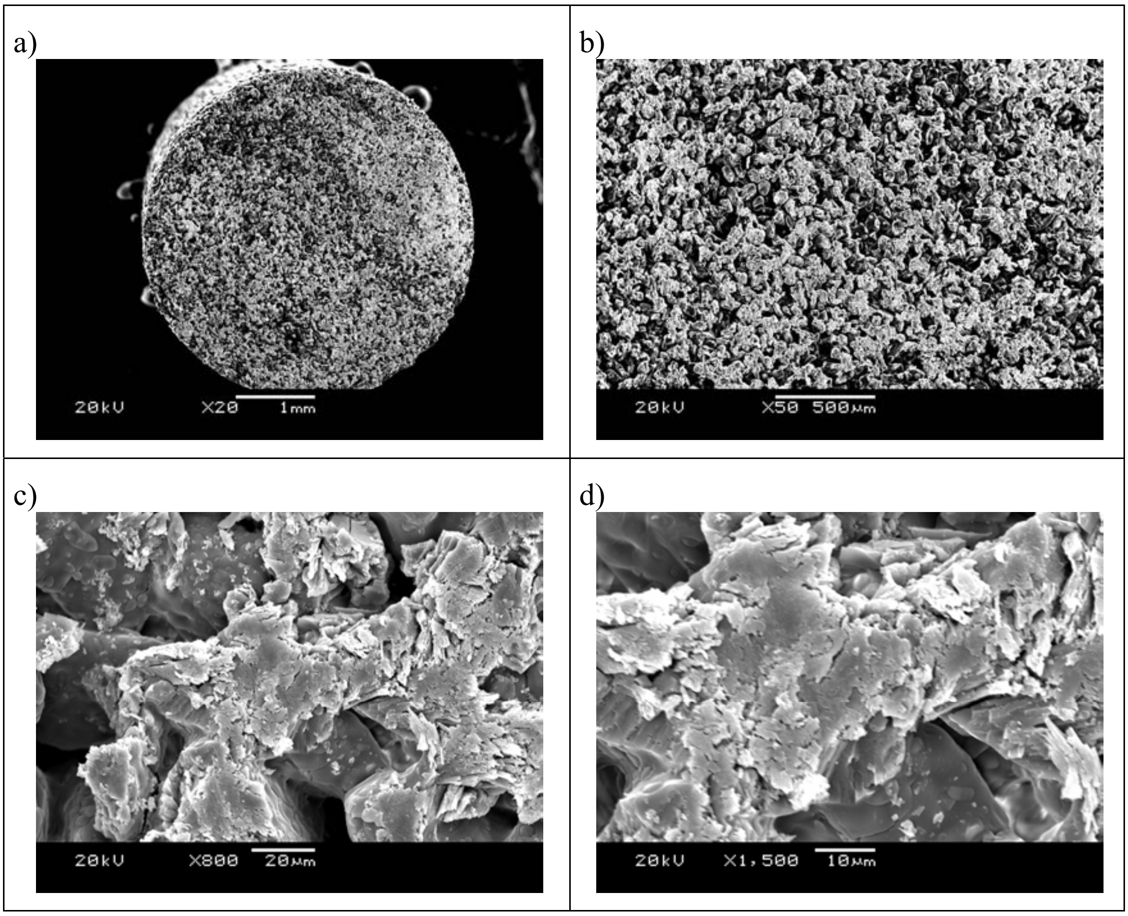

Figure 3-20: SEM images of a sample prepared using the 45-75 µm starting powder via the standard protocol: a) 20×, b) 50×, c) 800×, and d) 1500× magnification.

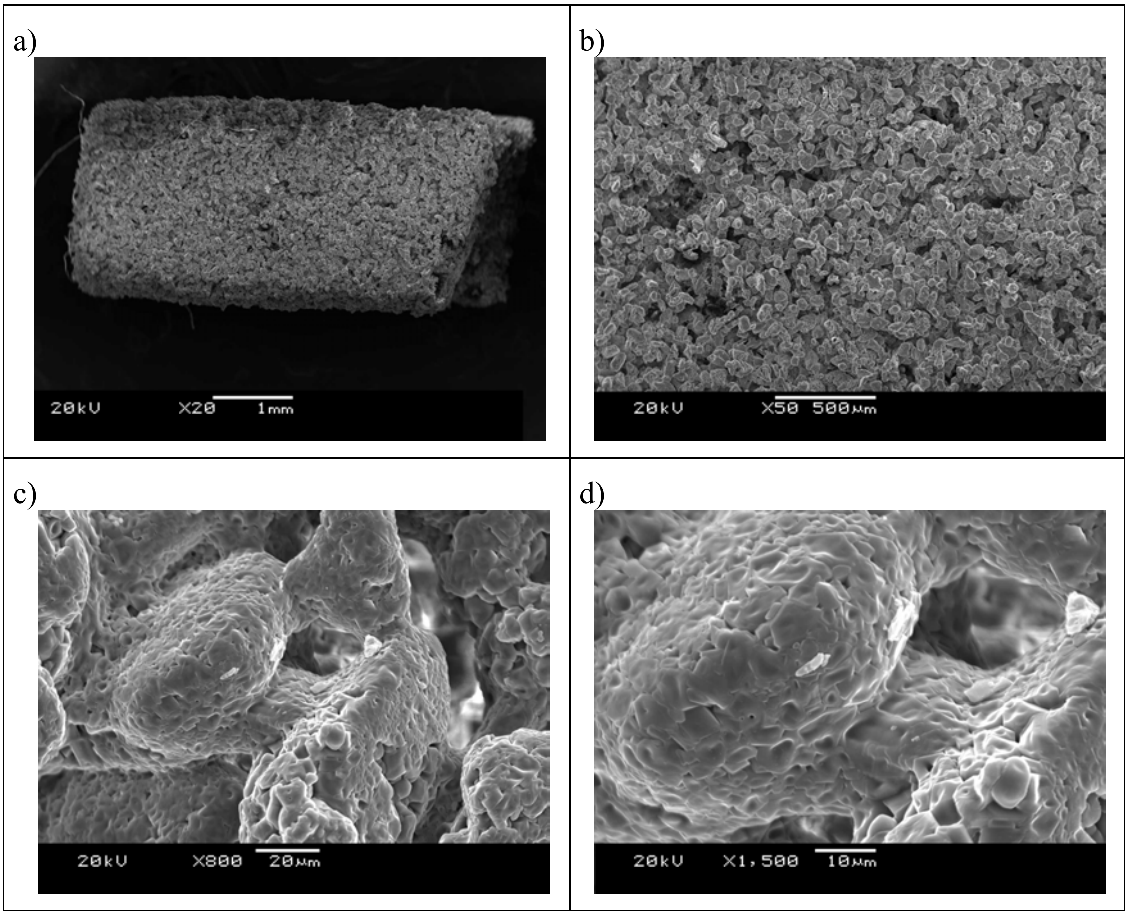

Figure 3-21: SEM images showing typical surfaces achieved in the samples produced using the direct-3DP method and sintered at 585°C: a) 20×, b) 50×, c) 800×, and d) 1500× magnification.

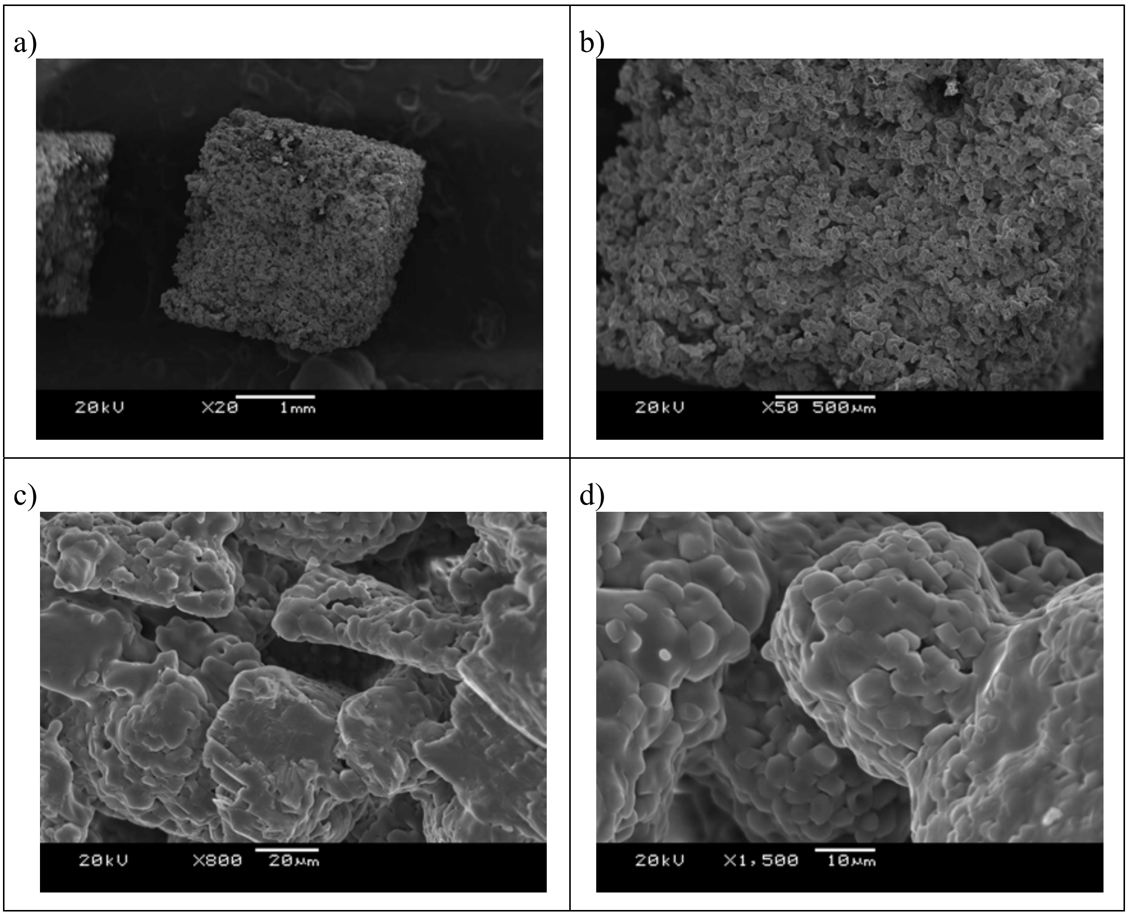

Figure 3-22: SEM images showing typical cross-sections achieved in the samples produced using the direct-3DP method and sintered at 585°C: a) 20×, b) 50×, c) 800×, and d) 1500× magnification.

### 3.3.4 Production of Tibial-Shaped Substrates using Direct-3DP

Similar to the indirect-3DP method, to validate the diversity and the complexity of the CPP samples that can be fabricated using the direct-3DP method, the tibial-shaped substrate described in Section 3.2.4 are produced. The material used for this part of the study is material #1 in Table 3-9. As shown in Figure 3-23a and b, complex parts were produced directly from the 3D printer with reliable geometric precision and accuracy. In addition, the SEM images show three-dimensional interconnected pores and neck formation (Figure 3-23c and d). To demonstrate the aptitude of the 3D printer, conformal channels between 100 to 500 µm are designed and built by Shanjani (University of Waterloo, Waterloo, ON, Canada) as shown in (Figure 3-23e and f).

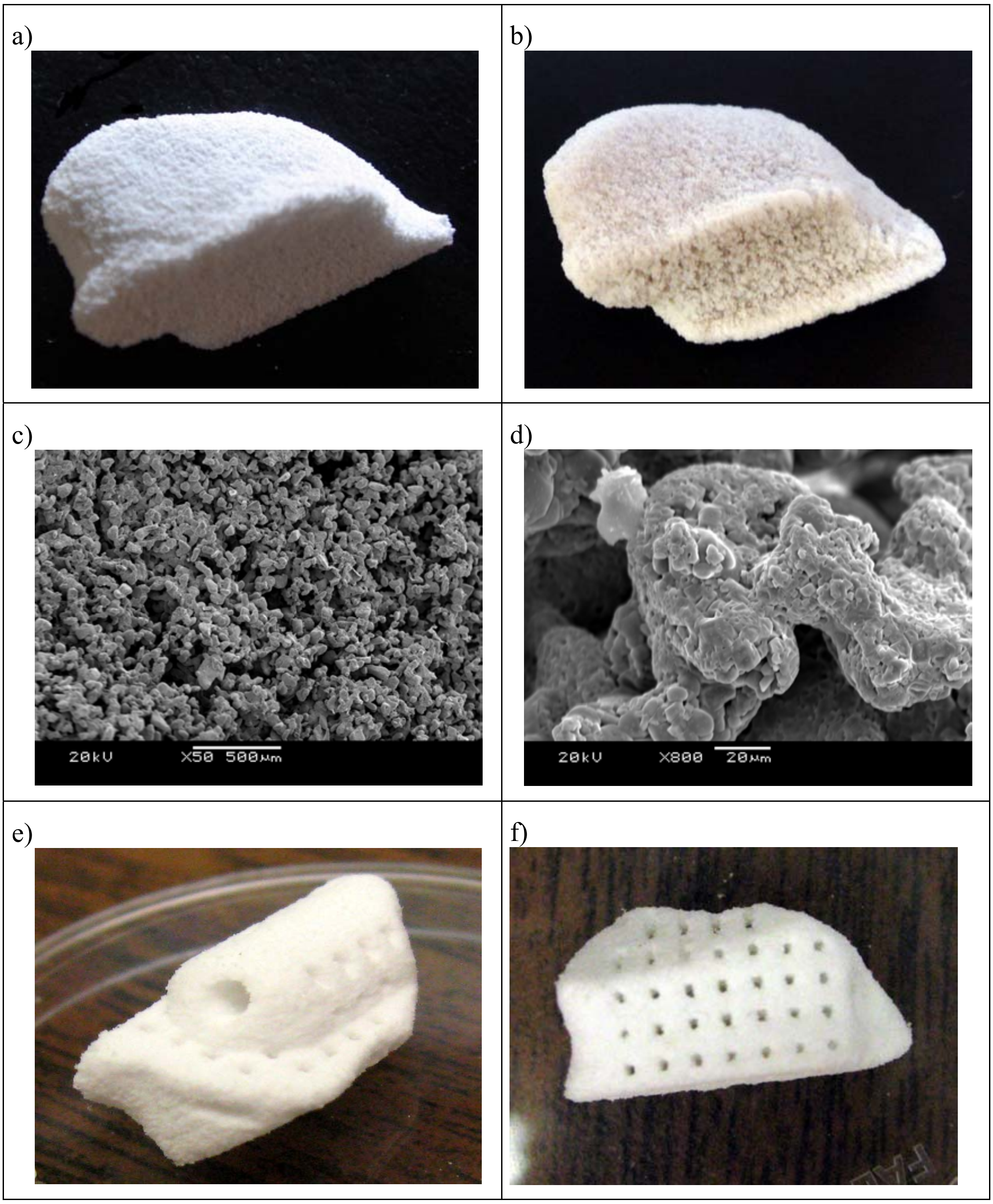

Figure 3-23: Complex CPP sample produced using the direct-3DP method: a) pre-shaped sample, b) sintered sample, c) SEM images of the sintered sample at 50× magnification, d) SEM images of the sintered sample at 800× magnification, e) and f) samples with 500 µm channels.

## 3.4 Dimensional Accuracy Study of Three-Dimensional Printing

While fabricating components directly from the ZPrinter®, it was observed that the actual dimension deviated from the specified dimension. Therefore, an investigation was conducted to determine the dimensional accuracy of 3DP technology. The objective of this study is solely to evaluate the performance capabilities in terms of achievable accuracy of the 3DP process as implemented by Z-Corporation. The following sections discuss the methodology employed in this investigation, which involves developing benchmark models, fabricating parts, and measuring and recording the designed features. A statistical analysis of the measured data will be presented in Section 3.4.3. It is important to note that all the results presented in the following sections are exclusively for the combination of Z-Corporation's ZPrinter® 310 Plus, the default plaster-based powder, and the aqueous-based binder. However, the same procedure discussed below can be implemented to study the dimensional and geometric accuracy of the directly-fabricated CPP parts if material is available.

### 3.4.1 Benchmarking Approach and Development

The use of benchmarking is a common procedure employed for all kinds of high productive equipment to evaluate various aspects of a process with respect to a best practice. The objective of benchmarking can differ from one scenario to another. In this investigation, new benchmark models were developed. The developed benchmark models represent characteristics to be investigated in order to evaluate the performance capabilities regarding dimensional accuracy of Z-Corporation's 3D printer.

To examine the dimensional accuracy, a range of small, medium, and large part dimensions were considered. The benchmarking part was designed to have a dimension of 20.0 × 20.0 × 10.0 mm. The physical features chosen were protrusions and rectangle cavities of varying lengths with nominal dimension of 2.0, 2.5, 4.0, 12.0, and 20.0 mm as shown in Figure 3-24. The 4.0 × 2.0 mm protrusion located on the bottom left corner was designed to properly indicate the x- and y-building axes.

This benchmark design was also used to evaluate the effect of temperature, relative humidity, and part location within the workspace on dimensional accuracy of the fabricated parts.

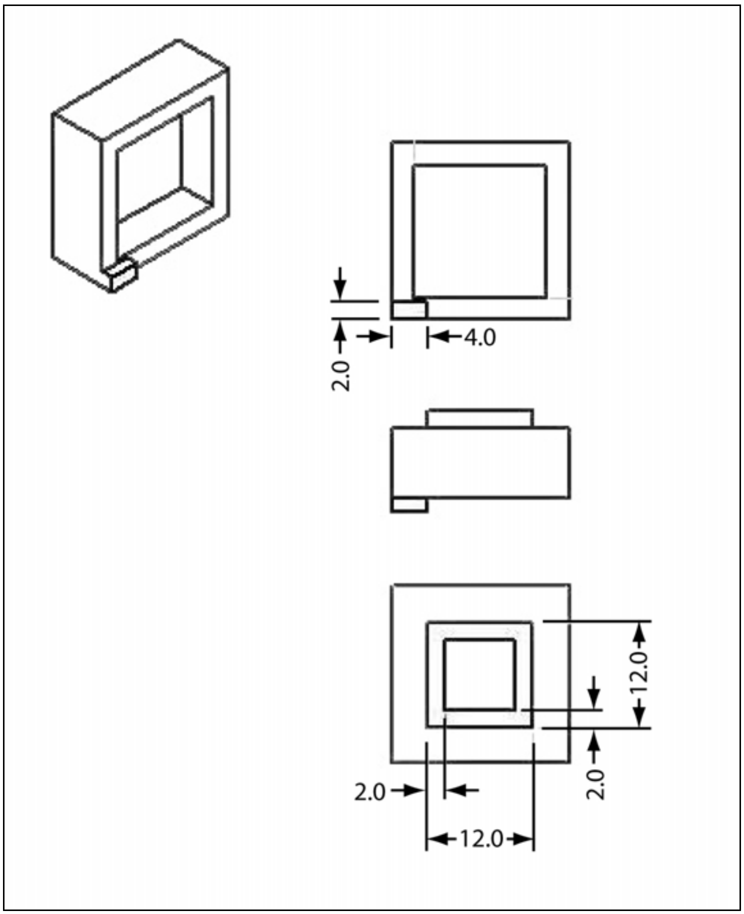

Figure 3-24: Benchmark #1 dimensions.

### 3.4.2 Experimental Procedure

#### 3.4.2.1 Machine Setup

All of the benchmark models were modelled in SolidWorks® (SolidWorks Corp., Concord, MA, USA) and fabricated using the same equipment and setup as described in Section 3.2.1.3.1.

#### 3.4.2.2 Measuring Procedures

Since it is rather difficult to eliminate human errors, a measurement protocol was designed to reduce the variation and careful attention was given to it during the execution of the experiments. To be consistent, all parts were removed from the printer 12 hours after the building process was complete. Due to the nature of the 3DP-fabricated parts, an excess force erected on the part may cause an impression and thus resulting in inaccurate readings. As a result, the measurements were taken carefully with the same person to ensure consistency. In addition, for every nominal dimension, three readings were taken at various locations and averaged to obtain the final value.

The linear dimensions were obtained by using a digimatic caliper (Series 500, Mitutoyo Corp., Kawasaki, Japan). The resolution is 0.01 mm (0.005") and the accuracy as specified by the manufacturer is ±0.02 mm (±0.01") [101]. The temperature and relative humidity readings were measured by using the thermohygrometer (HI 8064, Hanna Instruments®, Woonsocket, RI, USA). The accuracy as specified by the manufacturer is ±0.4°C for the temperature and ±2% for the relative humidity [102].

### 3.4.3 Results of Dimensional Accuracy Analysis

A picture of the 3DP-fabricated part using the default system material is shown in Figure 3-25. The surface appears to be smooth after the removal of the unbound powder, but there is evidence of loose powder.

Figure 3-25: Sample of 3DP-fabricated parts showing the surface finish.

#### 3.4.3.1 Nominal Dimension versus Deviation

The error measurements for different nominal dimensions in the x- and y-direction are summarized Table 3-12. Figure 3-26 and Figure 3-27 provide graphical illustrations of the distribution of these errors (see Appendix B for data and calculations). By applying linear regression to the measured data, two linear fits were obtained, which relate the measured dimension to the designed dimension in x- and y-direction as follow,

$$x_{\text{expected}} = 1.0057\, x_{\text{designed}} + 0.1106,\ R^2 = 0.9998 \tag{3.7}$$

$$y_{\text{expected}} = 1.0059\, y_{\text{designed}} + 0.15,\ R^2 = 0.9999 \tag{3.8}$$

Theoretically, based on these equations, one can determine calibration factors to compensate for the possible deviation one might anticipate in the produced part, thus producing a more dimensional accurate part. For example, if an x nominal dimension of 10 mm is desired, then the expected dimension can be calculated using Equation (3.7) to be 10.1676 mm. Having the designed and the expected values, an anisotropic scaling factor can be calculated based on the following equation to be 1.01676.

$$\text{Anisotropic scaling factor} = \frac{\text{Real dimension}}{\text{Designed dimension}} \tag{3.9}$$

This value can be employed in the ZPrinter® software to correct for the slight deviation inherent in the 3DP process when using the default material system and bring parts into true scale.

Table 3-12: Benchmark #1 measurement showing 3DP-fabricated part accuracy.

| | Design Nominal Dimension [mm] | n (# of samples) | Measurement Median [mm] | σ (standard deviation) [mm] | Error Median [mm] |
|---|---|---|---|---|---|
| x | 2 | 30 | 2.11 | 0.0486 | 0.11 |
| | 2.5 | 78 | 2.61 | 0.0656 | 0.11 |
| | 4 | 30 | 4.08 | 0.0590 | 0.08 |
| | 12 | 30 | 12.39 | 0.0909 | 0.39 |
| | 15 | 24 | 15.19 | 0.1037 | 0.19 |
| | 18 | 12 | 18.18 | 0.1230 | 0.18 |
| | 20 | 36 | 20.15 | 0.0488 | 0.15 |
| | 35 | 6 | 35.30 | 0.1133 | 0.30 |
| y | 2 | 60 | 2.17 | 0.0931 | 0.17 |
| | 2.5 | 78 | 2.64 | 0.0560 | 0.14 |
| | 12 | 30 | 12.24 | 0.0616 | 0.24 |
| | 18 | 24 | 18.30 | 0.0824 | 0.30 |
| | 20 | 36 | 20.28 | 0.0628 | 0.28 |
| | 30 | 12 | 30.33 | 0.1029 | 0.33 |
| | 43 | 6 | 43.29 | 0.0497 | 0.29 |

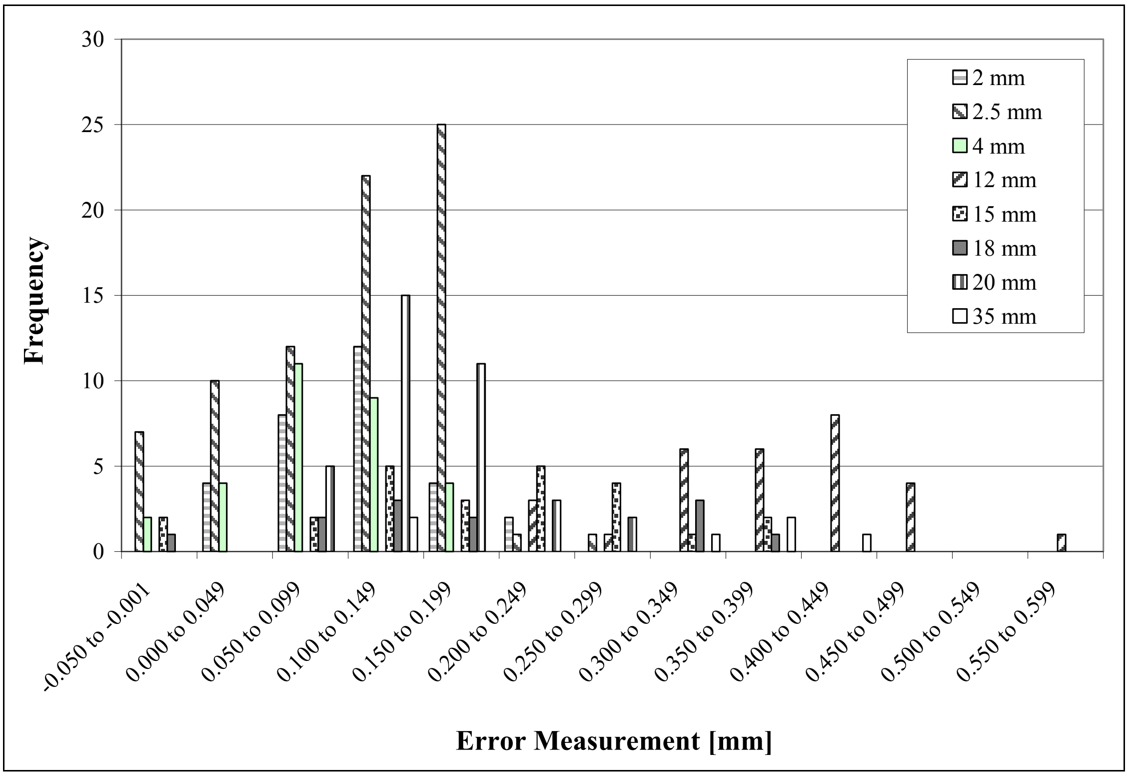

Figure 3-26: Error distribution for different normal dimensions in the x-direction.

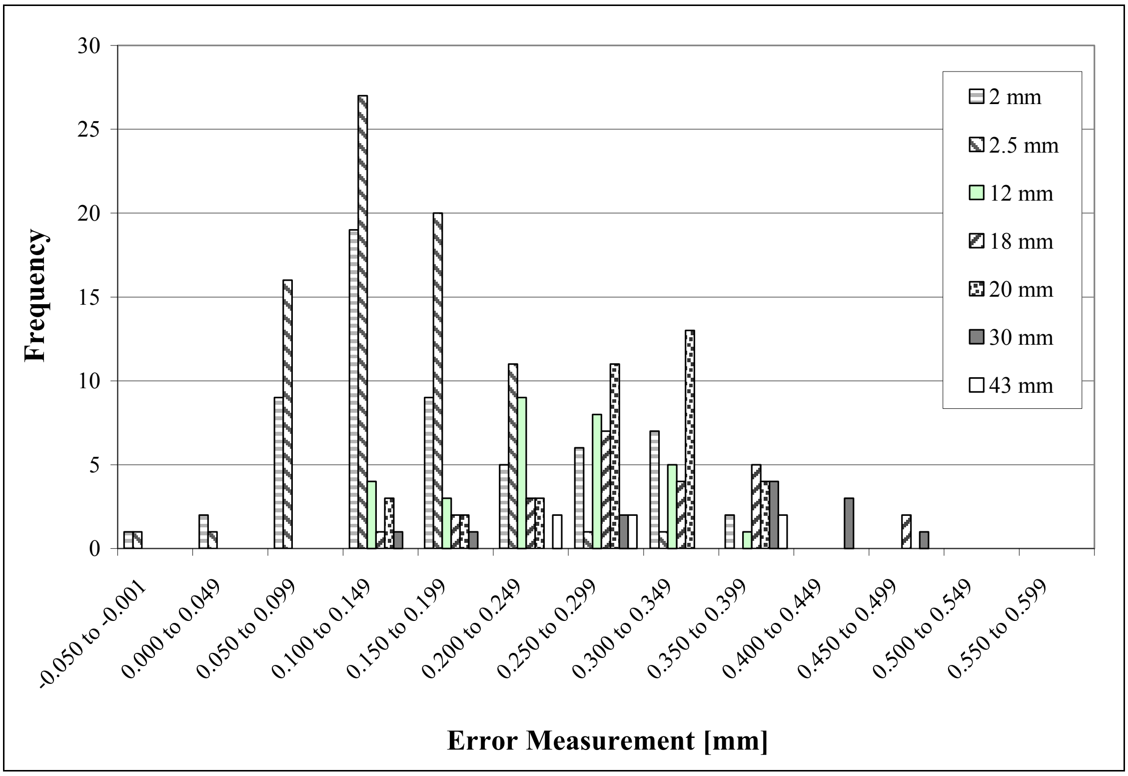

Figure 3-27: Error distribution for different normal dimensions in the y-direction.

#### 3.4.3.2 Temperature and Relative Humidity versus Deviation

From benchmark #1, the effects of temperature and relative humidity on the dimensional accuracy of the fabricated parts were also studied. It was observed during the experiment that temperature and relative humidity vary inverse proportionally to each other. Figure 3-28 presents the relationship between dimension deviation and temperature. As seen, the dimensional errors in both directions are fairly constant across a range of operating average temperatures. In addition, the result suggests that as the operating temperature increases, the y-direction errors increases.

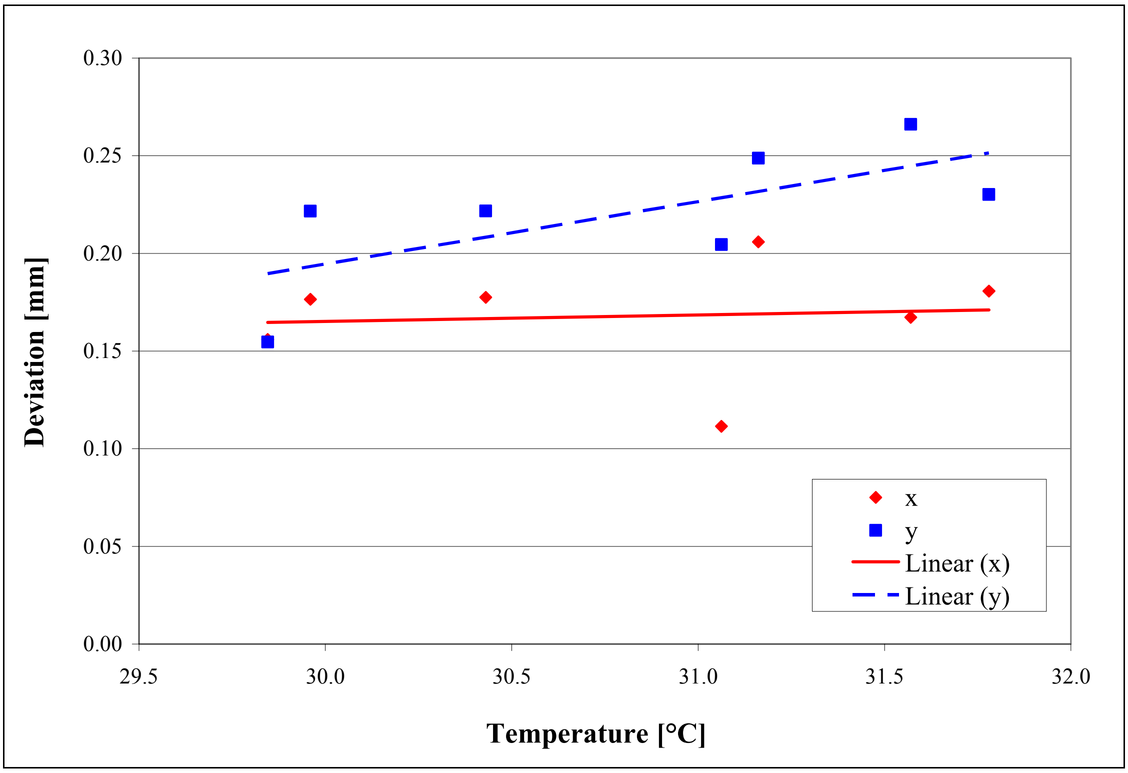

Figure 3-28: Temperature versus dimension deviation.

As seen in Figure 3-29, errors in both axes are fairly consistent across a range of humidity readings. However, the data points do not indicate any obvious pattern. Based on these results, there was not enough evidence to establish a link between operating temperature and relative humidity with the dimensional errors. As the temperature and relative humidity fluctuate during experiments, it is suspected that they will only influence the curing process [98]. In addition, without giving the permission to adjust these settings on commercialized ZPrinter®, it is not feasible to use these parameters to control the process accuracy.

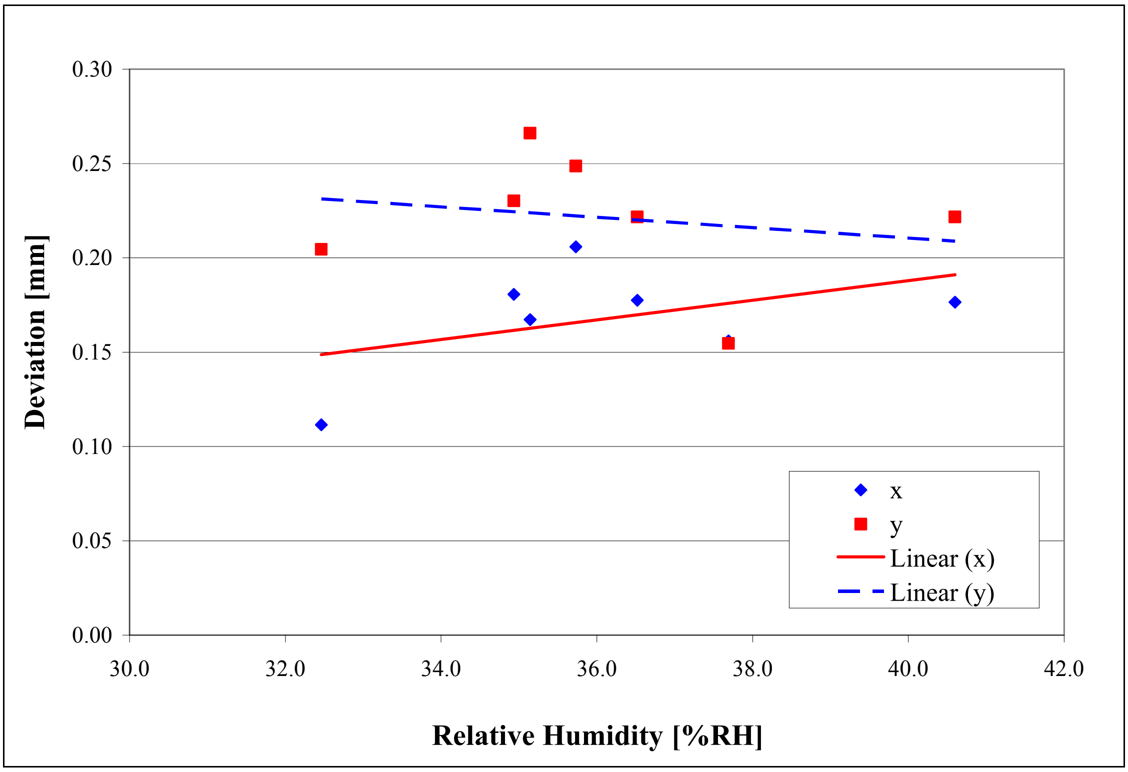

Figure 3-29: Relative humidity versus dimension deviation.

## 3.5 Discussion

### 3.5.1 Indirect- versus Direct-3DP Fabrication Methods

In this thesis, two rapid prototyping methods, indirect- and direct-3DP, were used to fabricate CPP substrates. It is a milestone for many researchers in the regenerative medicine field to develop a solvent-free and aqueous-based system for fabricating substrates [57]. Therefore, the direct-3DP method is also the ultimate interest of this study. The most important feature that the direct method provides is its capability in producing components with any pre-determined shape as complex as the freeform surfaces obtained from CAT scan images (Figure 3-23a, b, e, and f). The fact that it does not rely on user skills for the successful of fabrication makes this process even more attractive. In addition, the direct method has been reported to provide precise control of the pore size, interconnectivity, and the distribution of pores within the scaffolds [53][57]. This is also verified by the findings in this study as can be seen in Figure 3-18b, Figure 3-19b, Figure 3-21b, and Figure 3-22b.

There are many intrinsic difficulties that exist in the indirect-3DP method, particularly during the casting stage of the process. One major problem encountered during the preliminary study of the indirect-3DP method involved hindrance in mold removal and cleaning of the pre-shape sample. It was observed that if the samples were not dried sufficiently, there would be a high tendency of them sticking to the mold walls and breaking apart during mold removal. Therefore, to make sure this problem does not occur, a drying process (Section 3.2.1.4) was designed based on trial and error and was employed during this investigation. Another type of defect that was observed was differential thickness along the length of the samples (Figure 3-8a, Figure 3-12a, and Figure 3-14a). It was assumed that the manual-filling of CPP paste into the molds could generate a significant amount of variation in the pre-shaped parts due to human error. Possible causes may be uneven mechanical stresses applied during filling or stresses caused by the weight of the sample. It is also speculated that during drying, liquid migrates through the pores of the plaster molds. If the mold changes its shape due to the uneven absorption of the liquid, then the final shape of the sample might alter depending on the rate of liquid absorption and the rate of drying and paste settling. In addition to that, differential shrinkage can occur as a result of differing in liquid content, which can possibly introduce cracks within the pre-shaped structure.

Several other defects might also occur during the process of filling the molds. For example, air bubbles might be entrapped in the paste and instigate voids. It can be seen from the SEM images (Figure 3-10b and Figure 3-14a) that voids are found in the sintered structure. Although the reason that causes these voids cannot be confirmed to be air bubbles within the pre-shaped samples, it is possible that the imperfection of the paste-filling process hinders the quality of the sintered CPP samples. Drying of the paste during filling can also cause changes in the paste consistency, which can introduce undesired microstructural defects. In addition to the defects described above, microscopic defects can be produced by paste contamination and incomplete dispersion of material during mixing.

In the feasibility studies of the direct-3DP method, several material systems were looked into in order to develop a novel powder-binder system with the intention to directly incorporate CPP into the printer. From the process point of view, 3DP requires a powder with good flowability and spreadability and a controlled particle size distribution, as well as a binder with adequate consistency and viscosity to provide suitable and strong interaction with the powder.

In terms of the selection of powder, it has been observed that powder preparation is very crucial in the success of powder spreading. It is important to have a good controlled of powder particle size distribution. The size distribution can affect packing and compaction of the powder, which ultimately alters the amount of powder being spread at a time. This can also influence the porosity of the final sintered samples. With the current capacity of the printer, the degree of compaction can only be controlled by manually compressing the powder into a tighter compact during powder filling into the powder compartment. This process reflects additional source of human error. The differential compaction in powder layer can change the amount of powder being distributed, resulting in dimensional inaccuracy or density gradient. Purity is also another important issue owing to its influences on the sintering process. It usually acts as flaw and can generate further defects during high-temperature treatment. The effect of impurities are depends on the size of the inclusion compared to the grain size of the ceramic and on the relative thermal expansive and elastic properties of the matrix and inclusion [103].

It has been verified empirically that CPP powder exhibit good interaction with different kinds of binders provided that the amount of binder applied is adequate. In general, they have displayed good spreadability and flowability given that the following conditions and machine parameters are in operative. In terms of powder preparation, sieving and screening need to be conducted with care conforming to the protocol. The

3D printer operates at a process velocity of 0.52 m/s and a layer thickness of 0.102 mm (0.004").

On the other hand, the selection of binder generated unanticipated obstacles. The deposition of pure grade ethanol and PVB binders were not successful to the way the printhead functions. The HP printhead operates based on a bubble jet method. The resistor in a thermal printhead generates heat in order vaporize ink and create a bubble. As the bubble expands, it forces droplets of ink out of the nozzle. When the bubble bursts, it creates a vacuum, which draws more ink into the printhead from the reservoir. Since the default binder used for the printer is aqueous-based, its boiling temperature must be approximately 100°C. Conversely, the lower boiling temperature of ethanol is believed to evaporate when heat is applied. This not only impedes binder deposition, but also generates unwanted heat and damages the printhead. Problems also occurred during switchover from the PVB binder to the aqueous-based binder. It was not anticipated that the contact of PVB binder with water would precipitate a film-like residue, which congests the tube that transports the binder.

Initially, the reason that the PVB-based binder was selected is due to the fact that CPP undergoes hydrolysis degradation when in contact with water. Despite that, the default aqueous-based binder was tested in preliminary studies. The results indicate that the use of the aqueous-binder was indeed acceptable with no side effect on CPP observed; consequently, the use of ethanol-based binder was rejected.

### 3.5.2 Sintering of Calcium Polyphosphate

The samples fabricated indirectly were prepared from two type of starting powder: fine, < 75 μm, and coarse, 106-150 μm. The average density was determined to be 66.28 ± 11.62% and 65.87 ± 6.12% for the fine and coarse samples, respectively. Using the theoretical density of CPP, the volume fraction of the pores, namely porosity, can be determined. The average volume porosities were measured to be 33.72% and 34.13% for the fine and coarse samples, respectively. The results suggest that there were predominantly open pores within the structure. This can also be confirmed by the SEM images in Figure 3-8, Figure 3-9, Figure 3-11, and Figure 3-12. As according to Kingery *et al.*, when the sintered sample has a density less than 90%, the structure contains interconnected pores [104]. In addition, these samples exhibit comparable density as the samples produced using the standard protocol. In the most recent animal study done by Kandel *et al.*, they have reported success in maintaining implants up to 9 months in sheep. The desired samples yield 30-45% interconnected porosity with a pore size of approximately 100 μm [13].

Sintering is defined as the "a thermal treatment for bonding particles into a coherent, predominantly solid structure via mass transport events that often occur on the atomic scale. The bonding leads to improved strength and a lower system energy" [105]. The type of sintering used to sinter CPP is called the solid-state sintering (SSS). The SSS is commonly comprised of a series of three stages, where unique microstructural characteristics or changes are observed. 1) During the initial stage, the particles re-arrange themselves to allow for more contact points and the formation of grain boundaries and neck can be observed (Figure 3-30). During this stage, the relative density of a part can increase due to the increase in packing of the particles. 2) In the intermediate stage, necks between the particles continue to grow and the particles move closer. In addition, grain boundaries and grains move and grow at the expense of others, resulting in shrinkage and decrease porosity. 3) The final stage involves pores closing and elimination through vacancy diffusion. Grain size increases during this stage.

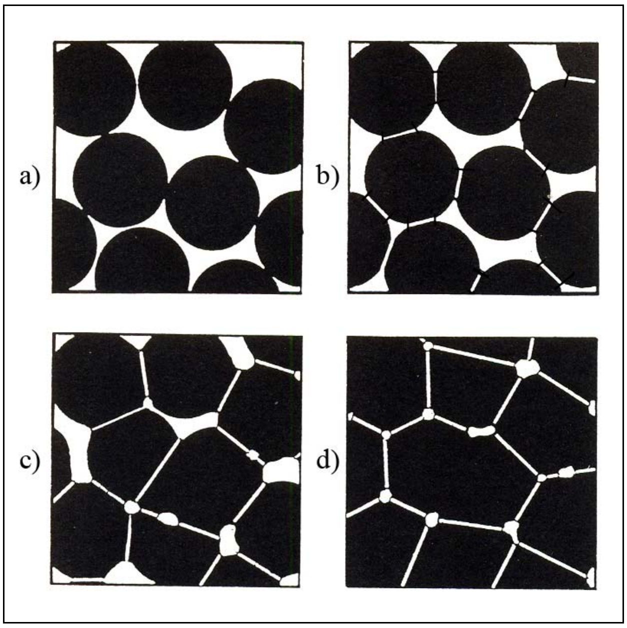

Figure 3-30: Schematic showing solid-state sintering: a) loose powder particle, b) initial stage, c) intermediate stage, and d) final stage [106].

The mass transport mechanism refers to how the mass can be transferred in response to the driving force. Typically, there are two major classes of mechanism: surface transport and bulk transport. Surface transport mechanisms include surface diffusion and evaporation-condensation. Bulk transport mechanisms include volume diffusion, grain boundary diffusion, plastic flow, and viscous flow [105][107]. Even though both mechanisms promote neck growth and contribute to bonding, the main difference, as illustrated in Figure 3-31, is that one leads to coarsening while the other leads to densification. In surface transport, coarsening takes place where the necks grow without a change in particle spacing; whereas, in bulk transport, densification occurs and pores are eliminated. These two mechanisms usually contend with one another during sintering. If coarsening dominates, both the pores and grains coarsen and get larger with time. If the atomic process that leads to densification dominates, then the pores get smaller and vanish with time and the compact shrink [107]. For an amorphous material like CPP, the mass transport mechanism is predominately viscous flow [105][106], in which densification occurs in response to the sintering stress.

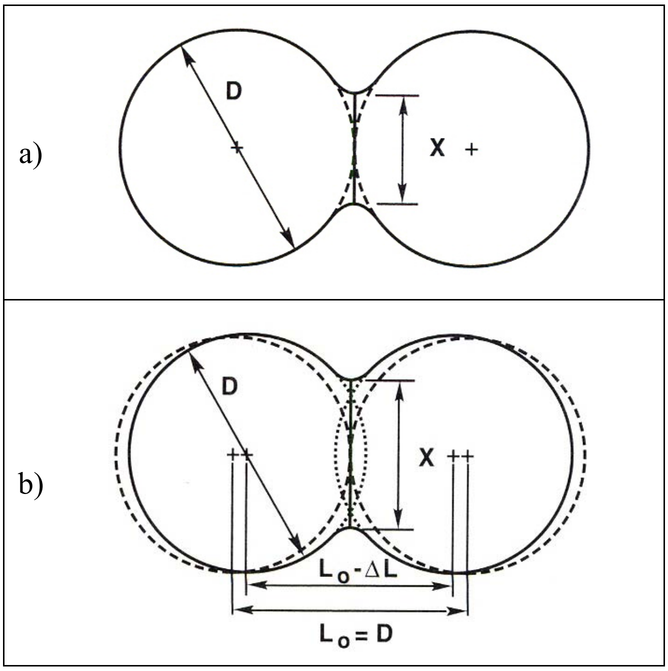

Figure 3-31: Schematic of two possible path by which particles can lower its energy. a) coarsening and b) densification.

The resulting density of a sintered sample is depended on a variety of factors including starting powder particle size, the sintering conditions used, and the packing density [108]. Foremost, by considering the two types of starting powders used in the indirect-3DP method, one would have expected to obtain a denser structure for the fine starting powder. According to the sintering concept, the driving force for sintering and the subsequent densification all require the consumption of free energy by elimination of surface area [103][107]. It is expected that when the particle size is finer, the grain size becomes smaller, resulting in a greater surface area. This presumption can be verified by the higher density obtained for the <75 μm CPP samples. In the development of any concept or equation, ideal conditions are involved to verify the basic understanding. However, in practice, various complications exist which degrade the ability to predict the outcome. This applies to solid-state sintering as well. One example of such is the particle size distribution. Most theories assume a monosized spherical powder, while most sintering in practice involves particles in a range of different sizes and often far from spherical in shape. The occurrence of irregular particles can result in a less uniform packing and anisotropic surface energy [105], which can affect the degree of shrinkage during sintering. Given that densification implies change in particle spacing, it is logical to expect the use of finer particle size would give in a more noteworthy dimensional shrinkage.

Another important factor affecting the density of the sintered samples is related to the sintering conditions operative, which includes sintering temperature, dwell time, and the heat-up rate. Densification of sintering is sensitive to sintering temperature and dwell time. At lower temperature, surface diffusion usually dominates sintering mass transport, which provides bonding without densification. Whereas, when temperature increases, densification dominates. This is confirmed by examining the density results from the direct-3DP method. At 592°C, the volume percent density is approximately 7% greater than the 585°C samples. Conversely, by exploring the results from both the indirect- and direct-3DP method, it would have been expected from sintering theory that the combination of finer powder and higher sintering temperature would yield a denser sample. Yet, this was not observed, e.g., 106-150 μm at 590°C compare to 45-75 μm at 592°C, which yield 65.87 vol% and 59.3 vol% density, respectively. Although the density is a strong function of the starting particle size and sintering temperature, other sources such as processing method and condition, packing method, and packing density all need to be considered. Due to the different methods for fabricating these samples, it is rather difficult to have a direct comparison. However, as a note, pore size and its distribution affects not only the density, but increases in capillary forces on the particles at the contact point (in the initial sintering stage), resulting in rearrangement and larger pores to grow at the expense of the smaller ones [105].

### 3.5.3 Binder Removal

The role of organic additive is essential in both the indirect- and direct-3DP fabrication methods to produce CPP substrates. These added binders remain in the pre-shaped samples to impart strength and to retain the desired shape before sintering. Such additives need to be removed completely before densification of sintering takes place. Otherwise, residues may be retained within the samples and alter the desired properties. Therefore, binder removal is one of the major steps in ceramic processing and must be controlled to eliminate distortion or cracks. The process of binder removal for the polymer binders used in this thesis is known as thermolysis, which implies thermal decomposition of the polymer binder into volatile products [104]. During thermolysis, many chemical and physical changes occur concurrently: decomposition of organic materials, chemical reactions between these materials with the surfaces of the ceramic powders, and mass transport of reactants and degradation product through binder-filled and open pores [109][110].

One of the major obstacles encountered during preliminary studies of sintering was the observation of samples became relatively grey in colour after sintering. This phenomenon was observed for the <75 μm samples made from the indirect-3DP method. During the removal process, it is common to have retention of carbonaceous residue due to minimal oxidation of the residue at lower oxygen partial pressure [110]. Polyvinyl butyral (PVB) and polyvinyl alcohol (PVA) both decompose initially by side group elimination following by scission [109]. In side group elimination, an array of low molecular weight products is produced; whereas in scission, a wide spectrum of molecular fragments that contain minimal monomer is produced [109]. During binder removal, the degradation products diffuse from the center of the sample through pores to the outer surface of the sample. The pores within these pre-shaped samples are initially open or filled with binder. When heat is applied, the open pores serve as fast diffusion path for mass transport; thus, the binder in the binder-filled pores can decompose and diffuse through these pores. As suggested by Lewis [109], when the pre-shaped sample contains less than 10 vol% of binder, the sample usually has sufficient open pores to allow degradation products to escape from the interior to the sample surface [106]. However, in this study, samples displaying carbon retention were found to have a wide range of powder sizes (<75 μm) and were fabricated from the indirect-3DP method. It was hypothesized that because a slurry containing CPP and the polymeric binder was employed, thus, the pores are mostly filled with binder. Therefore, in this case, there is an absence of connected pores initially to create a diffusion path.

The carbon residues in the samples can generate unwanted difficulties during sintering. Several authors have suggested that carbon retention can lead to insufficient sintering and cause cracking, blistering, warping, anisotropic shrinkage, and inadequate mechanical properties [109][110]. Some of these defects were observed during this study as shown in Figure 3-10 and Figure 3-14.

The amount of binder used is an important factor influencing dimensional shrinkage. During binder removal, the samples undergo shrinkage if the amount of binder being removed is much greater compared to the volume increase due to thermal expansion of the samples. Therefore, simply because more binder needs to be removed, when the amount of binder is increased in a pre-shaped sample, a more significant shrinkage is expected to occur. One way to control this undesired effect is to select optimal powder characterization and/or to modify the heating conditions [106]. During this study, a 10°C/min heat-up rate and a 3 h dwell time were used to achieve a more uniform heating in the entire sample.

### 3.5.4 Three-Dimensional Printer Accuracy

The whole purpose of part fabrication with novel advanced methods is to produce accurate parts. The benefits of a method are controversial if the parts obtained are not accurate. Hence, it is important and crucial to determine part accuracy using a reliable method from a sufficient amount of data in order to ensure accountability. In order to determine the process performance, two parameters need to be explained: accuracy and precision. The process accuracy can be evaluated by examining how close the average result is away from the set target. The amount by which the result deviates from the target indicates inaccuracy or bias. The indicator for accuracy is the mean value of the data. On the other hand, the precision of measurements and the repeatability of a process depend on how tightly clustered a set of data point is when the same measurements is repeated. The indicator for precision is the standard deviation of the data.

There are a number of factors influencing the accuracy of the 3DP process. Primarily, there are three basic process parameters including materials, scaling factors, and saturation values. However, inaccuracy due to the above factors can most often be pre-adjusted to values recommended by the system manufacturer for different materials and purposes. In practice, errors caused by the measurement process have a much higher and direct impact. For example, the measuring equipment used, the ambient conditions, the measuring procedures, as well as the time to remove parts from the machine are all important causes.

The benchmark model used to study the 3DP process with the default plaster-based powder and the aqueous-based binder was designed to give sufficient data in both the x- and y-direction at different nominal dimensions. Due to the variation in standard deviation, $\sigma$, the presence of a systematic error could be eliminated. From the preceding, it is also evident to conclude that the process accuracy depends on the nominal dimension and the printer axis responsible for that particular dimension. As the nominal dimension increases, the error median increases as well, implying that the accuracy of 3DP is based on a percentage of length. This relationship can be approximated by two linear functions as given in Equations (3.7) and (3.8), which are valuable in minimizing the expected bias in the x- and y-axis when the default plaster-based powder and the aqueous-based binder are in use.

It can be seen from Figure 3-26 and Figure 3-27 that there is a significant positive bias of the distribution, which confirms that the slight expansion inherent in the 3DP process. One possible reason that causes the parts to be larger than expected may be due to the spreading of the binder in the x-y plane. According to the concept of binder-powder bed interaction developed by the Moon *et al.*, when a binder droplet is ejected from the printhead, the high packing density of the powder causes it to remain temporarily on the surface of the powder bed [111]. Spreading then takes place until the kinetic energy of the falling droplet reaches equilibrium. Penetration of the droplet in the z-direction can happen any time during spreading. Factors that can influence the degree of binder spreading include droplet impact velocity, viscosity, and surface tension of the binder [111]. However, judging from the fact that access to regulate the droplet velocity and the surface tension are restricted, the viscosity of the binder is believed to have a greater effect owing to the fact that it can be changed depending on the shelf life stability of the binder. To verify, viscosity was measured for three different batches of binders and the readings vary from 1.13 cP to 1.40 cP. It is assumed that the change of viscosity was a result of an inadequate amount of liquid evaporated or changes in ambient temperatures in a prolong period of time. As the viscosity increases, resistance to momentum transfer when the binder droplet is compressed during spreading also increases. This phenomenon can reduce the droplet diameter, namely reducing the line width of the binder droplet [111].

Shrinkage or negative deviation in the x-direction occurred more frequently when the nominal dimensions were smaller (at 2.0, 2.5, and 4.0 mm). There were only two occurrences of shrinkage in the x-direction at the larger nominal dimensions, which happened at 15.0 and 18.0 mm. The results for the y-direction were more consistent. Shrinkage only occurred when the nominal dimensions were 2.0 and 2.5 mm. At higher nominal dimensions, ranging from 10.0 to 30.0 mm, expansion of the parts was observed. The error medians vary from 0.08 ± 0.0590 mm to 0.39 ± 0.0909 mm in the x-direction and 0.14 ± 0.0560 to 0.33 ± 0.1029 mm in the y-direction. These values appeared to be more pronounced than the values reported in literature. According to Curodeau *et al.* [71], the dimensional variation of the machine structures is approximately ± 5 to 10 μm in all three axes. In addition to that, it was noted that anisotropic dimensional deviations can be caused by the layering nature of 3DP. They have suggested an offset of -65 to -5 μm in the x-axis and ±8 μm in the y-axis [71]. Nonetheless, the values they have suggested represent the accuracy of the 3DP process, which depends only on the machine parameters such as machine frame alignment, axes of motion, and printhead controller. On the other hand, the results presented in this thesis depend not only on the machine parameters but on the material employed as well. Therefore, they are only applicable for this specific machine-material combination.

## 3.6 Conclusions

The following conclusions can be drawn based on the studies conducted in this chapter:

1. The results of this study have demonstrated the feasibility to produce porous calcium polyphosphate (CPP) substrates by the three-dimensional printing based technology with good reproducibility.

2. A six-step procedure was developed to fabricate CPP substrates indirectly via 3DP-fabricated molds for two sizes of starting powder: <75 µm and 106-150 µm. Two heat treatment processes were designed to burnout the binder, i.e., 7.4%w PVB and 92.6%w ethanol, followed by subsequent gravity sintering to produce the final porous structure. The structures appear to have homogeneous distributed and three-dimensional interconnected porosity. The produced CPP substrates display the following characteristics:

    i) Sintering of the 106-150 µm CPP samples at 590°C for one hour produced a crystalline structure with an average density of 65.87 ± 6.12%. The samples show consistency in particle size distribution.
    ii) Sintering of the <75 µm CPP samples at 582°C for one hour produced a crystalline structure with an average density of 66.28 ± 11.62%.

3. A successful four-step procedure was developed to fabricate CPP substrates with complex shape and internal passages directly from the three-dimensional printer. The 45-75 µm CPP powder were joined by an aqueous-based binder to produce substrates with any pre-determined shape. The samples display three-dimensional interconnected porosity and the pores are well-distributed over the entire samples. Particle-to-particle junctions and grain boundaries are evident which show adequate sintering.

    i) The samples sintered at 592°C for one hour produced an average density (59.33 ± 8.26%) that is comparable to the samples currently used in animal studies.
    ii) The samples sintered at 585°C for one hour produce a crystalline structure with an average density of 52.22 ± 3.76%.

4. Two anisotropic equations were derived empirically to compensate for the slight expansion inherent in the 3DP process for the default plaster-based powder and the aqueous-based binder in order to bring fabricated molds into true dimension.

# Chapter 4

# Computer Numerically Controlled Machining

## 4.1 Introduction

Machining is the most widely used manufacturing process to produce the desired shape of a component. The material removal process is well-developed for metal and various ceramic processing. However, in term of machining of biodegradable calcium polyphosphate ceramic, this is the first time to the best of the author's knowledge. Foremost, this chapter describes the mechanistic model used to predict the cutting forces. This model involves average cutting coefficients that include the contributions workpiece material, axial depth of cut, chip width, as well as cutter geometry. Subsequently, the experimental setup including the machine tool and dynamometer calibration employed to determine the cutting coefficients for CPP is presented. The experimental and the predicted cutting forces are compared to show the prediction accuracy. Lastly, scanning electron microscopy images are included to characterize the CNC machined surfaces.

## 4.2 Identification of Milling Force Coefficients for a Mechanistic Model

A milling operation is a periodic process that depends on the spindle speed and the tool geometry including the number of cutting edges and the pitch angles. The cutter, having one or more cutting edges, is held in a rotating spindle as the workpiece is fed towards it.

During this process, the cutter removes a variable amount of material for each spindle revolution, which has a tremendous impact on cutting force, vibration, and chatter. Thus, to ensure the accuracy of the chip thickness, the kinematics of dynamic milling needs to be considered. In the milling process, the instantaneous chip thickness, $h$, varies periodically as a function of the time-varying immersion and can be approximated by,

$$h\,(\phi) = c \sin \phi \tag{4.1}$$

where $c$ is the feed per tooth in [mm/rev-tooth] and $\phi$ is the angular immersion of the cutting edge. Depending on the helix angle and the shape of the end mill, the angular immersion angle along the same cutting edge varies, resulting in varying chip thickness and cutting forces. Figure 4-1 shows 2D milling cutting force direction and coordinate systems. There are three fundamental cutting forces acting on the cutting edge: tangential ($F_{\mathrm{ti}}$), radial ($F_{\mathrm{ri}}$), and axial ($F_{\mathrm{ai}}$). These forces as described in Equation (2.1) can be resolved into the feed (X), normal (Y), and axial (Z) directions as shown in the figure.

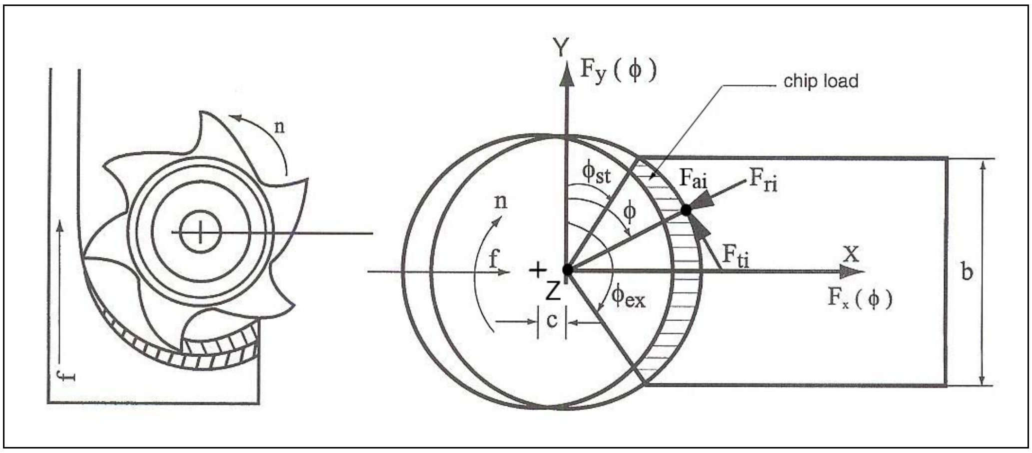

Figure 4-1: Milling cutting force direction and coordinate system [86].

$$\left.\begin{aligned} F_{\mathrm{x}}(\phi) &= -F_{\mathrm{t}}\cos(\phi) - F_{\mathrm{r}}\sin(\phi) \\ F_{\mathrm{y}}(\phi) &= +F_{\mathrm{t}}\sin(\phi) - F_{\mathrm{r}}\cos(\phi) \\ F_{\mathrm{z}}(\phi) &= F_{\mathrm{a}}(\phi) \end{aligned}\right\} \tag{4.2}$$

These forces are present only when the cutting tool is in the cutting zone, which is defined as $\phi_{\mathrm{st}} \leq \phi \leq \phi_{\mathrm{ex}}$ . $\phi_{\mathrm{st}}$ and $\phi_{\mathrm{ex}}$ are the start and the exit angles of the cut respectively. It must be noted that every cutting edge contributes to the total cutting force, and the uncut chip thickness varies at an instantaneous position of the cutter, as shown in Figure 4-1. Therefore, the total feed, normal, and axial forces can be formulated as,

$$\left.\begin{aligned} F_{\mathrm{x}} &= \sum_{j=1}^{N} F_{\mathrm{x}j}(\phi_j) \\ F_{\mathrm{y}} &= \sum_{j=1}^{N} F_{\mathrm{y}j}(\phi_j) \\ F_{\mathrm{z}} &= \sum_{j=1}^{N} F_{\mathrm{z}j}(\phi_j) \end{aligned}\right\} \tag{4.3}$$

Mechanistic modelling is a practical method used to model milling forces for a specific cutter by determining the constant parameters of the tool geometry and the tool-workpiece material. It assumes that the cutting forces, power consumed, and the torque acting on the spindle are proportional to the material removal rate. The constants can be obtained directly from slotting experiments by taking the average forces per tooth period. The average cutting forces per tooth period $\overline{F_{\mathrm{x}}}$ , $\overline{F_{\mathrm{y}}}$ , and $\overline{F_{\mathrm{z}}}$ are functions of two main components which are represented with the: i) edge force coefficients $K_{\mathrm{te}}$, $K_{\mathrm{re}}$, $K_{\mathrm{ae}}$ and ii) cutting force coefficients $K_{\mathrm{tc}}$, $K_{\mathrm{rc}}$, and $K_{\mathrm{ac}}$ as described in [87],

$$\left.\begin{aligned} \overline{F_{\mathrm{x}}} &= -K_{\mathrm{te}}S + K_{\mathrm{re}}T - \frac{c}{4}\left(-K_{\mathrm{tc}}P + K_{\mathrm{rc}}Q\right) \\ \overline{F_{\mathrm{y}}} &= -K_{\mathrm{te}}T - K_{\mathrm{re}}S + \frac{c}{4}\left(-K_{\mathrm{tc}}Q + K_{\mathrm{rc}}P\right) \\ \overline{F_{\mathrm{z}}} &= -\frac{a\mathrm{N}}{2\pi}K_{\mathrm{ae}}\left(\phi_{ex} - \phi_{st}\right) + cK_{\mathrm{ac}}\mathrm{T} \end{aligned}\right\} \tag{4.4}$$

where

$$\left.\begin{aligned} P &= \frac{a\mathrm{N}}{2\pi}\left[\cos 2\phi\right]_{\phi_{\mathrm{st}}}^{\phi_{\mathrm{ex}}} & Q &= \frac{a\mathrm{N}}{2\pi}\left[2\phi - \sin 2\phi\right]_{\phi_{\mathrm{st}}}^{\phi_{\mathrm{ex}}} \\ S &= \frac{a\mathrm{N}}{2\pi}\left[\sin \phi\right]_{\phi_{\mathrm{st}}}^{\phi_{\mathrm{ex}}} & T &= \frac{a\mathrm{N}}{2\pi}\left[\cos \phi\right]_{\phi_{\mathrm{st}}}^{\phi_{\mathrm{ex}}} \end{aligned}\right\} \quad (4.5)$$

Above, *a* is the axial depth of cut and *N* is the number of flutes of the cutter. The parameters *P*, *Q*, *S*, and *T* in Equation (4.5) remain constant for each cutting test. A set of slot milling experiments at varying feed rates but constant immersion and axial depth of cut is required. The start and the exit angles are $\phi_{\mathrm{st}} = 0°$ and $\phi_{\mathrm{ex}} = 180°$, respectively for slot milling. Therefore, each of the average cutting force can be expressed as a linear function of the feed rate and an offset contributed by the edge force component.

$$\left.\begin{aligned} \overline{F_{\mathrm{x}}} &= \overline{F_{\mathrm{xe}}} + c\overline{F_{\mathrm{xc}}} \\ \overline{F_{\mathrm{y}}} &= \overline{F_{\mathrm{ye}}} + c\overline{F_{\mathrm{yc}}} \\ \overline{F_{\mathrm{z}}} &= \overline{F_{\mathrm{ze}}} + c\overline{F_{\mathrm{zc}}} \end{aligned}\right\} \quad (4.6)$$

By combining Equations (4.4) and (4.6), the cutting force coefficients can be expressed as,

$$\left.\begin{aligned} K_{\mathrm{te}} &= -\frac{\overline{F_{\mathrm{xe}}}S + \overline{F_{\mathrm{ye}}}T}{S^2 + T^2} \\ K_{\mathrm{tc}} &= 4\frac{\overline{F_{\mathrm{xc}}}P + \overline{F_{\mathrm{ye}}}Q}{P^2 + Q^2} \\ K_{\mathrm{re}} &= -\frac{K_{\mathrm{te}}S + \overline{F_{\mathrm{xe}}}}{T} \\ K_{\mathrm{rc}} &= -\frac{K_{\mathrm{tc}}P - 4\overline{F_{\mathrm{xc}}}}{Q} \end{aligned}\right\} \quad (4.7)$$

## 4.3 Simulation of Cutting Forces

Using the empirically obtained cutting coefficients, cutting forces were simulated via two approaches. For a simple flat-end mill, an algorithm was developed in MatLAB (R2006a, The MathWorks Inc., Natick, MA, USA) to compute the forces. However, for a more complex cutter such as a ball nose end mill, CutPRO (7.0, Manufacturing Automation Laboratories Inc., Vancouver, BC, Canada), a cutting process simulation and measurement software was used.

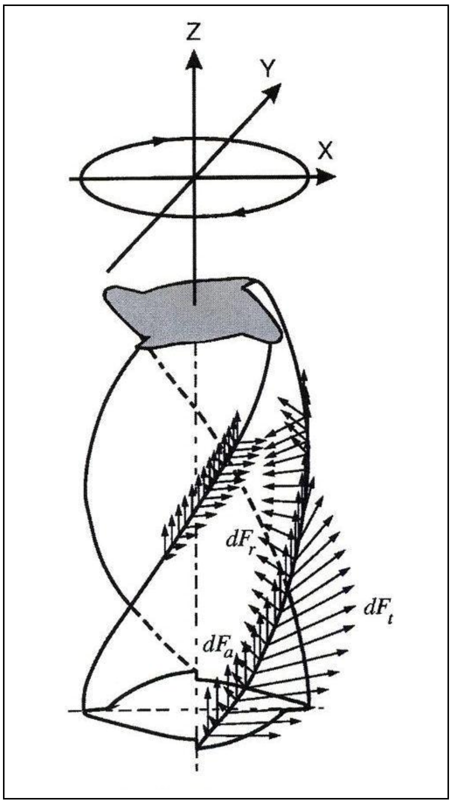

Figure 4-2: 3D end mill with incremental force acting along the flute of a cutter [86].

The cutting force prediction uses the kinematics of milling as the algorithm where the differential cutting forces acting on a discretized cutting edge with a height of *dz* in the tangential, radial, and axial direction are expressed as [86][112]:

$$\left.\begin{aligned}\mathrm{d}F_{\mathrm{t},j}(\phi,z)&=\left[K_{\mathrm{te}}+K_{\mathrm{tc}}h_j\left(\phi_j(\mathrm{z})\right)\right]dz\\\mathrm{d}F_{\mathrm{r},j}(\phi,z)&=\left[K_{\mathrm{re}}+K_{\mathrm{rc}}h_j\left(\phi_j(\mathrm{z})\right)\right]dz\\\mathrm{d}F_{\mathrm{a},j}(\phi,z)&=\left[K_{\mathrm{ae}}+K_{\mathrm{ac}}h_j\left(\phi_j(z)\right)\right]dz\end{aligned}\right\}\tag{4.8}$$

where $h_j\left(\phi_j(\mathrm{z})\right)$ is the uncut chip thickness normal to the cutting edge and varies with the position of the cutting edge. The cutting forces are separated into edge ($K_{\mathrm{te}}$, $K_{\mathrm{re}}$, $K_{\mathrm{ae}}$) and cutting ($K_{\mathrm{tc}}$, $K_{\mathrm{rc}}$, $K_{\mathrm{ac}}$) components. They can be obtained from orthogonal to oblique cutting transformation or mechanistically as presented in Section 4.2. To analytically model the cutting forces, one must consider the geometry of the cutter. For a helical end mill, the helix angle $\beta$, diameter of $D$, and number of flutes $N$ is known. By designating the bottom end of one flute $j$ = 0 and at the elevation $z$ = 0 as the reference, the rotation angle is $\phi$. At any other axial depth of cut $z$, there is a lag angle $\psi$ due to helix, where $\psi = k_\beta z$ and $k_\beta = (2\tan\beta)/D$. Therefore, the immersion angle for flute $j$ at an axial depth of cut $z$ can be obtained as [86]:

$$\phi_j(z)=\phi+j\phi_p-k_\beta z \tag{4.9}$$

where the cutter pitch angle is $\phi_p = 2\pi/N$. The differential cutting forces are integrated along the in-cut portion ($\phi_{\mathrm{st}} \leq \phi \leq \phi_{\mathrm{ex}}$) of the flute $j$ to compute the cutting forces produced by the flute:

$$F_q\left(\phi_j(z)\right)=\int_{z_{j,1}}^{z_{j,2}} dF_q\left(\phi_j(z)\right)dz\,,\ q=x,y,z \tag{4.10}$$

where the upper and lower bound $z_{j,2}$ and $z_{j,1}$ are axial engagement limits of the in-cut portion of flute $j$.

$$\left.\begin{aligned}
F_{x,j}\left(\phi_j\right) &= \left\{ \frac{c}{4k_\beta}\left[-K_{\mathrm{tc}}\cos 2\phi_j(z) + K_{\mathrm{rc}}\left[2\phi_j(z) - \sin 2\phi_j(z)\right]\right.\right. \\
&\qquad \left.\left. + \frac{1}{k_\beta}\left[K_{\mathrm{te}}\sin\phi_j(z) - K_{\mathrm{re}}\cos\phi_j(z)\right]\right\}_{z,1(\phi_j(z))}^{z,2(\phi_j(z))} \\
F_{y,j}\left(\phi_j\right) &= \left\{ \frac{-c}{4k_\beta}\left[-K_{\mathrm{tc}}\left(2\phi_j - \sin 2\phi_j\right) + K_{\mathrm{rc}}\cos 2\phi_j\right]\right. \\
&\qquad \left. + \frac{1}{k_\beta}\left[K_{\mathrm{te}}\cos\phi_j(z) + K_{\mathrm{re}}\sin\phi_j(z)\right]\right\}_{z,1(\phi_j(z))}^{z,2(\phi_j(z))} \\
F_{z,j}\left(\phi_j\right) &= \left\{ \frac{1}{k_\beta}\left[K_{\mathrm{ac}}c\cos\phi_j(z) - K_{\mathrm{ae}}\phi_j\right]\right\}_{z,1(\phi_j(z))}^{z,2(\phi_j(z))}
\end{aligned}\right\} \qquad (4.11)$$

The cutting forces contributed by all the flutes of the cutter are then summed to obtain the total instantaneous forces on the cutter at immersion $\phi$ as described in Equation (4.3) [86].

## 4.4 Experimental Results

### 4.4.1 Setup

75% dense CPP with a dimension of 20.0 × 20.0 × 10.0 mm blocks were prepared at the University of Toronto by methods described in Section 2.1.1. The blocks were milled using a 2.381 mm (3/32") diameter tungsten carbide cylindrical flat-end mill (Figure 4-3) on a 3-axis CNC machining center (OKK MCV-410, Gross Machinery Group, Brampton, ON, Canada). The experimental setup is shown in Figure 4-4. The spindle speed was fixed at 2500 rpm. The tool has a helix angle of 30°, relief angle of 12°, and clearance angle of 25°. The axial width of cut was kept constant at 1.191 mm (3/64") for each cut. The configuration is shown in Figure 4-5. Cutting tests at every layer were conducted at the feed rates in the following order from Cut 1 to Cut 8 at 0.04, 0.03, 0.02, 0.015, 0.01, 0.04, 0.02, and 0.01 mm/tooth. Thirty-two slot milling ($\phi_{st}$ = 0° and $\phi_{ex}$ = 180°) tests were conducted to evaluate the cutting coefficients. The average forces were measured using a three component table dynamometer (Kistler Instrument Corp., Amherst, NY, USA) and the data were collected using digital oscilloscope (54621D 2+16 Channel, 60 MHz Mixed-Signal Oscilloscope, Agilent Technologies, Santa Clara , CA, USA).

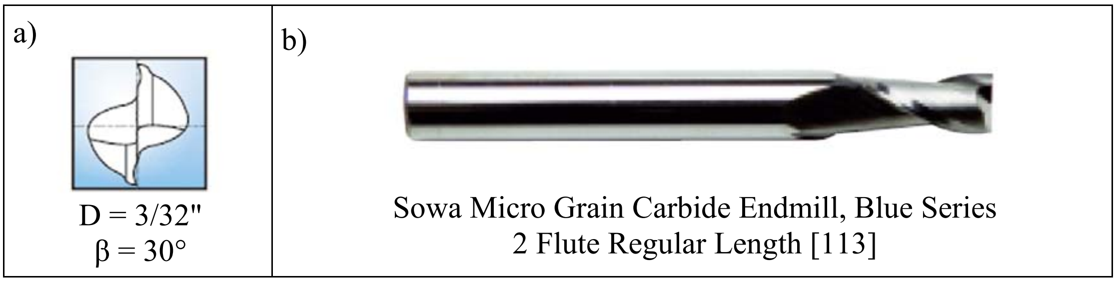

D = 3/32"
β = 30°

Sowa Micro Grain Carbide Endmill, Blue Series
2 Flute Regular Length [113]

Figure 4-3: Two-fluted flat-end mill used in slotting of CPP: a) schematic and b) the actual cutter.

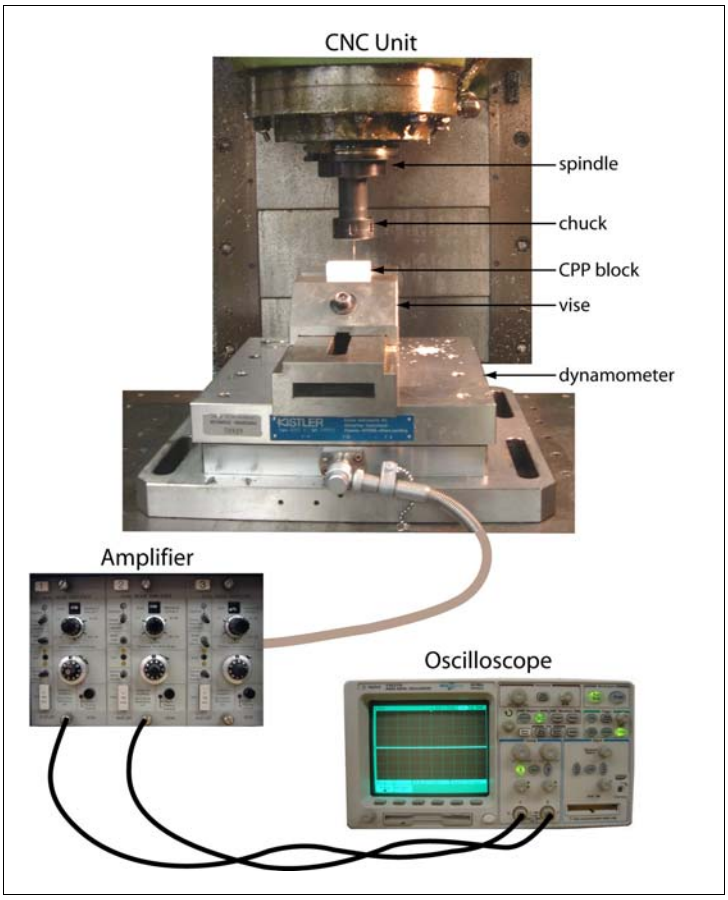

Figure 4-4: Experimental setup.

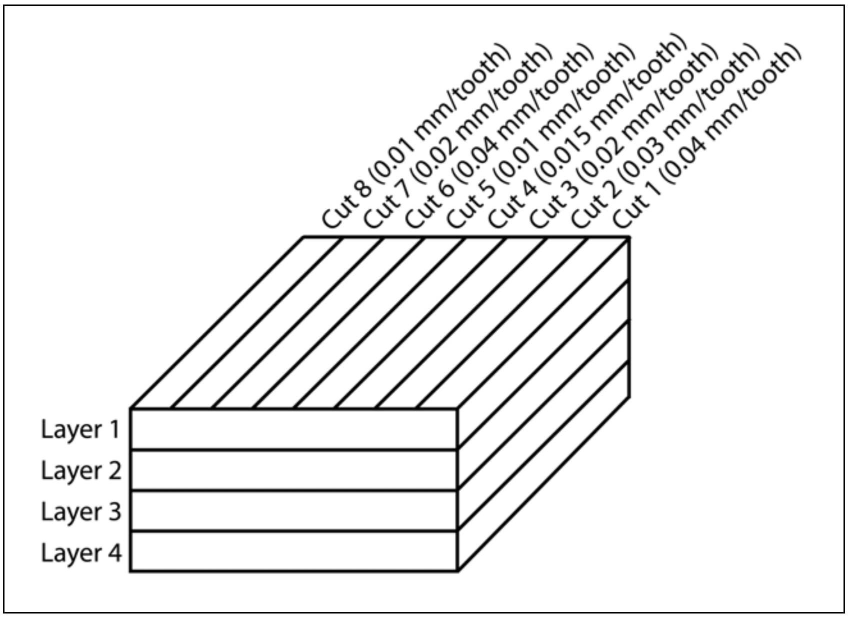

Figure 4-5: Cutting configuration of CPP block.

### 4.4.2 Dynamometer Calibration

To calibrate the static gains of the dynamometer in the range of small force, i.e., 0 to 50 N in the x- and the y-directions, known weights were hung from a pulley system, as shown in Figure 4-6. The readings were recorded and linear regression was applied to obtain a calibration curve to compensate for measurement inaccuracies.

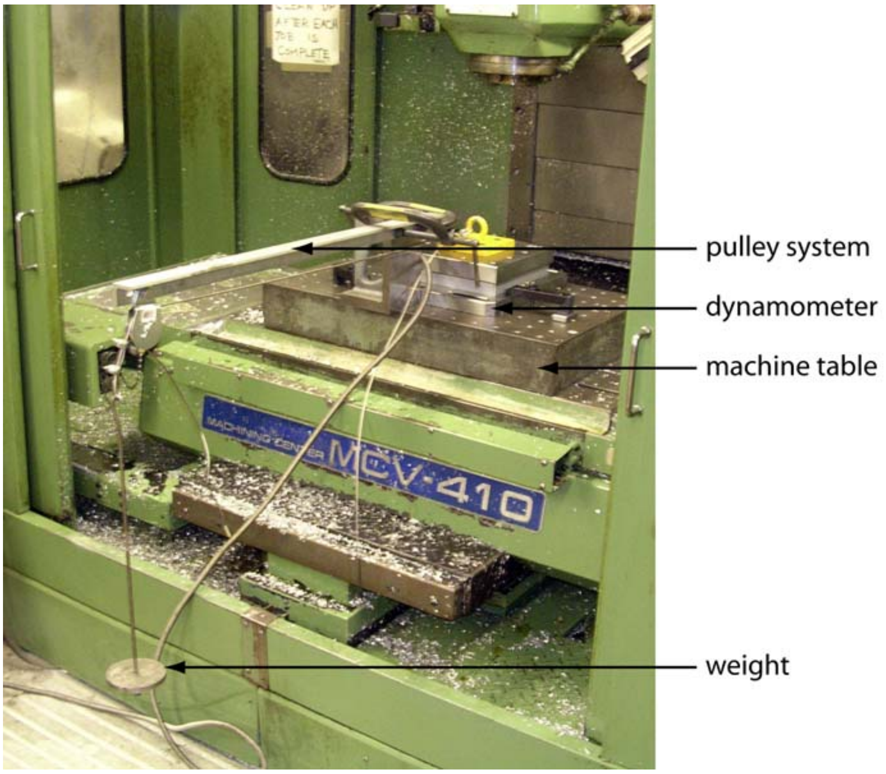

Figure 4-6: Setup for calibrating the dynamometer.

Sixteen different weights were applied and the corresponding voltage measurements were recorded using the oscilloscope (see Appendix C for the data). The charge amplifier was set to convert 50 N into 1 V and the oscilloscope probe had a unity gain. Two equations were obtained by curve fitting the data. These equations were solved for to calibrate the measured cutting forces.

$$x_{measured}\ [V] = 0.0195\ x_{applied}\ [N] - 0.0207,\ R^2 = 0.9942 \quad (4.12)$$

$$y_{measured}\ [V] = 0.0199\ y_{applied}\ [N] - 0.0246,\ R^2 = 0.9954 \quad (4.13)$$

The measurement errors are 7.20% and 6.12% in the x- and y-direction respectively, with standard deviations of 3.20% and 2.23% in the mentioned order.

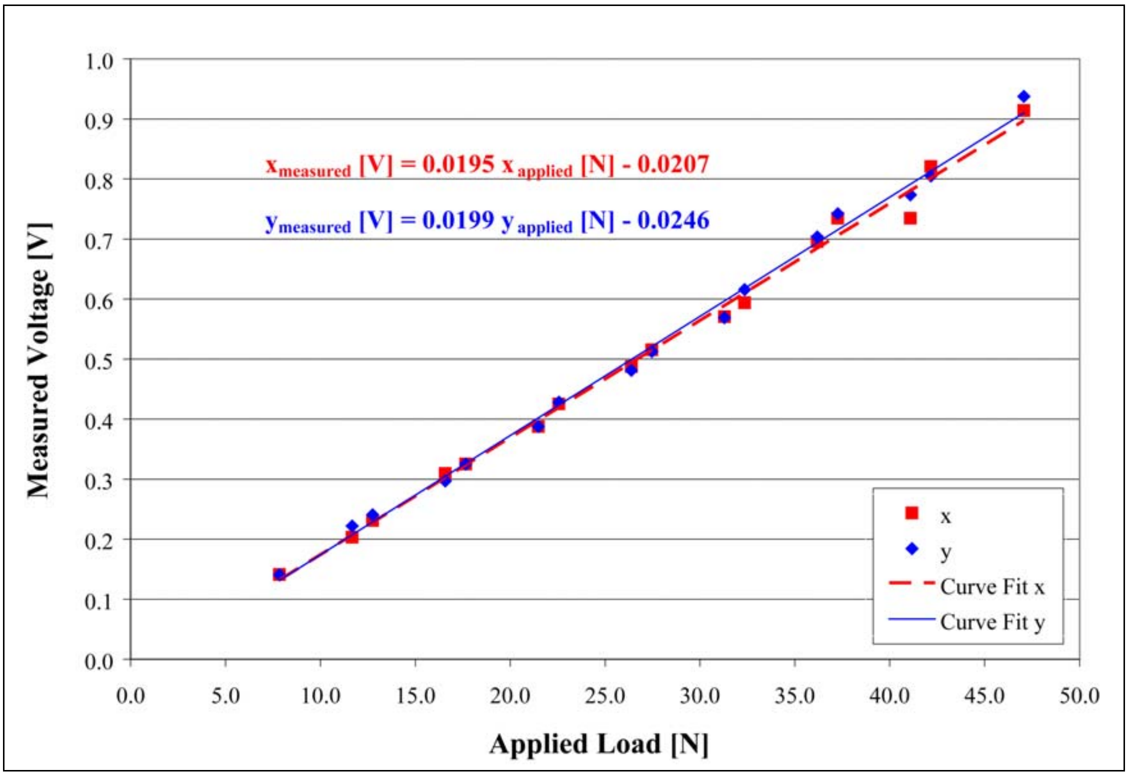

Figure 4-7: Measured load versus applied load for the dynamometer.

### 4.4.3 Cutter Run-out Inspection

Run-out is defined as the deviation of cutting edge positions with respect to the rotating center. To measure run-out, the cutter was held in the mechanical chuck of the CNC unit and a dial indicator was placed in contact with the surface of the cutting edge. As the chuck rotated through one revolution, the highest and the lowest point along the cutting edge could be determined.

In milling operation, run-out commonly occurs due to the cutter offset with respect to the center of the spindle rotation. The total indicated run-out of the router spindle was measured to be 5 µm (0.0002"). The tooth difference was measured to be 7.5 µm (0.0003"), resulting in a 2.5 µm (0.0001") run-out between the two teeth.

### 4.4.4 Identification of Cutting Coefficients

The average cutting forces were evaluated from more than 30 cutting tests for a constant depth of cut and varying feed rates. The cutting data was collected at 10 kHz sampling frequency and calibrated using Equations (4.12) and (4.13) followed by low pass filtering at five times the tooth passing frequency, in order to eliminate fluctuations caused by particle breakage [85]. A second-order butterworth filter was used with a cut-off frequency of 416.67 Hz. The average edge and cutting forces in the x- and y-directions were computed by applying linear regression. As shown in Figure 4-8, the edge forces are identified at zero feed and the slope of the lines represent the cutting forces. Figure 4-9 presents the variation of average cutting forces against varying feed rates and across the cross section of CPP. Subsequently, the shear and the edge components of cutting force coefficients were calculated using Equations (4.7). The results are presented in Table 4-1.

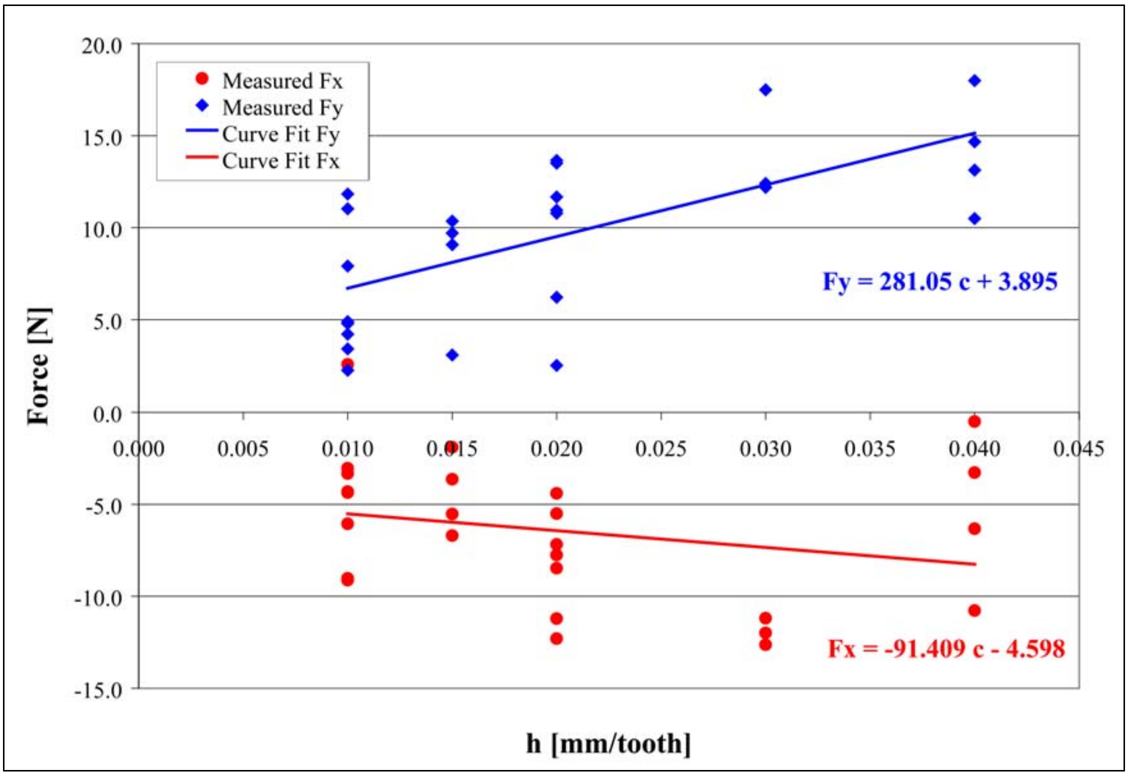

Figure 4-8: Average cutting forces for cutting 75% dense CPP block at $n = 2500$ rpm and $a = 1.191$ mm.

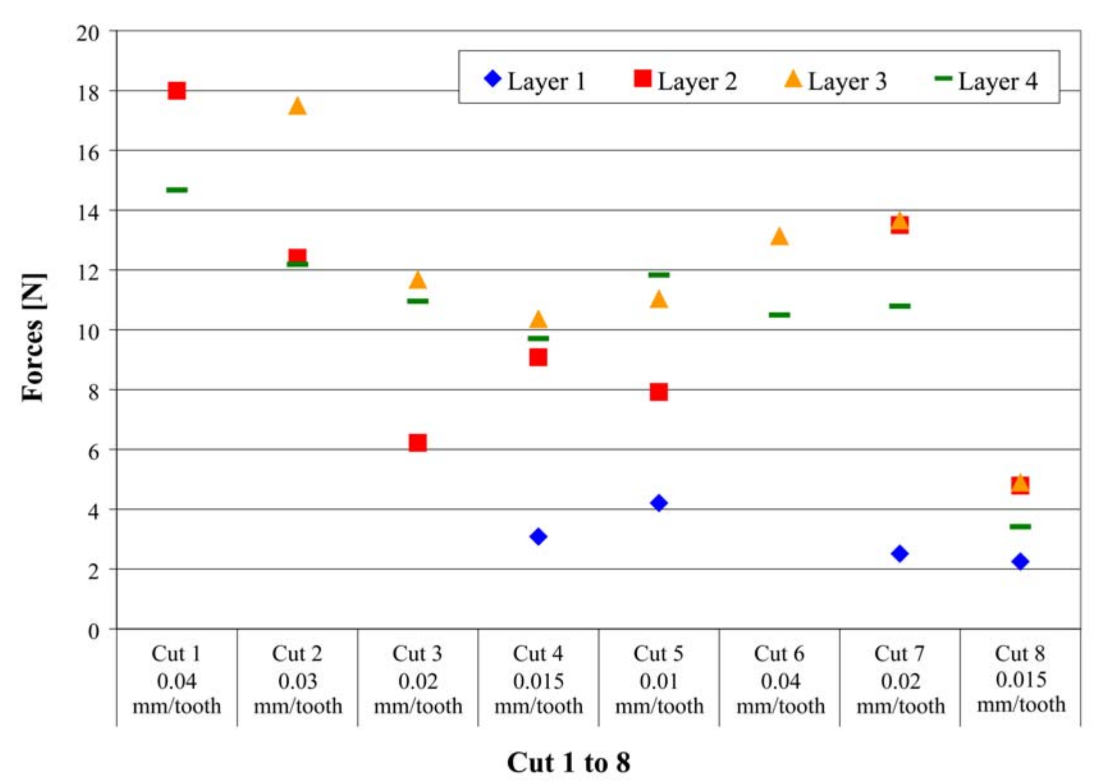

Figure 4-9: Average y-direction cutting forces showing variation across the material blank for cutting 75% dense CPP block at $n$ = 2500 rpm and $a$ = 1.191 mm.

Table 4-1: The average cutting and edge force cutting coefficients.

| Average Cutting Force | | Cutting and Edge Coefficients | |
|---|---|---|---|
| $\overline{F_{xc}}$ [N/mm] | -91.409 | $K_{tc}$ [N/mm$^2$] | 472.101 |
| $\overline{F_{xe}}$ [N] | -4.598 | $K_{te}$ [N/mm] | 5.1387 |
| $\overline{F_{yc}}$ [N/mm] | 281.05 | $K_{rc}$ [N/mm$^2$] | 153.5476 |
| $\overline{F_{ye}}$ [N] | 3.895 | $K_{re}$ [N/mm] | 6.0662 |

To verify the calculated cutting coefficients, the measured cutting data were plotted against the simulated forces in Figure 4-10 and Figure 4-11. Figure 4-10 presents the variation of milling results across the same layer horizontally, i.e., Layer 2, Cut 1, 2, 3, 4, and 5; while Figure 4-11 shows the variation of milling forces across the same position vertically, i.e., Cut 4 at Layer 1, 2, 3, and 4.

These first set of trials demonstrated the feasibility of machining CPP via conventional CNC machining. The cutting forces of CPP were measured and ascertained by conducing cutting tests. For all the cutting tests conducted, the maximum cutting forces reached were 12.63 N and 17.99 N in the x- and y-direction respectively. The cutting forces increased in magnitude when the cutter was immersed in the material blank deeper vertically, i.e., Cut 4 of Layer 1, 2, 3, and 4 as shown in Figure 4-9. This finding suggests that a variation in material properties may exist in the sintered CPP blanks. One reason could be the occurrence of warpage, which is usually a result of density variation or inadequate support that causes a part to deform during sintering. These imperfections can cause sintered samples to have variations in thickness and/or microstructure, e.g., density and porosity, across the cross sections [107]. Hence, the increase in the force magnitude is assumed to be due to the increase in the CPP density and hardness from the surface towards the core of the blank. By cross examining the above assumption with Figure 4-10 and Figure 4-11, one can observe that the measured forces across the same horizontal layer (Figure 4-10) appeared to be reasonably consistent with the simulated forces, whereas more variations were observed along the vertical layer (Figure 4-11). This further confirms the fact that the material properties remain relatively identical across the horizontal layer but differ vertically.

a)

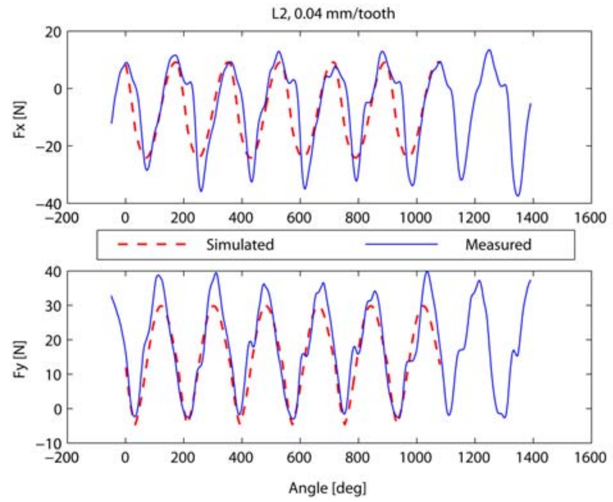
L2, 0.04 mm/tooth
Fx [N]
20
0
−20
−40
−200
0
200
400
600
800
1000
1200
1400
1600
Simulated
Measured
Fy [N]
40
30
20
10
0
−10
Angle [deg]

b)

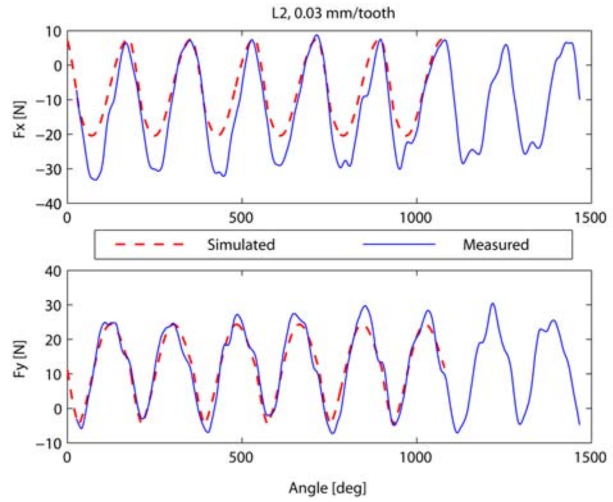
L2, 0.03 mm/tooth
Fx [N]
10
0
−10
−20
−30
−40
0
500
1000
1500
Simulated
Measured
Fy [N]
40
30
20
10
0
−10
Angle [deg]

c)

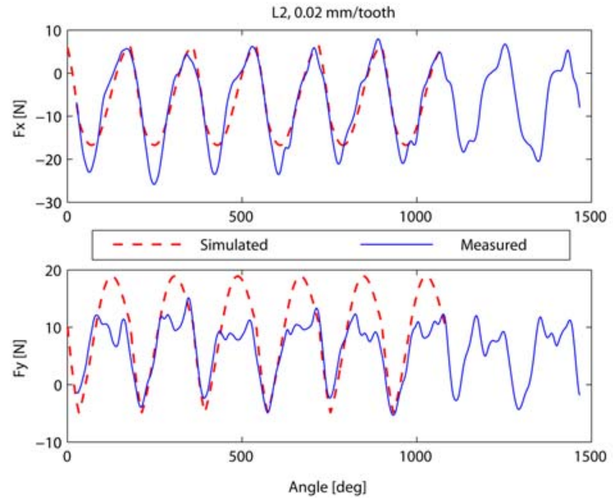
L2, 0.02 mm/tooth
Fx [N]
10
0
−10
−20
−30
0
500
1000
1500
Simulated
Measured
Fy [N]
20
10
0
−10
Angle [deg]

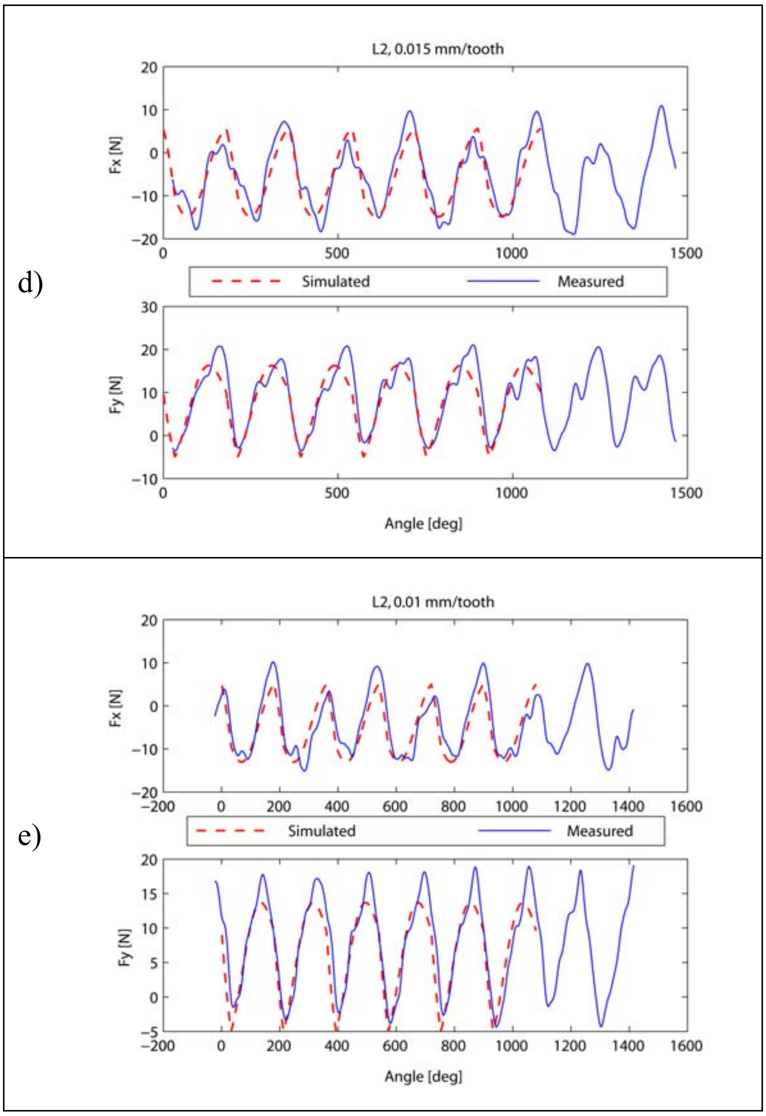

Figure 4-10: Experimental and simulation (MatLAB) results for a two-fluted flat end mill, full immersion at $n$ = 2500 rpm: a) layer 2, feed rate 0.04 mm/tooth, b) layer 2, feed rate 0.03 mm/tooth, c) layer 2, feed rate 0.02 mm/tooth, d) layer 2, feed rate 0.015 mm/tooth, and e) layer 2, feed rate 0.01 mm/tooth.

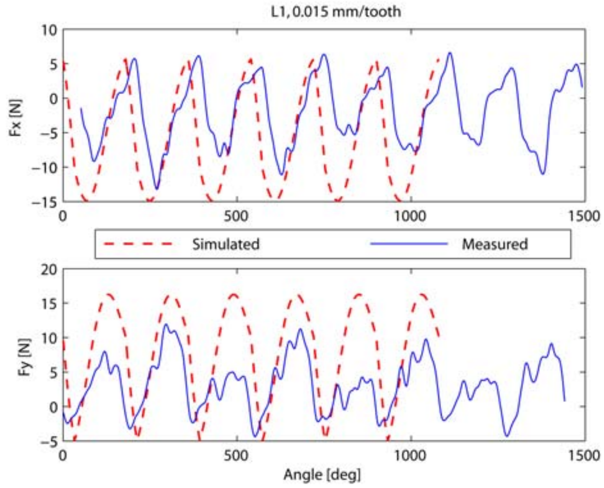
L1, 0.015 mm/tooth
Fx [N]
10
5
0
−5
−10
−15
0
500
1000
1500
Simulated
Measured
Fy [N]
20
15
10
5
0
−5
0
500
1000
1500
Angle [deg]

a)

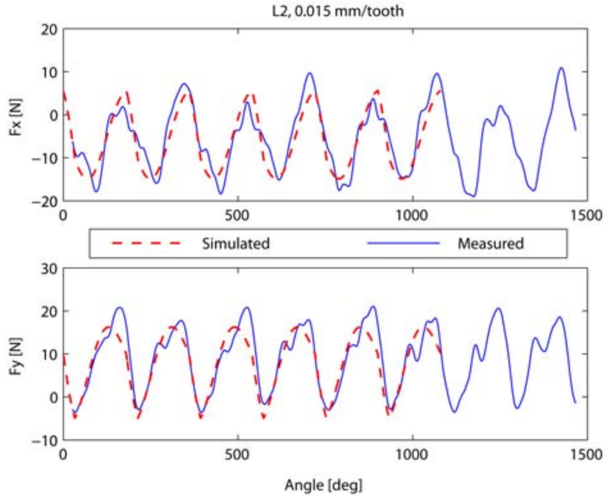
L2, 0.015 mm/tooth
Fx [N]
20
10
0
−10
−20
0
500
1000
1500
Simulated
Measured
Fy [N]
30
20
10
0
−10
0
500
1000
1500
Angle [deg]

b)

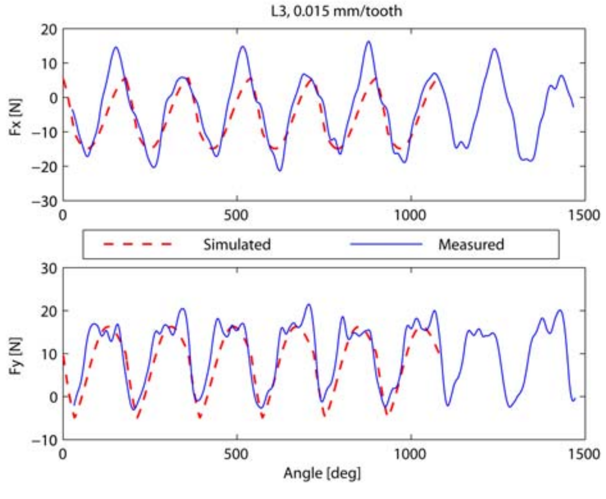
L3, 0.015 mm/tooth
Fx [N]
20
10
0
−10
−20
−30
0
500
1000
1500
Simulated
Measured
Fy [N]
30
20
10
0
−10
0
500
1000
1500
Angle [deg]

c)

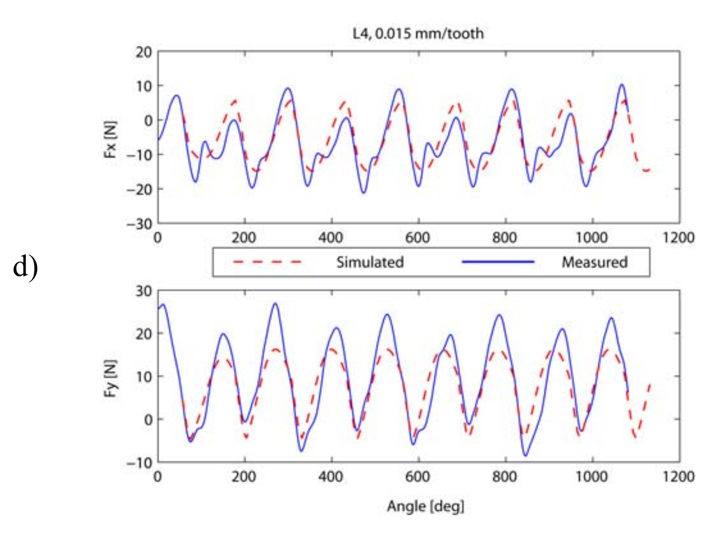

Figure 4-11: Experimental and simulation (MatLAB) results showing variations between different layers of cut under identical conditions (two-fluted flat end mill, full immersion at $n$ = 2500 rpm and $h$ = 0.015 mm/tooth: a) layer 1, b) layer 2, c) layer 3, and d) layer 4.

Even though it can be seen from Figure 4-10 and Figure 4-11 that the predicted cutting forces are in good agreement with the measured values, the experimental $F_x$ in Figure 4-10a and the experimental $F_x$ and $F_y$ in Figure 4-10c all display repeating features at the peak regions which are not predicted. However, these features do not exhibit a specific pattern under identical machining parameters between different layers of cut. Therefore, they are assumed to be due to particle effects, which may include randomly distributed microstructural defects and/or density gradients.

Additionally, the $F_y$ in both Figure 4-10c and Figure 4-11a reveal some discrepancies between the experimental and the simulated forces at the peak and valley regions. Yet again, the occurrences appear to be unsystematic. Foremost, run-out and poor alignment of the tool in chuck were speculated, implying that all cutting tests should exhibit similar outcomes. Nonetheless, this was not observed and the assumption was rejected. Another reason could be the existence of different forced vibration conditions from cut to cut, which was not considered in the simulation.

The machinability and the finish of a brittle material like CPP can be dramatically affected by the presence of defects within the material blank. These can be either internal, such as flaws generated during material preparation, or flaws that are introduced later during post processing such as machining. Some of the examples of these internal microstructural defects can be cracks formed as a result of sintering shrinkage or abnormal large grains [107]. However, it is difficult to predict these flaws because their occurrences and distribution are purely statistical. On the other hand, the deviation between the experimental and simulated forces could be a result of cracks and material deformation that occurred during machining, which would instigate microstructure discontinuity and cause strength reduction in CPP [103][107]. Hence, special precaution needs to be taken during machining to avoid chatter or excessive forced vibration by using rigid tools and fixtures and selecting stable cutting conditions [86]. During machining, the interaction at the tool-workpiece interface can initiate flaws in the ceramics as shown in Figure 4-12. Thus, it is important to understand this phenomenon. Material directly in the path of the tool is sheared to form the chip and is experiencing the maximum amount of stress and highest temperature rise. The sheared away chips are partially deformed and are along the rake face of the tool [86]. Lastly, the material adjacent to the cutting edge rubs the newly machined surface, which can lead to either crack or chipping [104].

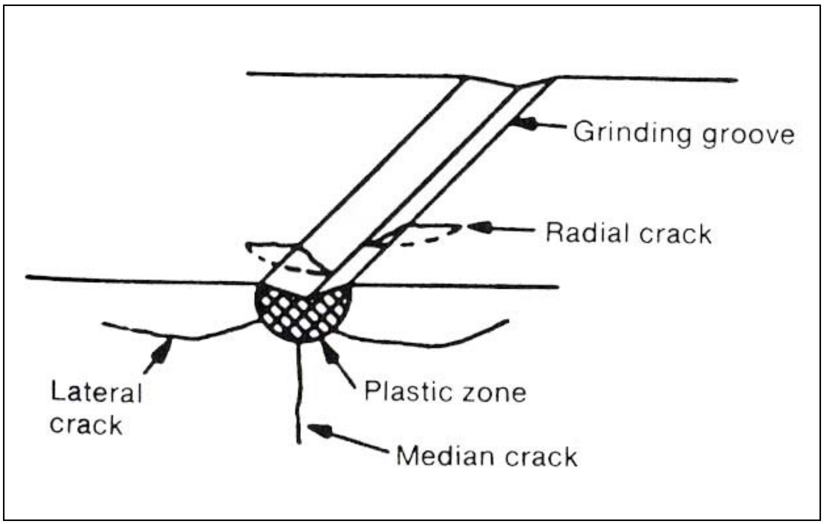

Figure 4-12: Schematic showing cracks and material deformation occurs during machining [104].

During machining, a notable amount of chipping was observed at the corner of the machined grooves. This can be a result of mechanically induced cracks caused by stress concentration. Lateral cracks are extended from the plastic zone, parallel to the surface, and usually form along the least resistant path, which is commonly the grain boundary [106]. They instigate chipping and result in deviation in the cutting forces.

A forced prediction model as developed here is intended for avoiding unfavourable machining conditions in which excessive force and vibration are generated that could damage the CPP material's microstructure.

### 4.4.5 Validation of Cutting Force Model

Using the identified cutting coefficients, cutting forces for different cutter geometries and machining condition can be predicted. For this purpose, the cutting forces for a ball nose-end mill [112], which is commonly used in surface machining, were simulated and compared to experiment results. Figure 4-13 shows a general geometry of the ball nose-end mill geometry and a picture of the actual used during the validation experiments. The experiments were conducted using a 2.381 mm (3/32") diameter, two-fluted tungsten carbide ball nose-end mill. The experimental setup follows the same procedure as described in Section 4.4.1. The results are shown in Figure 4-14.

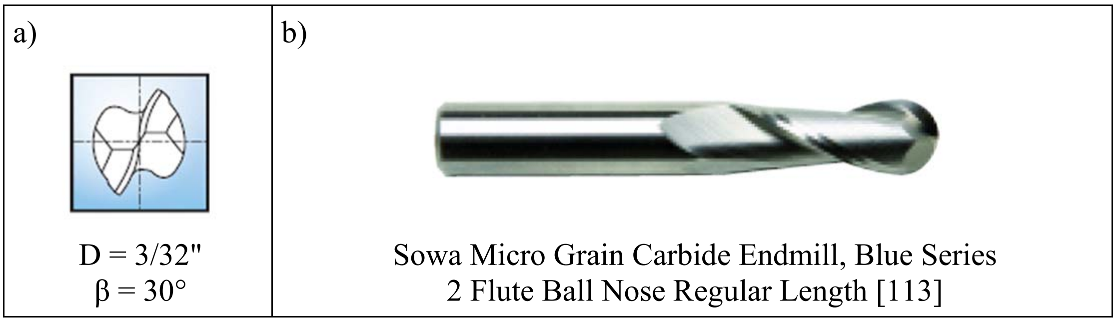

a) D = 3/32"
$\beta = 30°$

b) Sowa Micro Grain Carbide Endmill, Blue Series
2 Flute Ball Nose Regular Length [113]

Figure 4-13: Two-fluted ball nose-end mill used in validation of the CPP cutting force model: a) schematic and b) the actual cutter.

a)

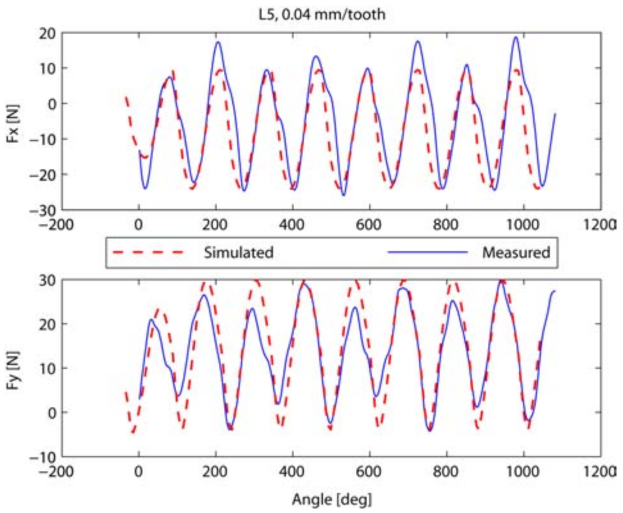
L5, 0.04 mm/tooth
Fx [N]
20
10
0
−10
−20
−30
−200
0
200
400
600
800
1000
1200
Simulated
Measured
Fy [N]
30
20
10
0
−10
Angle [deg]

b)

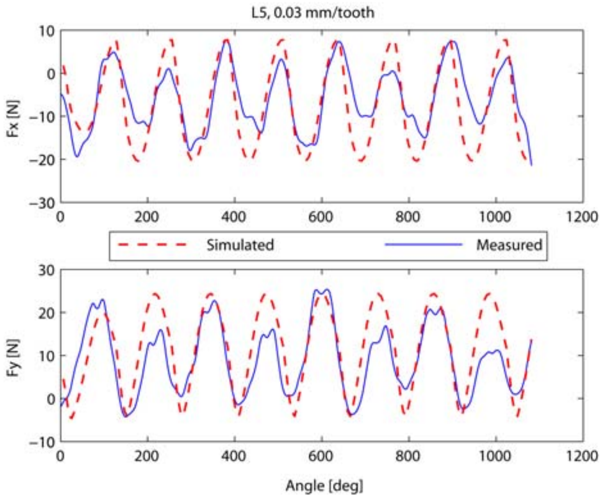
L5, 0.03 mm/tooth
Fx [N]
10
0
−10
−20
−30
0
200
400
600
800
1000
1200
Simulated
Measured
Fy [N]
30
20
10
0
−10
Angle [deg]

c)

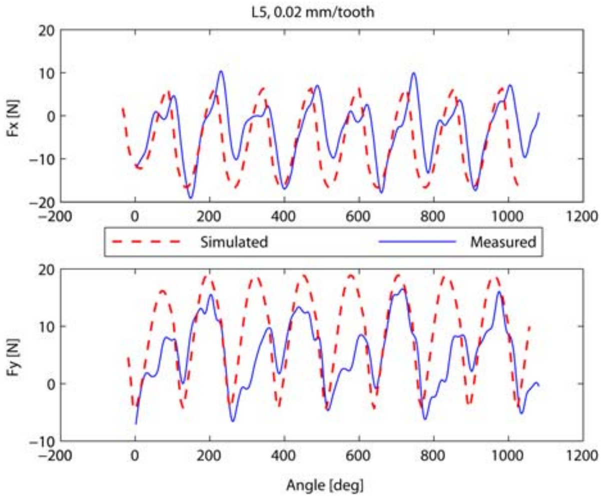
L5, 0.02 mm/tooth
Fx [N]
20
10
0
−10
−20
−200
0
200
400
600
800
1000
1200
Simulated
Measured
Fy [N]
20
10
0
−10
Angle [deg]

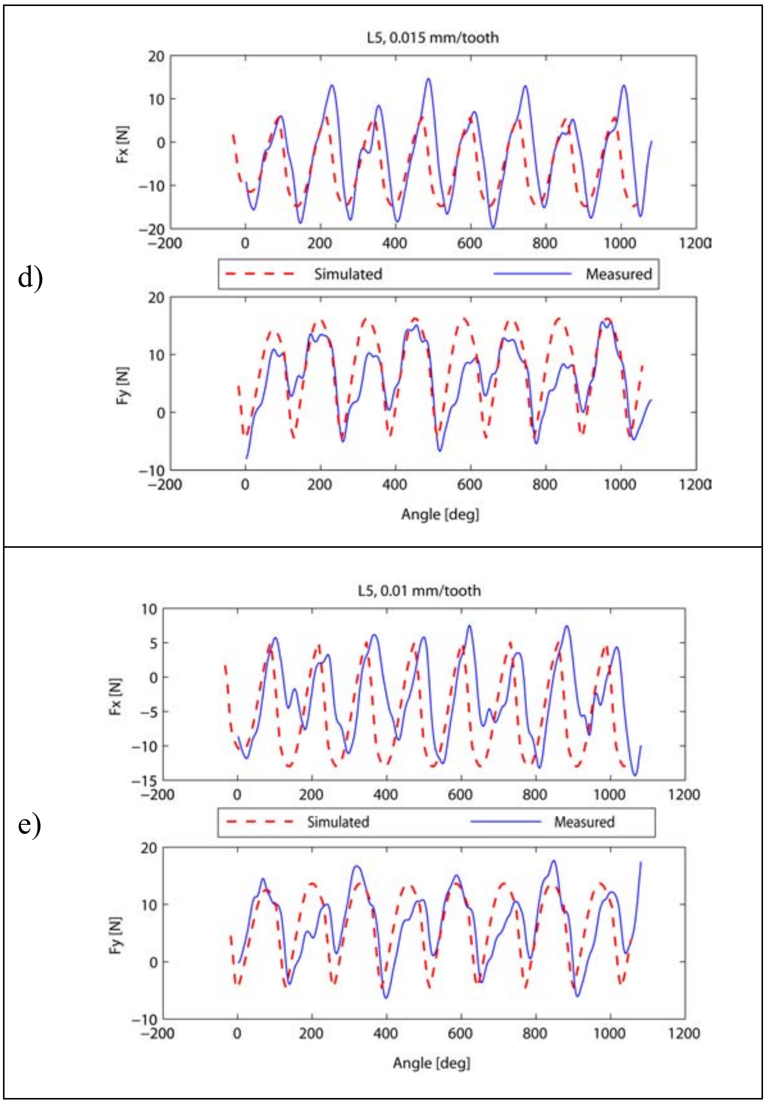

Figure 4-14: Experimental and simulation (CutPRO) results of a two-fluted ball nose-end mill, full immersion at $n = 2500$ rpm: a) feed rate 0.04 mm/tooth, b) feed rate 0.03 mm/tooth, c) feed rate 0.02 mm/tooth, d) feed rate 0.015 mm/tooth, and e) feed rate 0.01 mm/tooth.

The cutting forces for milling CPP using a ball nose-end mill were simulated using the identified cutting coefficients and compared with the experimental results. This validates the possibility of using the cutting coefficients to predict forces for different cutter geometries. As can be seen, the cutting force simulation usually exhibits good agreement in predicting the fundamental magnitude and shape of the actual forces. The variations are accounted to the effect of particle breakage due to microstructural defects or density gradients. In addition, the brittle fracture mechanism of CPP does not fully agree with the shear plane model used in the force prediction, and the deviation of the true cutter geometry from the ideal can also contribute to discrepancies.

The discrepancies and unevenness in the cutting forces from one tooth period to the next were a result of run-out. As verified by the run-out measurement, there is a difference of 2.5 μm (0.0001") between the two teeth and a total run-out of 7.5 μm (0.0003"). Even though the magnitude of the run-out appears to be minimal, when compare with the chip load used during machining (10 to 40 μm/tooth), it is in fact significant. The occurrence of run-out causes the chip thickness to vary between different flutes of the cutter. This subsequently affects the average and peak forces, and the instantaneous force profile as shown in Equations (4.4) and (4.6). Nonetheless, this effect depends on several factors: the cutting conditions, cutter geometry, as well as the degree and nature of the run-out. Overall, the cutting coefficients enable reasonably close prediction of the actual cutting forces, as verified by the experimental results.

Hence, a quantized cutting force model has been established for machining CPP for the first time and validated with ball-end milling experiments, which show reasonable consistency with the predictions. Such a force model can be utilized to determine cutting conditions which will prevent excessive tool deflection and machining vibration, and avoid damaging the part and machined surfaces.

### 4.4.6 CNC Machined Sample Characterization

Scanning electron microscopy images were taken to examine the machined surfaces obtained under different feeds and speeds. The procedures employed to clean the machined samples and prepare them for SEM imaging were similar to those described in Section 3.2.2.4. SEM images were captured at the locations as shown in Figure 4-15 for the surfaces machined using flat-end and ball nose-end mills.

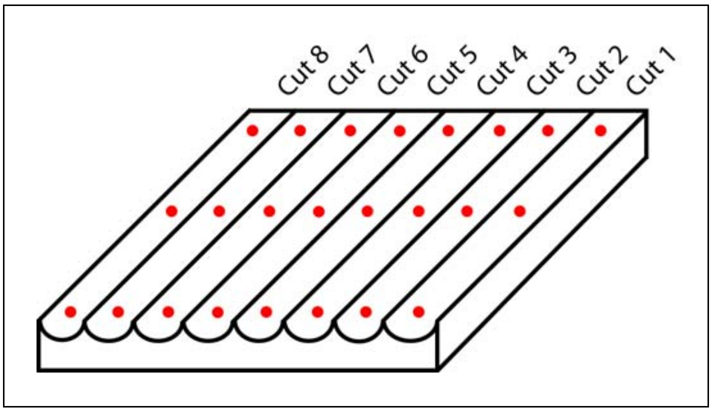

Figure 4-15: SEM scheme for machined surface using ball nose end mill.

A picture of the machined sample is shown in Figure 4-16. The microstructure of the machined surfaces was assessed by SEM images at three locations, i.e., entry, midpoint, and exit of the sample, for ball milling conditions. Circle a in Figure 4-16 is cross reference to the SEM image in Figure 4-17b, while the proceeding image for circle b is shown in Figure 4-18b. There is evidence of smearing and pores closing up as shown in Figure 4-17b and Figure 4-18 at fifty times the magnification. A SEM image of a sample prepared and sectioned using the standard protocol (as described in Section 3.2.2.4) is presented in Figure 4-19 at 100 times the magnification and was used as a controlled surface for comparison.

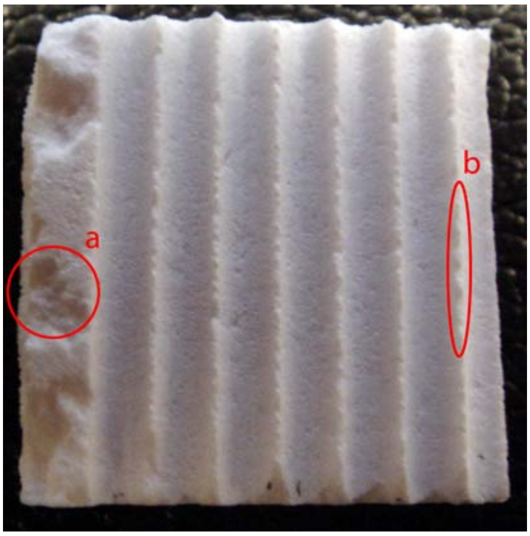

Figure 4-16: A picture of the machined sample. The circles indicate the occurrence of chipping during machining.

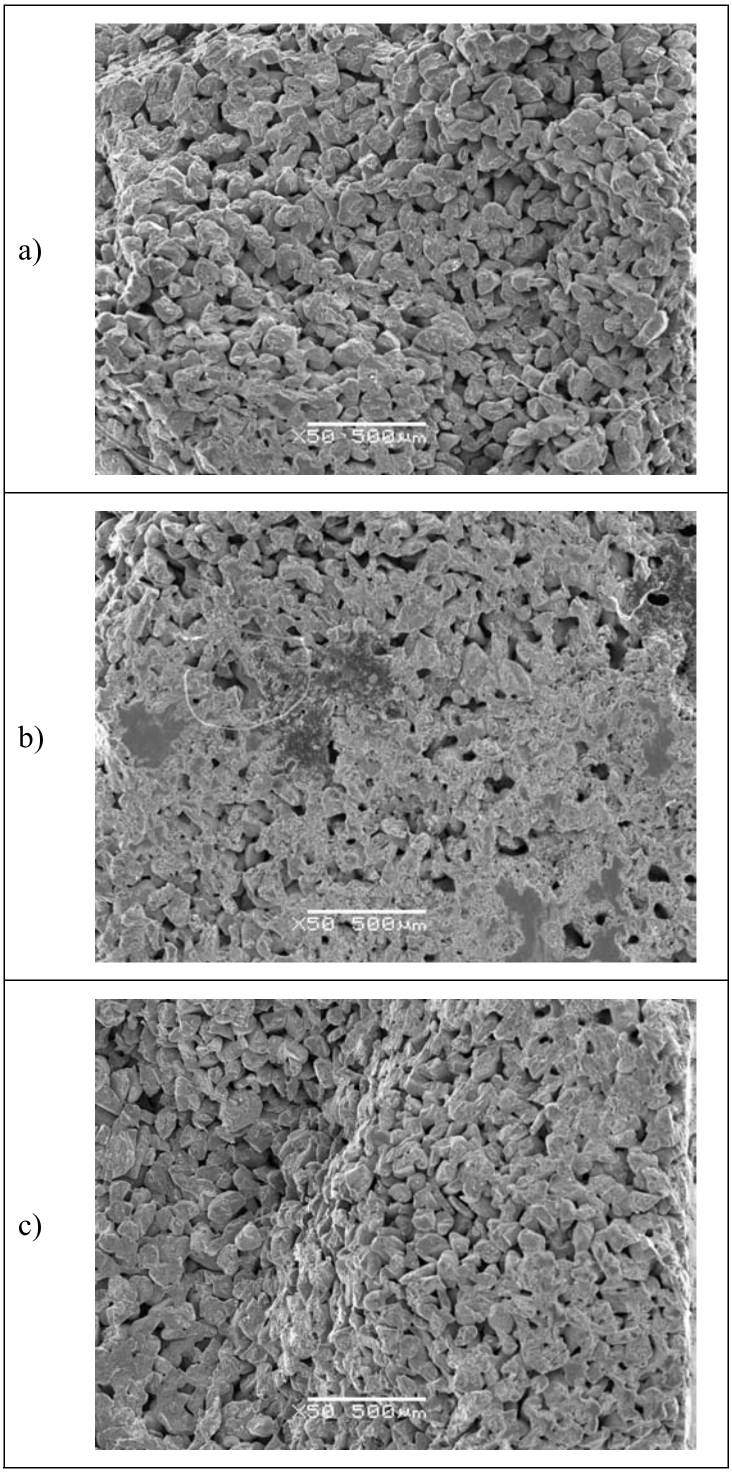

Figure 4-17: SEM of flat-end milled surface, full immersion with spindle speed of 2500 rpm and feed rate of 0.01 mm/tooth at: a) entry point, b) midpoint, and c) exit position.

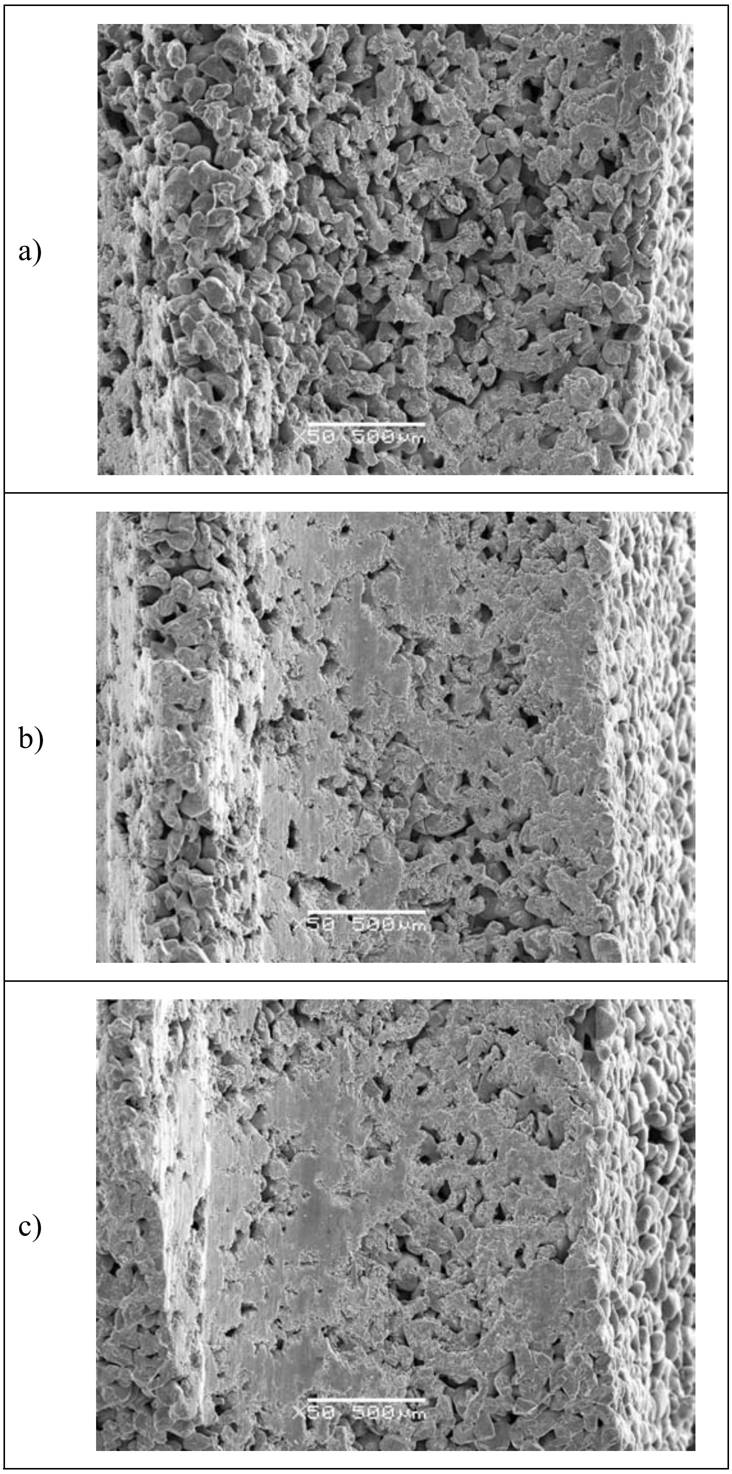

Figure 4-18: SEM of ball-end milled surface, full immersion with spindle speed of 2500 rpm and feed rate of 0.04 mm/tooth at: a) entry point, b) midpoint, and c) exit position.

As revealed above, at the center of the ball nose cutter, a smearing effect can be observed. In general, the surfaces produced by up-milling yield an improved finish with more pores remained open.

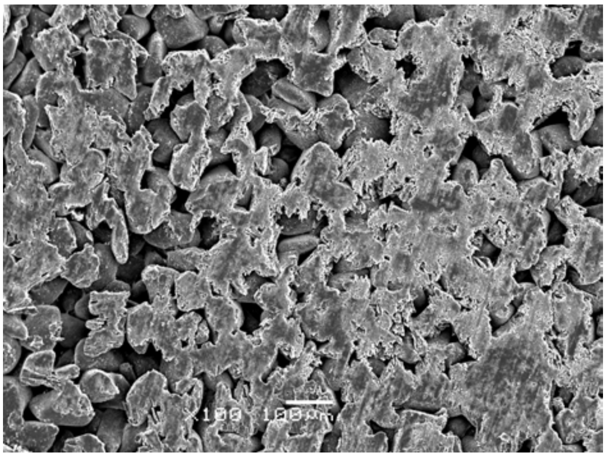

Figure 4-19: SEM image of a sample prepared using the standard protocol.

It appears that the flat end-milled surfaces demonstrated higher-quality and more open porosity when compared to the ball end-milled surfaces as shown in Figure 4-17 and Figure 4-18 respectively. From cross-examination of these results with the controlled surface (Figure 4-19), one can observe that the surface produced using the diamond wafering blade has a significant degree of smearing and close porosity. This surface was produced by the standard technique used to slice CPP rods into discs for chondrocytes culturing [13][44]. Even though the surfaces of these discs appeared to be partially clogged, cartilage tissues were able to be seeded and integrated at the cartilage-CPP interfaces in previous studies [5][18][49]. For that reason, even though some of the ball-milled surfaces have shown insufficient surface morphological properties after machining, they might not be completely deleterious and unacceptable. In addition, the most recent study conducted by another colleague at the Precision Controls Laboratory demonstrated that it is possible to avoid smearing and enhance pore opening by choosing the correct CNC machining conditions [114].

One process parameter that determines the quality of the surface finish of a part is the relationship between the direction of the tool rotation and the feed. This relationship defines two types of peripheral milling operations: up- and down-milling. Both operations essentially produce the same part but the dynamics and stability properties are quite different. During slotting, the cutting forces between the up- and down-milling will be the same simply because they are just a mirror image of each other. However, the forces for up- and down-milling are different in partially immersed cuts. Ideally, to generate a better surface finish for a brittle material like CPP, up-milling is normally desired where shock loading is reduced [86] and particles are "pulled off" from the surface, thus leading a porous finish behind. This was verified in further studies conducted [114].

### 4.4.7 Conclusions

The following conclusions can be drawn based on the studies conducted in this chapter:

1. The findings of this study have shown that it is feasible to machine CPP. By careful selection of the machining conditions, CPP can be machined to yield complex half-tibia implants as designed by Dudi and Papini [97].

2. The cutting coefficients for 75% dense CPP were identified by conducting full immersion slotting tests at a constant depth of cut and varying feed rates using a flat-end mill. The cutting forces were modeled using the identified cutting coefficients in MatLAB.

    i) The shear and the edge components of the cutting coefficients in the tangential and radial directions were determined to be 472.101 N/mm$^2$, 5.1387 N/mm, 153.5476 N/mm$^2$, and 6.0662 N/mm, respectively.
    ii) In general, the experimental forces exhibit good agreement with the predicted forces in magnitude and shape.

3. To validate the identified cutting coefficients, a ball nose-end mill was used. The results indicate that cutting force simulation usually displays good prediction

accuracy. Nonetheless, variations at the peak and valley regions indicate discrepancies including the brittle nature of CPP which does not agree with the shear plane model in use, the material properties of CPP, and the microstructural defects. Tool run-out is also a contributor.

# Chapter 5

# Conclusions and Future Work

This thesis has presented two methods to fabricate complex, anatomically-shaped biodegradable calcium polyphosphate (CPP) implants for the potential use as a load-bearing component for repairing of osteochondral focal defects in clinically relevant bone-engineering applications. The proposed techniques investigated were: rapid prototyping (RP) as the novel material additive process and computer numerically controlled (CNC) machining as the conventional material subtractive process.

In rapid prototyping, a powder-based technology called the three-dimensional printing (3DP) was exercised in two approaches. In the first approach, 3DP was used to fabricate negative molds based on the substrate design and pre-shape the substrates using a polymeric binder and CPP powder. This alternative technique is termed indirect-3DP. It was ascertained that the substrates produced this way yielded densities (<75 μm: 66.28 ± 11.62% and 106-150 μm: 65.87 ± 6.12%) equivalent to what are being used currently in animal studies. The findings suggest that the use of different powder sizes and sintering temperatures can result in considerable differences in densification. In general, finer particle size and higher sintering temperature lead to denser CPP structures. The degree of shrinkage is most significant in the z-direction regardless of the staring powder or the fabrication method used. Additionally, the sintered structures exhibit homogeneously distributed and three-dimensional interconnected porosity.

In the second approach, the 3DP was used directly in fabricating the substrates by successively adding the CPP powder in a layer-by-layer fashion. The aqueous-based binder used eliminates the problem linked to the use of an organic solvent. The results show that the samples produced exhibit more significant shrinkages with up to 22.70 ± 8.87% in the z-direction when they were sintered at a higher temperature of 592°C. The direct impact of sintering temperature can be confirmed by the samples sintered at 585°C, which yield an average shrinkage of 14.00 ± 1.61% in the z-direction. These samples display three-dimensional interconnected porosities and the neck and grain boundary formations indicate good connections through sintering were achieved. From the processing point of view, CPP powder demonstrates good flowability and spreadability if it is sieved and screened properly. CPP also exhibits good interaction with different kinds of binders provided that the amount of binder applied is adequate. Nonetheless, results support the use of the aqueous-based binder at the current time despite the fact that water might induce hydrolysis degradation of CPP.

In terms of CNC machining, the feasibility of machining CPP has been studied for the first time and proven successful. A mechanistic model was developed based on conducting full immersion slotting experiments at a range of feed rates and measuring cutting forces during the tests. By linear curve fitting the average measured forces, the edge and cutting force coefficients were determined. To verify the accuracy of these coefficients, the cutting forces for a ball nose-end mill were predicted and verified with experimental data. The findings suggest that the accuracy is fairly reasonable in yielding fundamental force magnitudes and shapes. However, due to the brittle nature of CPP, particle effects and microstructural defects also result in unpredictable variations. The machined surface demonstrated open porosity when milled using a flat-end mill. Even though the ball-milled surfaces showed partial smearing and closed porosity, results from the previous studies have demonstrated that they are not completely unacceptable for cartilage growth.

The main differences between the direct-3DP and CNC machining were discovered in the manufacturing time, dimensional accuracy, and the wastage of material. Unlike 3DP, the planning of the CNC machining operation is more intricate. However, the process can be streamlined for mass production or producing custom implants with similar anatomical features but different dimensions. The 3DP technique also allows multiple parts to be fabricated in one step, whereas in CNC machining, only one part can be produced at a time. In addition, 3DP is capable of producing complex parts with conformal passages and allows varying density and porosity across the part.

A major disadvantage of 3DP is the dimensional inaccuracy as a result of anisotropic sintering shrinkage. Presently, the amount of shrinkage can be corrected by the average shrinkage determined; nonetheless, more experimental data should be conducted to yield more statistically-confident correction factors. In terms of CNC machining, the achievable accuracy is high and the as-machined part does not necessitate any further processing, this assures the material properties in its condition. However, the drawback is that the amount of stress exerted on the CPP blank can generate or induce unwanted CPP breaking and chipping. Hence, special attention is required during machining to select proper feeds and speeds for the tool to avoid excessive force loading and vibration, as well as to generate adequate surface finish.

A significant difference can also be perceived in the amount of material wastage involved between the two techniques. Due to the fact that 3DP engages in an additive process, the unbound powder can be recycled and reused. Conversely, during the subtractive machining process, the material removed by the cutter is discarded; thus the production yield is considerably low.

The followings are recommendations for future work based on the results obtained from the present study:

1. To optimize the process parameters of the developed direct-3DP technique. Some process parameters include binder and solvent combination, level of binder to solvent ratio, and powder mesh size.

2. To attain a better dimensional accuracy of the fabricated 3DP parts, investigation should be conducted to determine compensation factors similar to the process and methodology employed in studying the accuracy of the default plaster material (Section 3.4).

3. Mechanical properties should be assessed to determine the bending and compressive strength of the sintered samples produced using the 3DP methods.

4. Although precautions were taken to avoid contamination during the 3DP studies, an investigation into the effects of potential contaminants due to processing, especially in the indirect method, is required for more consistency in the resulting sintering properties.

5. Findings suggest that the use of the aqueous-based binder appears to bond the CPP powder adequately. Further study should be conducted to ensure there is no sign of hydrolysis degradation and ultimately it would be best to avoid this problem by using an ethanol-based binder.

6. Dynamic vibration should be modelled to account for the disturbance during machining. The structural vibrations of the tool attached to the spindle can be determined using hammer tests, finite element modelling, and receptance coupling.

7. Tool wear, particularly flank wear, should be examined regularly during these slotting experiments to cross-examine whether the prediction inaccuracy is a result of tool wear.

# References

[1] Chang, C.H., Kuo, T.F., Lin, C.C., Chou, C.H., Chen, K.H., Lin, F.H., and Liu H.C., (2006), "Tissue engineering-based cartilage repair with allogenous chondrocytes and gelatin-chondroitin-hyaluronan tri-copolymer scaffold: a porcine model assessed at 18, 24, and 36 weeks", *Biomater.*, Vol. 27, pp. 1876-1888.

[2] Redman, S.N., Oldfield, S.F., and Archer, C.W., (2005), "Current strategies for articular cartilage repair", *Eur. Cell. Mater.*, Vol. 9, pp. 23-32.

[3] Söderman, P., Malchau, H., Herberts, P., Zügner, R., Regnér, H., and Garellick, G., (2001), "Outcome after total hip arthroplasty. Part II. Disease-specific follow-up and the Swedish national total hip arthroplasty register", *Acta. Orthop. Scand.*, Vol. 72 No. 2, pp. 113-119.

[4] Waldman, S.D., Spiteri, C.G., Grynpas, M.D., Pilliar, R.M., Hong, J., and Kandel, R.A., (2003), "Effect of biomechanical conditioning on cartilaginous tissue formation *in vitro*", *J. Bone Joint Surg. Am.*, Vol. 85-A Suppl. 2, pp. 101-105.

[5] Kandel, R.A., Grynpas, M., Pilliar, R., Lee, J., Wang, J., Waldman, S., Zalzal, P., and Hurtig, M., (2006), "Repair of osteochondral defects with biphasic cartilage-calcium polyphosphate constructs in a sheep model", *Biomater.*, Vol. 27, pp. 4120-4131.

[6] Tanaka, T., Komaki, H., Chazono, M., and Fujii, K., (2005), "Use of a biphasic graft constructed with chondrocytes overlying a β-tricalcium phosphate block in the treatment of rabbit osteochondral defects", *Tissue Eng.*, Vol. 11 No. 1/2, pp.331-339.

[7] Schaefer, D., Martin, I., Jundt, G., Seidel, J., Heberer, M., Grodzinsky, A., Bergin, I., Vunjak-Novakovic, G., and Freed, L.E., (2002), "Tissue-engineered composites for the repair of large osteochondral defects", *Arthritis Rheum.*, Vol. 46 No. 9, pp. 2524-2534.

[8] Gao, J., Dennis, J.E., Solchaga, L.A., Goldberg, V.M., and Caplan, A.I., (2002), "Repair of osteochondral defect with tissue-engineered two-phase composite material of injectable calcium phosphate and hyaluronan sponge", *Tissue Eng.*, Vol. 8 No. 5, pp. 827-837.

[9] Vaccaro, A.R., (2002), "The role of the osteoconductive scaffold in synthetic bone graft", *Orthopedics*, Vol. 25 No. 5 Suppl., pp. 571-578.

[10] Moore, W.R., Graves, S.E., and Bain, G.I., (2001), “Synthetic bone graft substitutes”, *ANZ J. Surg.*, Vol 71, pp. 354-361.

[11] Begley, C.T., Doherty, M.J., Mollan, R.A.B., and Wilson, D.J., (1995), “Comparative study of the osteoinductive properties of bioceramic, coral and processed bone graft substitutes”, *Biomater.*, Vol. 16 No. 15, pp. 1181-1185.

[12] Lewandrowski, K.-U., Gresser, J.D., Wise, D.L., and Trantolo, D.J., (2000), “Bioresorbable bone graft substitutes of different osteoconductivities: a histologic evaluation of osteointegration of poly(propylene glycol-co-fumaric acid)-based cement implants in rats”, *Biomater.*, Vol. 21 No. 8, pp. 757-764.

[13] Pilliar, R.M., Filiaggi, M.J., Wells, J.D., Grynpas, M.D., and Kandel R.A., (2001), “Porous calcium polyphosphate scaffolds for bone substitute applications - *in vitro* characterization”, *Biomater.*, Vol. 22 No. 9, pp. 963-972.

[14] Pilliar, R.M., (1987), “Porous-surfaced metallic implants for orthopaedic applications”, *J. Biomed. Mater. Res.*, Vol. 21, pp. 1-33.

[15] Bartel, D.L., Davy, D.T., and Keaveny, T.M., (2006), *Orthopaedic Biomechanics: Mechanics and Design in Musculoskeletal System*. Pearson Prentice Hall, New Jersey, pp. 95.

[16] Baksh, D. and Davies, J.E., (1998), “Three-dimensional matrices of calcium polyphosphates support bone growth *in vitro* and *in vivo*”, *J. Mater. Sci.*, Vol. 9, pp. 743-748.

[17] Qiu, K., Wan C.X., and Zhao, C.S., (2006), “Fabrication and characterization of porous calcium polyphosphates scaffolds”, *J. Mater. Sci.*, Vol. 41, pp. 2429-2434.

[18] Waldman, S.D., Grynpas, M.D., Pilliar, R.M., and Kandel, R.A., (2002), “Characterization of cartilaginous tissue formed on calcium polyphosphate substrates *in vitro*”, *J. Biomed. Mater. Res.*, Vol. 62 No. 3, pp. 323-330.

[19] Ciolfi, V.J.D., Pilliar, R., McCulloch, C., Wang, S.X., Grynpas, M.D., and Kandel, R.A., (2003), “Chondrocyte interactions with porous titanium alloy and calcium polyphosphate substrates”, *Biomater.*, Vol. 24, pp. 4761-4770.

[20] Hung, C.T., Lima, E.G., Mauck, R.L., Taki, E., LeRoux, M.A., Lu, H.H., Stark, R.G., Guo, X.E., and Ateshian, G.A., (2003), “Anatomically shaped

osteochondral constructs for articular cartilage repair", *J. Biomechanics*, Vol. 36, pp. 1853-1864.

[21] Chen, F., Mao, T., Tao, K., Chen, S., Ding, G., and Gu, X., (2002), "Bone graft in the shape of human mandibular condyle reconstruction via seeding marrow-derived osteoblasts into porous coral in a nude mice model", *J. Oral Maxillofac. Surg.*, Vol. 60, pp. 1155-1159.

[22] Abukawa, H., Terai, H., Hannouche, D., Vacanti, J.P., Kaban, L.B., and Troulis, M.J., (2003), "Formation of a mandibular condyle *in vitro* by tissue engineering", *J. Oral Maxillofac. Surg.*, Vol. 61, pp. 94-100.

[23] Alhadlaq, A. and Mao, J.J., (2003), "Tissue-engineered neogenesis of human-shaped mandibular condyle from rat mesenchymal stem cells", *J. Dent. Res.*, Vol. 82 No. 12, pp. 951-956.

[24] Schek, R.M., Taboas, J.M., Hollister, S.J., and Krebsbach, P.H., (2005), "Tissue engineering osteochondral implants for temporomandibular joint repair", *Orthod. Craniofacial Res.*, Vol. 8, pp. 313-319.

[25] Hamilton, D.J., Séguin, C.A., Wang, J., Pilliar, R.M., and Kandel R.A., (2006), "Formation of nucleus pulposus-cartilage endplate construct *in vitro*", *Biomater.*, Vol. 27 No. 3, pp. 397-405.

[26] Ahmad, C.S, Cohen, Z.A., Levine, W.N., Ateshian, G.A., and Mow, V.C., (2001), "Biomechanical and topographic considerations for autologous osteochondral in the knee", *Am. J. Sports Med.*, Vol. 29 No. 2, pp. 201-206.

[27] Simmons, C.A., Meguid, S.A., and Pilliar, R.M., (2001), "Differences in osseointegration rate due to implant surface geometry can be explained by local tissue strains", *J. Orthop. Res.*, Vol. 19 No. 2, pp. 187-194.

[28] Carter, D.R., Beaupre, G.S., Giori, N.J., and Helms, J.A., (1998), "Mechanobiology of skeletal regeneration", *Clin. Orthop.*, Vol. 355 Suppl., pp. 41-55.

[29] Kumta, P.N., (2006), Ceramic Biomaterials. *An Introduction to Biomaterials*. Edited by Guelcher, S.A. and Hollinger, J.O., CRC Press, Boca Raton, pp. 311-339.

[30] Hench, L.L. and Best, S., (2004), Ceramics, Glass, and Glass Ceramics. *Biomaterials Science: An Introduction to Materials in Medicine*. Edited by Ratner, B.D., Hoffman, A.S., Schoen, F.J., and Lemons, J.E., Elsevier Academic Press, London, pp 153-170.

[31] Roy, T.D., Simon, J.L., Ricci, J.L., Rekow, E.D., Thompson, V.P., and Parsons, J.R., (2003), “Performance of hydroxyapatite bone repair scaffolds created via three-dimensional fabrication techniques”, *J. Biomed. Mater. Res.*, Vol. 67A, pp. 1228-1237.

[32] Erbe, E.M., Marx, J.G., Clineff, T.D., and Bellincampi, L.D., (2001), “Potential of an ultraporous β-tricalcium phosphate synthetic cancellous bone void filler and bone marrow aspirate composite graft”, *Eur. Spine J.*, Vol 10 Suppl., pp. 141-146.

[33] Eggli, P.S., Moller, W., and Schenk, R.K., (1988), “Porous hydroxyapatite and tricalcium phosphate cylinders with two different pore size ranges implanted in the cancellous bone of rabbits: A comparative histomorphometric and histologic study of bony ingrowth and implant substitution”, *Clin. Orthop. Res.*, Vol. 232, pp. 127-138.

[34] Kitsugi, T., Yamamuro, T., Nakamura, T., Kotani, S., Kokubo, T., and Takeuchi, H., (1993), “Four calcium phosphate ceramics as bone substitutes for non-weight-bearing” *Biomater.*, Vol. 14 No. 3, pp. 216-224.

[35] Porter, N.L., Pilliar, R.M., and Grynpas, M.D., (2001), “Fabrication of porous calcium polyphosphate implants by solid freeform fabrication: A study of processing parameters and *in vitro* degradation characteristic”, *J. Biomed. Mater. Res.*, Vol. 56, pp. 504-515.

[36] de Groot, K., Klein, C.P.A.T., Wolke, J.G.C., and de Blieck-Hogervorst, J.M.A., (1990), Chemistry of Calcium Phosphate Bioceramics. *CRC Handbook of Bioactive Ceramics: Volume II Calcium Phosphate and Hydroxyapatite Ceramics*. Edited by Yamamuro, T., Hench, L.L., and Wilson, J., CRC Press, Boca Raton.

[37] LeGeros, R.Z., (1993), “Biodegradation and bioresorption of calcium phosphate ceramics”, *Clin. Mater.*, Vol. 14, pp. 65-88.

[38] van Noort, R., (2002), Dental Ceramics. *Introduction to Dental Materials*. Mosby, Toronto, pp. 231-246.

[39] Nasr, H.F., Aichelmann-Reidy, M.E., and Yukna, R.A., (2000), “Bone and bone substitutes”, *Periodontology*, Vol. 19, pp. 74-86.

[40] Tas, C.A., Korkusuz, F., Timucin, M., and Akkas, N., (1997), “An investigation of the chemical synthesis and high-temperature sintering behaviour of calcium hydroxyapatite (HA) and tricalcium phosphate (TCP) bioceramics”, *J. Mater. Sci.*, Vol. 8, pp. 91-96.

[41] Tisdel, C.L., Goldberg, V.M., Parr, J.A., Bensusan, J.S., Staikoff, L.S., and Stevenson, S., (1994), "The influence of a hydroxyapatite and tricalcium-phosphate coating on bone growth into titanium fiber-metal implants", *J. Bone & Joint Surg. Am.*, Vol. 76, pp. 159-171.

[42] Lacout, J.L, (1992), Calcium phosphate as bioceramics. *Biomaterials: Hard Tissue Repair and Replacement*. Edited by Muster, D., Elsevier Science Publishers, Netherlands.

[43] Klein, C.P.A.T., Driessen, A.A., de Groot, K., and van den Hooff, A., (1983), "Biodegradation behavior of various calcium phosphate materials in bone tissue", *J. Biomed. Mater. Res.*, Vol. 17 No. 5, pp. 769-784.

[44] Hamilton, D.J., Séguin, C.A., Wang, J., Pilliar, R.M., and Kandel R.A., (2006), "Formation of nucleus pulposus-cartilage endplate construct *in vitro*", *Biomater.*, Vol. 27 No. 3, pp. 397-405.

[45] Brown, E.H., Lehr, J.R., Smith, J.P., Brown, W.E., and Frazier, A.W., (1957), "Crystalline intermediates in the hydrolytic degradation of calcium polymetaphosphate", *J. Phys. Chem.*, Vol. 61, pp. 1669-1670.

[46] Huffman, E.O. and Fleming, J.D., (1960), "Calcium polyphosphate - rate and mechanism of its hydrolytic degradation", *J. Phys. Chem.*, Vol. 64, pp. 240-244.

[47] Averbuch-Pouchot, M.T. and Durif, A., (1996), Long-Chain Polyphosphates. *Topics in Phosphate Chemistry*. World Scientific Publishing Co., Singapore, pp196-220.

[48] Griffith, E.J., (1995), General Phosphate Chemistry. *Phosphate Fibers*. Plenum Press, London, pp 81-85.

[49] Grynpas, M.D., Pilliar, R.M., Kandel, R.A., Renlund, R., and Filiaggi, M., (2003), "Porous calcium polyphosphate scaffolds for bone substitute applications - *in vivo* studies", *Biomater.*, Vol. 23 No. 9, pp. 2063-2070.

[50] Waldman, S.D., Spiteri, C.G., Grynpas, M.D., Pilliar, R.M., and Kandel, R.A., (2004), "Long-term intermittent compressive stimulation improves the composition and mechanical properties of tissue-engineered cartilage", *Tissue Eng.*, Vol. 10 No. 9/10, pp. 1323-1331.

[51] Waldman, S.D., Spiteri, C.G., Grynpas, M.D., Pilliar, R.M., and Kandel, R.A., (2003), "Long-term intermittent shear deformation improves the quality of cartilaginous tissue formed *in vitro*", *J. Orthopaedic Res.*, Vol. 21, pp. 590-596.

[52] Dimitrov, D., van Wijck, W., Schreve, K., and de Beer, N., (2006), "Investigating the achievable accuracy of three dimensional printing", *Rapid Prototyping J.*, Vol. 12, pp. 42-52.

[53] Yan, X. and Gu, P., (1996), "Survey: a review of rapid prototyping technologies and systems", *Computer-Aided Design*. Vol. 28 No. 4, pp. 307-318.

[54] Beaman, J.J., Atwood, C., Bergman, T.L., Bourell, D., Hollister, S., and Rosen, D., (2004), "WTEC panel report on additive subtractive manufacturing research and development in Europe", Baltimore, MD: World Technology Evaluation Center, Inc. Available on http://www.wtec.org.

[55] Lohfeld, S., Barron, V., and McHugh, P.E., (2005), "Biomodels of Bone: a review", *Annals Biomed. Eng.*, Vol. 33 No. 10, pp. 1295-1311.

[56] Webb, P.A., (2000), "A review of rapid prototyping (RP) techniques in the medical and biomedical sector", *J. Med. Eng. Tech.*, Vol. 24 No. 4, pp. 149-153.

[57] Hutmacher, D.W., Sittinger, M., Risbud, M.V., (2004), "Scaffold-based tissue engineering: rationale for computer-aided design and solid free-form fabrication systems", *TRENDS in Biotechnology*, Vol. 22 No. 7, pp. 354-362.

[58] Hull, C.W., (1986) Apparatus for production of three-dimensional objects by Stereolithography, US Patent 4,575,330.

[59] Jacobs, P.F., (1992), Introduction to Rapid Prototyping and Manufacturing. *Rapid Prototyping & Manufacturing: Fundamentals of Stereolithography*. Society of Manufacturing Engineers, New York, pp. 1-25.

[60] Cooke, M.N., Fisher, J.P., Dean, D., Rimnac, C., and Mikos, A.G., (2002), "Use of stereolithography to manufacture critical-sized 3D biodegradable scaffolds for bone ingrowth", *J. Biomed. Mater. Res.*, Vol. 64, pp. 65-69.

[61] Shin, H., Ruhe, P.Q., Mikos, A.G., and Jansen, J.A., (2003), "*In vivo* bone and soft tissue response to injectable, biodegradable oligo(poly(ethylene glycol) fumarate) hydrogels", *Biomater.*, Vol. 24, pp. 3201–3211.

[62] Matsuda, T. and Mizutani, M., (2004), "Liquid acrylate-endcapped biodegradable poly(ε-caprolactone-co-trimethylene carbonate). II. computer-aided stereolithographic microarchitectural surface photoconstructs", *J. Biomed. Mater. Res.*, Vol. 62, pp. 395-403.

[63] Pham, D.T. and Dimov, S.S., (2001), *Rapid Manufacturing - the technologies & applications of rapid prototyping and rapid tooling*. Springers-Verlag, London.

[64] Steen, W. M., (2003), *Laser Material Processing*. Springer-Verlag, London.

[65] Vail, N.K., Swain, L.D., Fox, W.C., Aufdlemorte, T.B., Lee, G., and Barlow, J.W., (1999), "Materials for biomedical applications", *Materials & Design*, Vol. 20, pp.123-132.

[66] Barlow, J.W., Lee, G.H., Snyder, T.M., Vail, N.K., Swain, L.D., Fox, W.C., and Aufdlemorte, T.B., (2000), "Preparation of calcium phosphate implants", *Rapid Prototyping & Manufacturing 2000*; Rosemont, IL, USA, Apr. 10-13.

[67] Tan, K.H., Chua, C.K., Leong, K.F., Cheah, C.M., Cheang, P., Abu Bakar, M.S., and Cha, S.W., (2003) "Scaffolds development using selective laser sintering of polyetheretherketon-hydroxyapatite biocomposite blends", *Biomater.*, Vol. 24, pp. 3115-3123.

[68] Williams, J.M., Adewunmi, A., Schek, R.M., Flanagan, C.L., Krebsbach, P.H., Feinberg, S.E., Hollister, S.J., and Das, S., (2005), "Bone tissue engineering using polycaprolactone scaffolds fabricated via selective laser sintering", *Biomater.*, Vol. 26, pp. 4817-4827.

[69] Chua, C.K., Leong, K.F., Tan, K.H., Wiria, F.E., and Cheah, C.M., (2004), "Development of tissue scaffolds using selective laser sintering of polyvinyl alcohol/hydroxyapatite biocomposite for craniofacial and joint defects", *J. Mater. Sci.*, Vol. 15, pp. 1113-1121.

[70] Rimell, J.T. and Marquis, P.M., (2000), "Selective laser sintering of ultra high molecular weight polyethylene for clinical applications", *J. Biomed. Mater. Res.*, Vol. 53, pp. 414-420.

[71] Curodeau, A., Sachs, E., and Caldarise, S., (2000), "Design and fabrication of cast orthopedic implants with freeform surface textures from 3-D printed ceramic shell", *J. Biomed. Mater. Res.*, Vol. 53, pp. 525-535.

[72] Upcraft, S. and Fletcher, R., (2003), "The rapid prototyping technologies", *Assembly Automation*, Vol. 23, pp. 318-330.

[73] Venuvinod, P.K. and Ma, W., (2004), *Rapid Prototyping: Laser-Based and Other Technologies*. Kluwer Academic Publishers, Boston.

[74] Carrion, A., (1997), "Technology forecast on ink-jet head technology applications in rapid prototyping", *Rapid Prototyping J.*, Vol. 3 No. 3, pp. 99-115.

[75] Pfister, A., Walz, U., Laib, A., and Mulhaupt, R., (2005), "Polymer ionomers for rapid prototyping and rapid manufacturing by means of 3D printing", *Macromol. Mater. Eng.*, Vol. 290, pp. 99-113.

[76] Wohlers, T.T., (2005), *Wohlers report 2005 rapid prototyping, tooling, and manufacturing: state of the industry*. Annual Worldwise Progress Report, Wohlers Associates Inc., Fort Collins.

[77] Dimitrov, D., Schreve, K., and de Beer, N., (2006), "Advances in three dimensional printing - state of the art and future perspectives", *Rapid Prototyping J.*, Vol. 12, pp. 136-147.

[78] Irsen, S.H., Leukers, B., Hockling, C., Tille, C., and Seitz, H., (2006), "Bioceramic granulates for use in 3D printing: process engineering aspects", *Mat.-wiss. U. Werkstofftech.*, Vol. 37 No. 6, pp. 533-537.

[79] Seitz, H., Rieder, W., Irsen, S., Leukers, B, and Tille, C., (2005), "Three-dimensional printing of porous ceramic scaffolds for bone tissue engineering", *J. Biomed. Mater. Res.*, Vol. 74, pp. 782-788.

[80] Sherwood, J.K., Riley, S.L., Palazzolo, R., Brown, S.C., Monkhouse, D.C., Coates, M., Griffith, L.G., Landeen, L.K., and Ratcliffe, A., (2002), "A three-dimensional osteochondral composite scaffold for articular cartilage repair", *Biomater.*, Vol. 23, pp. 4739-4751.

[81] Dimitrov, D. and Schreve K., (2002), "Raid prototyping of a differential housing using 3D printing technology", *Proceeding of the International Conference on Manufacturing Automation*, 10-12 December, Hong Kong, pp. 483-490.

[82] Lee, S.-J.J., Sachs, E., and Cima, M., (1995) "Layer position accuracy in powder-based rapid prototyping", *Rapid Prototyping J.*, Vol. 1, pp. 24-37.

[83] Wilson, C.E., de Bruijn, J.D., van Blitterswijk, C.A., Verbout, A.J., and Dhert, W.J.A., (2003), "Design and fabrication of standardized hydroxyapatite scaffolds with a defined macro-architecture by rapid prototyping for bone-tissue-engineering research", *J. Biomed. Mater. Res.*, Vol. 68 No. 1, pp. 123-132.

[84] Taboas, J.M., Maddox, R.D., Krebsbach, P.H., and Hollister, S.J., (2003), "Indirect solid free form fabrication of local and global porous,

biomimetic and composite 3D polymer-ceramic scaffolds", *Biomater.*, Vol. 24 No. 1, pp. 181-194.

[85] Engin, S., Altintas, Y., and Amara, F.B., (2000), "Mechanics of routing medium density fiberboard", *Forest Products J.*, Vol. 50 No. 9, pp. 65-69.

[86] Altıntas, Y., (2000). *Manufacturing Automation: Principles of Metal Cutting and Machine Tool Control. Cambridge University Press*. ISBN 0521659736.

[87] Budak, E., Altıntas, Y., and Armarego, E.J.A., (1996), "Prediction of milling force coefficients from orthogonal cutting data", *J. Manuf. Sci. Eng.*, Vol. 118, pp. 216-224.

[88] Kline, W.A., DeVor, R.E., and Lindberg, J.R., (1982), "The prediction of cutting forces in end milling with application to cornering cuts", *Intl. J. Mach. Tool Des. Res.*, Vol. 1, pp. 7-22.

[89] Kline, W.A. and DeVor, R.E., (1983), "The effect of runout on cutting geometry and forces in end milling", *Intl. J. Mach. Tool Des. Res.*, Vol. 23 No. 2/3, pp. 123-140.

[90] Feng, H.Y. and Su, N., (2001), "A Mechanistic Cutting Force Model for 3D Ball-end Milling", *J. Manuf. Sci. Eng.*, Vol. 123, pp. 23-29.

[91] Zhang, W.-Y., Gao, H., Li, B.-Y., and Jiao, (2006), "A novel route for fabrication of machinable fluoramphibole glass-ceramics", *Scripta Materialia*, Vol. 55, pp. 275-278.

[92] Kasuga, T., Terada, M., and Nogami, M., (2001), "Machinable calcium pyrophosphate glass-ceramics", *J. Mater. Res.*, Vol. 16 No. 3, pp. 876-880.

[93] Wang, T.H. and James, P.F., (1990), "A new machinable phosphate based glass ceramics", *Inst. Physics. Conf. Ser.*, Vol. 111, pp. 401-410.

[94] Corning Inc., Professional Plastic, Macor Machining. Copyright © 2006 Corning Inc. http://www.professionalplastics/professionalplastics/content/MacorMachining.doc Date accessed: May 2007.

[95] Filser, F., Lüthy, H., Schärer, P., and Gauckler, L., (1998), All-ceramic dental bridges by direct ceramic machining (DCM). *Materials in Medicine, Materials Day, Department of Materials*. Edited by Speidel, M.O., Uggowitzer, P.G., and vdf Hochschulverlag, A.G., ETH Zürich, Zurich, pp. 165-189.

[96] Al-Shammery, H.A.O., Wood, D.J., Bubb, N.L., and Youngson, C.C., (2004), "Novel machinable mica based glass ceramics for dental applications", *Glass Technol.*, Vol. 45, pp. 88-90.

[97] Dudi, A. and Papini, M., (2007), "Design of a Prototype Bioresorbable Tibial Implant in a Sheep Model", *Proc. of 21st Canadian Congress of Applied Mechanics (CANCAM'07)*, Toronto, ON, June 3-7.

[98] Z Corporation. *ZPrinter 310 Plus User Manual*. Copyright© Rev A, August 2005 by Z Corporation. Date accessed: August 2006.

[99] Scartorius. *User's Manual Sartorius YDK 01, YDK 01-0D, YDK 01 LP Density Determination Kit*. Copyright© Scartorius. Date accessed: March 2007.

[100] Lien, S.M., Liu, C.K., and Huang, T.J., (2007), "A novel surface modification on calcium polyphosphate scaffold for articular cartilage tissue engineering", *Mater. Sci. Eng.*, Vol. 27, pp. 127-134.

[101] Mitutoyo Corporation. *Digimatic Calipers w/Absolute Encoders - Series 500*. Copyright© 2006 Mitutoyo Corporation. http://www.mitutoyo.com/TerminalMerchandisingGroup.aspx?group=1382. Date accessed: August 2006.

[102] Hanna Instruments Corporate. *HI 8064 Portable Thermohygrometer*. Copyright© 2006 Hanna Instruments. Date accessed: August 2006.

[103] Richerson, D.W., (1992), *Modern Ceramic Engineering: Properties, Processing, and Use in Design*. Marcel Dekker Inc., New York.

[104] Kingery, W.D., Bowen, H.K., and Uhlmann, D.R., (1976), *Introduction to Ceramics*. John Wiley & Sons Inc., Toronto.

[105] German, R.M., (1946), *Sintering Theory and Practice*. John Wiley & Sons Inc., New York.

[106] Reed, J.S., (1995), *Principles of Ceramics Processing*. John Wiley & Sons Inc., New York.

[107] Barsoum, M.W., (1997), *Fundamentals of Ceramics*. The McGraw-Hill Companies Inc., New York, pp. 391-440.

[108] Lee, W.E. and Rainforth, W.M., (1994), *Ceramic Microstructure: Property Control by Processing*. Chapman & Hall, London.

[109] Lewis, J.A., (1997), “Binder removal from ceramics”, *Annu. Rev. Mater. Sci.*, Vol. 27, pp. 147-173.

[110] Higgins, R.J., Rhine, W.E., Cima, M.J., and Bowen, H.K., (1994), “Ceramic surface reactions and carbon retention during non-oxidative binder removal: $Al_2O_3$/Poly(methyl methacrylate) at 20°-70°C”, *J. Am. Ceram. Soc.*, Vol. 77 No. 9, pp. 2243-2253.

[111] Moon, J., Grau, J.E., Knezevic, V., Cima, M.J., and Sachs, E.M., (2002), “Ink-Jet Printing of Binders for Ceramic Components”, *J. Am. Ceram. Soc.*, Vol. 85 No. 4, pp. 755–62.

[112] Lee P., Altintas Y. (1996), “Prediction of ball-end milling forces from orthogonal cutting data”, *Intl. J. Mach. Tools Manuf.*, Vol. 36, pp. 1059-1072.

[113] Sowa Tool and Machine Co. Ltd., *Sowa Tooling Solutions, Catalogue #ST0906*, http://www.sowatool.com/catalogue/carbide_endmills.html. Date accessed: July 2007.

[114] Rouzorkh, A., (2007), “Progress Report for University of Toronto”, May 04, 2007.

# Appendixes

# Appendix A

Table A1 and Table A2 include the width, length, and thickness measurements for all the pre-shaped and sintered samples produced using the indirect-3DP method from 106-150 μm and <75 CPP μm powder, respectively. These samples were used in the dimensional shrinkage analysis and the results are summarized in Section 3.2.3.1. The benchmark design for parts used in all the analyses in this appendix is presented in Section 3.2.2.1.

Appendix A1: Indirect-3DP Dimensional Shrinkage (106-150 μm samples).

| Sample # | Pre-shaped Dimensions | | | Sintered Dimensions | | | Shrinkage | | | |
|---|---|---|---|---|---|---|---|---|---|---|
| | x (mm) | y (mm) | z (mm) | x (mm) | y (mm) | z (mm) | x (%) | y (%) | z (%) | Overall (%) |
| 1 | 3.36 | 10.34 | 3.55 | 3.63 | 9.82 | 2.54 | -8.04% | 5.03% | 28.45% | 73.41% |
| 2 | 3.58 | 10.32 | 3.37 | 3.35 | 9.74 | 2.91 | 6.42% | 5.62% | 13.65% | 76.26% |
| 3 | 3.79 | 10.38 | 3.50 | 3.42 | 10.03 | 3.30 | 9.76% | 3.37% | 5.71% | 82.21% |
| 4 | 3.45 | 10.19 | 3.58 | 3.13 | 9.56 | 3.41 | 9.36% | 6.22% | 4.84% | 80.89% |
| 5 | 3.40 | 9.93 | 3.49 | 3.28 | 9.68 | 3.34 | 3.53% | 2.52% | 4.30% | 90.00% |
| 6 | 3.48 | 9.95 | 3.66 | 3.16 | 9.56 | 3.23 | 9.34% | 3.87% | 11.75% | 76.91% |
| 7 | 3.32 | 10.00 | 3.46 | 3.07 | 9.50 | 3.15 | 7.34% | 5.05% | 9.05% | 80.02% |
| 8 | 3.21 | 9.85 | 3.29 | 3.03 | 9.55 | 3.37 | 5.51% | 3.01% | -2.33% | 93.78% |
| 9 | 3.37 | 9.85 | 3.26 | 3.24 | 9.55 | 3.14 | 4.10% | 3.01% | 3.74% | 89.54% |
| 10 | 3.35 | 10.07 | 3.36 | 3.15 | 9.69 | 3.23 | 5.88% | 3.79% | 4.11% | 86.83% |
| 11 | 3.28 | 9.98 | 3.44 | 3.06 | 9.54 | 3.26 | 6.71% | 4.44% | 5.23% | 84.48% |
| 12 | 3.29 | 9.82 | 3.35 | 3.14 | 9.54 | 3.15 | 4.56% | 2.85% | 5.97% | 87.18% |
| 13 | 3.37 | 10.07 | 3.51 | 3.18 | 9.70 | 3.36 | 5.73% | 3.67% | 4.18% | 87.01% |
| 14 | 3.42 | 9.84 | 3.46 | 3.23 | 9.71 | 3.31 | 5.61% | 1.29% | 4.39% | 89.09% |
| 15 | 3.24 | 9.83 | 3.43 | 3.09 | 9.42 | 3.27 | 4.73% | 4.20% | 4.72% | 86.96% |
| 16 | 3.55 | 10.08 | 3.48 | 3.35 | 9.85 | 3.30 | 5.86% | 2.25% | 5.23% | 87.21% |
| 17 | 3.15 | 9.98 | 3.30 | 3.00 | 9.48 | 3.13 | 4.92% | 5.09% | 5.25% | 85.50% |
| 18 | 3.21 | 9.74 | 3.49 | 3.05 | 9.36 | 3.28 | 4.98% | 3.93% | 5.93% | 85.87% |
| 19 | 3.26 | 9.93 | 3.49 | 3.12 | 9.51 | 3.25 | 4.45% | 4.28% | 6.97% | 85.09% |
| 20 | 3.24 | 9.88 | 3.23 | 3.09 | 9.56 | 3.06 | 4.88% | 3.26% | 5.42% | 87.03% |
| 21 | 3.31 | 10.01 | 3.45 | 3.17 | 9.53 | 3.33 | 4.28% | 4.76% | 3.57% | 87.90% |
| 22 | 3.28 | 10.01 | 3.44 | 3.10 | 9.59 | 3.23 | 5.49% | 4.28% | 6.10% | 84.95% |
| 23 | 3.29 | 9.89 | 3.39 | 3.22 | 9.60 | 3.20 | 2.03% | 2.98% | 5.66% | 89.67% |
| 24 | 3.39 | 9.73 | 3.24 | 3.21 | 9.34 | 3.07 | 5.32% | 3.96% | 5.26% | 86.16% |
| 25 | 3.21 | 9.81 | 3.43 | 3.06 | 9.38 | 3.22 | 4.83% | 4.40% | 6.21% | 85.33% |
| 26 | 3.26 | 9.94 | 3.33 | 3.09 | 9.37 | 3.27 | 5.37% | 5.77% | 1.90% | 87.48% |
| 27 | 3.42 | 10.03 | 3.32 | 3.28 | 9.71 | 3.05 | 4.09% | 3.21% | 8.22% | 85.20% |
| 28 | 3.36 | 9.79 | 3.43 | 3.24 | 9.51 | 3.24 | 3.48% | 2.94% | 5.55% | 88.49% |
| 29 | 3.36 | 9.81 | 3.42 | 3.24 | 9.55 | 3.27 | 3.82% | 2.65% | 4.53% | 89.39% |
| 30 | 3.44 | 10.04 | 3.47 | 3.31 | 9.65 | 3.35 | 3.83% | 3.88% | 3.60% | 89.10% |
| 31 | 3.24 | 9.86 | 3.58 | 3.09 | 9.58 | 3.41 | 4.63% | 2.86% | 4.75% | 88.25% |
| 32 | 3.25 | 9.79 | 3.34 | 3.21 | 9.40 | 3.06 | 1.28% | 3.98% | 8.47% | 86.75% |
| 33 | 3.35 | 9.83 | 3.49 | 3.19 | 9.42 | 3.31 | 4.68% | 4.20% | 5.02% | 86.73% |

| | | | | | | | | | | |
|---|---|---|---|---|---|---|---|---|---|---|
| 34 | 3.34 | 9.87 | 3.39 | 3.23 | 9.75 | 3.24 | 3.39% | 1.22% | 4.33% | 91.30% |
| 35 | 3.30 | 9.83 | 3.40 | 3.18 | 9.65 | 3.29 | 3.64% | 1.92% | 3.38% | 91.32% |
| 36 | 3.53 | 9.98 | 3.59 | 3.38 | 9.64 | 3.39 | 4.48% | 3.46% | 5.48% | 87.16% |
| 37 | 3.49 | 9.91 | 3.54 | 3.30 | 9.49 | 3.36 | 5.35% | 4.24% | 5.17% | 85.95% |
| 38 | 3.23 | 9.77 | 3.39 | 3.05 | 9.37 | 3.23 | 5.57% | 4.18% | 4.72% | 86.21% |
| 39 | 3.14 | 9.79 | 3.40 | 3.02 | 9.37 | 3.28 | 3.67% | 4.37% | 3.53% | 88.87% |

## Appendix A2: Indirect-3DP Dimensional Shrinkage (<75 µm samples).

| Sample # | Pre-shaped Dimensions | | | Sintered Dimensions | | | Shrinkage | | | |
|---|---|---|---|---|---|---|---|---|---|---|
| | x (mm) | y (mm) | z (mm) | x (mm) | y (mm) | z (mm) | x (%) | y (%) | z (%) | Overall (%) |
| 1 | 3.69 | 10.36 | 3.55 | 3.23 | 9.31 | 3.03 | 12.47% | 10.14% | 14.65% | 67.14% |
| 2 | 3.54 | 10.34 | 3.4 | 3.06 | 9.89 | 3.10 | 13.56% | 4.35% | 8.82% | 75.38% |
| 3 | 3.79 | 10.3 | 3.48 | 3.25 | 9.91 | 3.14 | 14.25% | 3.79% | 9.77% | 74.44% |
| 4 | 4.05 | 10.5 | 3.53 | 3.20 | 9.69 | 3.04 | 20.99% | 7.71% | 13.88% | 62.80% |
| 5 | 4.01 | 10.89 | 3.58 | 3.75 | 10.53 | 3.34 | 6.48% | 3.31% | 6.70% | 84.36% |
| 6 | 3.55 | 10.89 | 3.72 | 3.36 | 10.03 | 3.58 | 5.35% | 7.90% | 3.76% | 83.89% |
| 7 | 3.58 | 10.71 | 3.73 | 4.01 | 10.15 | 3.08 | -12.01% | 5.23% | 17.43% | 87.66% |
| 8 | 3.71 | 10.89 | 3.5 | 3.15 | 9.86 | 3.30 | 15.09% | 9.46% | 5.71% | 72.48% |
| 9 | 3.87 | 10.43 | 3.58 | 3.31 | 9.94 | 3.24 | 14.47% | 4.70% | 9.50% | 73.77% |
| 10 | 3.87 | 10.38 | 3.54 | 3.20 | 9.85 | 3.13 | 17.31% | 5.11% | 11.58% | 69.38% |
| 11 | 3.43 | 10.41 | 3.42 | 3.29 | 9.20 | 3.12 | 4.08% | 11.62% | 8.77% | 77.33% |
| 12 | 3.73 | 9.85 | 3.43 | 3.14 | 9.47 | 3.06 | 15.82% | 3.86% | 10.79% | 72.20% |
| 13 | 3.56 | 10.33 | 3.34 | 3.39 | 9.00 | 3.14 | 4.78% | 12.88% | 5.99% | 78.00% |
| 14 | 3.67 | 10.11 | 3.56 | 3.30 | 9.44 | 3.06 | 10.08% | 6.63% | 14.04% | 72.17% |
| 15 | 3.37 | 10.50 | 3.71 | 3.20 | 9.97 | 3.30 | 5.04% | 5.10% | 11.27% | 79.96% |
| 16 | 3.59 | 10.70 | 3.47 | 3.33 | 9.92 | 3.04 | 7.24% | 7.29% | 12.27% | 75.45% |
| 17 | 3.39 | 10.80 | 3.51 | 3.21 | 10.23 | 3.36 | 5.32% | 5.32% | 4.14% | 85.93% |
| 18 | 3.45 | 10.58 | 3.35 | 3.20 | 10.01 | 3.20 | 7.39% | 5.34% | 4.33% | 83.86% |
| 19 | 3.65 | 10.36 | 3.53 | 3.44 | 10.46 | 3.43 | 5.67% | -0.88% | 2.83% | 92.47% |
| 20 | 3.43 | 10.52 | 3.38 | 3.15 | 9.88 | 3.14 | 8.18% | 6.13% | 7.11% | 80.07% |
| 21 | 3.49 | 10.10 | 3.51 | 3.21 | 9.72 | 3.25 | 8.03% | 3.76% | 7.55% | 81.82% |
| 22 | 3.53 | 10.65 | 3.45 | 3.38 | 10.00 | 3.23 | 4.11% | 6.11% | 6.52% | 84.16% |
| 23 | 3.45 | 10.78 | 3.34 | 3.36 | 10.45 | 3.43 | 2.61% | 3.06% | -2.70% | 96.96% |
| 24 | 3.45 | 10.44 | 3.57 | 3.15 | 10.07 | 3.29 | 8.47% | 3.50% | 7.84% | 81.40% |
| 25 | 3.64 | 10.42 | 3.74 | 3.38 | 9.97 | 3.49 | 7.15% | 4.37% | 6.56% | 82.97% |
| 26 | 3.59 | 10.29 | 3.39 | 3.34 | 9.96 | 3.11 | 6.97% | 3.16% | 8.12% | 82.77% |
| 27 | 3.56 | 10.30 | 3.43 | 3.39 | 9.86 | 3.21 | 4.78% | 4.32% | 6.28% | 85.39% |
| 28 | 3.69 | 10.41 | 3.58 | 3.51 | 9.95 | 3.35 | 5.01% | 4.42% | 6.29% | 85.08% |
| 29 | 3.48 | 10.43 | 3.35 | 3.37 | 9.97 | 3.19 | 3.02% | 4.46% | 4.78% | 88.22% |
| 30 | 3.33 | 10.70 | 3.44 | 3.17 | 10.08 | 3.14 | 4.80% | 5.84% | 8.87% | 81.69% |
| 31 | 3.59 | 10.45 | 3.27 | 3.41 | 9.83 | 3.13 | 5.15% | 5.98% | 4.43% | 85.22% |
| 32 | 3.38 | 10.26 | 3.20 | 3.32 | 9.69 | 3.08 | 1.78% | 5.56% | 3.75% | 89.29% |
| 33 | 3.65 | 10.44 | 3.34 | 3.41 | 9.97 | 3.22 | 6.71% | 4.55% | 3.59% | 85.84% |
| 34 | 3.60 | 10.68 | 3.54 | 3.42 | 9.57 | 3.29 | 5.00% | 10.39% | 6.97% | 79.19% |
| 35 | 3.36 | 10.33 | 3.22 | 3.27 | 10.05 | 3.20 | 2.83% | 2.71% | 0.78% | 93.80% |
| 36 | 3.50 | 10.58 | 3.40 | 3.41 | 10.16 | 3.06 | 2.57% | 3.97% | 10.00% | 84.20% |
| 37 | 3.62 | 10.38 | 3.38 | 3.32 | 10.01 | 3.18 | 8.29% | 3.61% | 6.07% | 83.04% |
| 38 | 3.64 | 10.20 | 3.57 | 3.50 | 9.94 | 3.34 | 3.85% | 2.60% | 6.58% | 87.49% |
| 39 | 3.61 | 10.77 | 3.40 | 3.47 | 9.91 | 3.33 | 3.88% | 8.03% | 1.91% | 86.70% |
| 40 | 3.56 | 10.56 | 3.44 | 3.35 | 10.16 | 3.25 | 5.99% | 3.84% | 5.67% | 85.28% |

| | | | | | | | | | | |
|---|---|---|---|---|---|---|---|---|---|---|
| 41 | 3.57 | 10.42 | 3.29 | 3.29 | 10.15 | 3.15 | 7.98% | 2.59% | 4.26% | 85.82% |
| 42 | 3.65 | 10.35 | 3.32 | 3.54 | 10.10 | 3.23 | 3.01% | 2.46% | 2.71% | 92.03% |
| 43 | 3.74 | 10.30 | 3.40 | 3.45 | 9.88 | 3.17 | 7.75% | 4.08% | 6.76% | 82.50% |
| 44 | 3.63 | 10.40 | 3.45 | 3.43 | 10.03 | 3.30 | 5.51% | 3.51% | 4.35% | 87.21% |

Table A3 and Table A4 include the following measurements: dry weight in air ($W_d$), submersed weight ($W_s$), wet weight ($W_w$), density of the fluid ($\rho_{fl}$), density of the solid ($\rho_{solid}$), volume of pores ($V_{pores}$), and the bulk density ($\rho_{bulk}$) of all the sintered samples produced using the indirect-3DP method from the 106-150 μm and <75 CPP μm CPP powder, respectively. These samples were used in the density analysis and the results are presented in Section 3.2.2.2.

Appendix A3: Indirect-3DP Density – Archimedes Principle (106-150 μm samples).

| Sample # | $W_d$ (g) | $W_d$-$W_s$ (--) | $T_l$ (°C) | $\rho_{fl}$ (g/cm$^3$) | $W_w$ (g) | $\rho_{solid}$ (g/cm3) | $V_{pores}$ (cm3) | $\rho_{bulk}$ (g/cm3) | % Full Density | % Volume Porosity |
|---|---|---|---|---|---|---|---|---|---|---|
| 1 | 0.1327 | 0.0450 | 23.1 | 0.78669 | 0.1387 | 2.2861 | 0.0076 | 2.0206 | 70.90% | 29.10% |
| 2 | 0.1440 | 0.0434 | 23.2 | 0.78660 | 0.1500 | 2.5717 | 0.0076 | 2.2634 | 79.42% | 20.58% |
| 3 | 0.1394 | 0.0428 | 23.4 | 0.78643 | 0.1454 | 2.5240 | 0.0076 | 2.2176 | 77.81% | 22.19% |
| 4 | 0.1470 | 0.0487 | 23.2 | 0.78660 | 0.15300 | 2.33971 | 0.00763 | 2.08641 | 73.21% | 26.79% |
| 5 | 0.1359 | 0.0444 | 23.2 | 0.78660 | 0.14190 | 2.37251 | 0.00763 | 2.09370 | 73.46% | 26.54% |
| 6 | 0.1360 | 0.0438 | 23.1 | 0.78669 | 0.14200 | 2.40704 | 0.00763 | 2.12076 | 74.41% | 25.59% |
| 7 | 0.1504 | 0.0432 | 23.90 | 0.78600 | 0.1674 | 2.7339 | 0.0216 | 1.9624 | 68.86% | 31.14% |
| 8 | 0.1380 | 0.0417 | 23.90 | 0.78600 | 0.1550 | 2.5988 | 0.0216 | 1.8467 | 64.80% | 35.20% |
| 9 | 0.1411 | 0.0426 | 23.90 | 0.78600 | 0.1581 | 2.6011 | 0.0216 | 1.8596 | 65.25% | 34.75% |
| 10 | 0.1479 | 0.0442 | 23.90 | 0.78600 | 0.1649 | 2.6277 | 0.0216 | 1.8983 | 66.61% | 33.39% |
| 11 | 0.1309 | 0.0377 | 23.90 | 0.78600 | 0.1479 | 2.7266 | 0.0216 | 1.8798 | 65.96% | 34.04% |
| 12 | 0.1199 | 0.0355 | 23.90 | 0.78600 | 0.1369 | 2.6523 | 0.0216 | 1.7940 | 62.95% | 37.05% |
| 13 | 0.1390 | 0.0411 | 23.90 | 0.78600 | 0.1560 | 2.6558 | 0.0216 | 1.8792 | 65.94% | 34.06% |
| 14 | 0.1392 | 0.0406 | 23.90 | 0.78600 | 0.1562 | 2.6924 | 0.0216 | 1.8983 | 66.61% | 33.39% |
| 15 | 0.1242 | 0.0358 | 23.90 | 0.78600 | 0.1412 | 2.7243 | 0.0216 | 1.8477 | 64.83% | 35.17% |
| 16 | 0.1383 | 0.0401 | 23.90 | 0.78600 | 0.1553 | 2.7083 | 0.0216 | 1.9025 | 66.76% | 33.24% |
| 17 | 0.1351 | 0.0401 | 23.90 | 0.78600 | 0.1551 | 2.6457 | 0.0254 | 1.7658 | 61.96% | 38.04% |
| 18 | 0.1369 | 0.0405 | 23.90 | 0.78600 | 0.1549 | 2.6545 | 0.0229 | 1.8382 | 64.50% | 35.50% |
| 19 | 0.1390 | 0.0428 | 23.90 | 0.78600 | 0.1590 | 2.5504 | 0.0254 | 1.7387 | 61.01% | 38.99% |
| 20 | 0.1328 | 0.0388 | 23.90 | 0.78600 | 0.1483 | 2.6878 | 0.0197 | 1.9210 | 67.41% | 32.59% |
| 21 | 0.1368 | 0.0413 | 23.90 | 0.78600 | 0.1508 | 2.6012 | 0.0178 | 1.9431 | 68.18% | 31.82% |
| 22 | 0.1319 | 0.0400 | 23.90 | 0.78600 | 0.1479 | 2.5895 | 0.0204 | 1.8501 | 64.92% | 35.08% |
| 23 | 0.1280 | 0.0398 | 23.90 | 0.78600 | 0.1460 | 2.5256 | 0.0229 | 1.7396 | 61.04% | 38.96% |
| 24 | 0.1358 | 0.0418 | 23.90 | 0.78600 | 0.1518 | 2.5513 | 0.0204 | 1.8455 | 64.75% | 35.25% |
| 25 | 0.1372 | 0.0420 | 23.90 | 0.78600 | 0.1557 | 2.5653 | 0.0235 | 1.7814 | 62.50% | 37.50% |
| 26 | 0.1381 | 0.0418 | 23.90 | 0.78600 | 0.1566 | 2.5945 | 0.0235 | 1.7990 | 63.12% | 36.88% |
| 27 | 0.1256 | 0.0389 | 23.90 | 0.78600 | 0.1406 | 2.5356 | 0.0191 | 1.8304 | 64.22% | 35.78% |
| 28 | 0.1328 | 0.0391 | 23.90 | 0.78600 | 0.1498 | 2.6672 | 0.0216 | 1.8594 | 65.24% | 34.76% |
| 29 | 0.1375 | 0.0431 | 23.90 | 0.78600 | 0.1455 | 2.5053 | 0.0102 | 2.1134 | 74.15% | 25.85% |

|  |  |  |  |  |  |  |  |  |  |  |
|---|---|---|---|---|---|---|---|---|---|---|
| 30 | 0.1428 | 0.0373 | 23.90 | 0.78600 | 0.1598 | 3.0046 | 0.0216 | 2.0649 | 72.45% | 27.55% |
| 31 | 0.1257 | 0.0430 | 23.95 | 0.78596 | 0.1507 | 2.2956 | 0.0318 | 1.4521 | 50.95% | 49.05% |
| 32 | 0.1453 | 0.0457 | 23.95 | 0.78596 | 0.1623 | 2.4967 | 0.0216 | 1.8202 | 63.87% | 36.13% |
| 33 | 0.1515 | 0.0463 | 23.95 | 0.78596 | 0.1685 | 2.5695 | 0.0216 | 1.8799 | 65.96% | 34.04% |
| 34 | 0.1453 | 0.0431 | 23.95 | 0.78596 | 0.1608 | 2.6472 | 0.0197 | 1.9475 | 68.33% | 31.67% |
| 35 | 0.1366 | 0.0419 | 23.95 | 0.78596 | 0.1546 | 2.5601 | 0.0229 | 1.7912 | 62.85% | 37.15% |
| 36 | 0.1410 | 0.0429 | 23.95 | 0.78596 | 0.1595 | 2.5809 | 0.0235 | 1.8038 | 63.29% | 36.71% |
| 37 | 0.1390 | 0.0424 | 23.95 | 0.78596 | 0.1560 | 2.5743 | 0.0216 | 1.8380 | 64.49% | 35.51% |
| 38 | 0.1387 | 0.0454 | 23.95 | 0.78596 | 0.1572 | 2.3991 | 0.0235 | 1.7049 | 59.82% | 40.18% |
| 39 | 0.1539 | 0.0759 | 23.95 | 0.78596 | 0.1734 | 1.5927 | 0.0248 | 1.2673 | 44.47% | 55.53% |
| 40 | 0.1514 | 0.0464 | 23.95 | 0.78596 | 0.1684 | 2.5622 | 0.0216 | 1.8757 | 65.81% | 34.19% |
| 41 | 0.1344 | 0.0409 | 23.95 | 0.78596 | 0.1464 | 2.5804 | 0.0153 | 1.9955 | 70.02% | 29.98% |
| 42 | 0.1275 | 0.0389 | 23.95 | 0.78596 | 0.1440 | 2.5738 | 0.0210 | 1.8077 | 63.43% | 36.57% |

## Appendix A4: Indirect-3DP Density – Archimedes Principle (<75 µm samples).

| Sample # | $W_d$ (g) | $W_d$-$W_s$ (--) | $T_l$ (°C) | $\rho_{fl}$ ($g/cm^3$) | $W_w$ (g) | $\rho_{solid}$ (g/cm3) | $V_{pores}$ (cm3) | $\rho_{bulk}$ (g/cm3) | % Full Density | % Volume Porosity |
|---|---|---|---|---|---|---|---|---|---|---|
| 1 | 0.1429 | 0.0460 | 22.5 | 0.78720 | 0.1464 | 2.4098 | 0.0044 | 2.4098 | 84.55% | 15.45% |
| 2 | 0.1455 | 0.0469 | 22.5 | 0.78720 | 0.1517 | 2.4065 | 0.0078 | 2.4065 | 84.44% | 15.56% |
| 3 | 0.1554 | 0.0505 | 22.4 | 0.78729 | 0.1616 | 2.3873 | 0.0078 | 2.3873 | 83.77% | 16.23% |
| 4 | 0.1403 | 0.0641 | 22.5 | 0.78720 | 0.1465 | 1.6982 | 0.0078 | 1.6982 | 59.59% | 40.41% |
| 5 | 0.1675 | 0.0521 | 22.3 | 0.78738 | 0.1737 | 2.4944 | 0.0078 | 2.4944 | 87.52% | 12.48% |
| 6 | 0.1656 | 0.0572 | 23.1 | 0.78669 | 0.1718 | 2.2444 | 0.0078 | 2.2444 | 78.75% | 21.25% |
| 7 | 0.1694 | 0.0576 | 23.0 | 0.78678 | 0.1756 | 2.2802 | 0.0078 | 2.2802 | 80.01% | 19.99% |
| 8 | 0.1337 | 0.0469 | 22.9 | 0.78686 | 0.1387 | 2.2105 | 0.0064 | 2.2105 | 77.56% | 22.44% |
| 9 | 0.1460 | 0.0522 | 22.5 | 0.78720 | 0.1522 | 2.1698 | 0.0078 | 2.1698 | 76.13% | 23.87% |
| 10 | 0.1440 | 0.0462 | 22.5 | 0.78720 | 0.1502 | 2.4178 | 0.0078 | 2.4178 | 84.84% | 15.16% |
| 11 | 0.1470 | 0.0499 | 22.6 | 0.78712 | 0.1610 | 2.2850 | 0.0178 | 2.2850 | 80.18% | 19.82% |
| 12 | 0.1402 | 0.0460 | 22.3 | 0.78738 | 0.1432 | 2.3648 | 0.0038 | 2.3648 | 82.98% | 17.02% |
| 13 | 0.1435 | 0.0467 | 22.3 | 0.78738 | 0.1490 | 2.3842 | 0.0070 | 2.3842 | 83.66% | 16.34% |
| 14 | 0.1531 | 0.0529 | 22.3 | 0.78738 | 0.1593 | 2.2456 | 0.0078 | 2.2456 | 78.79% | 21.21% |
| 15 | 0.1499 | 0.0499 | 22.3 | 0.78738 | 0.1559 | 2.3308 | 0.0076 | 2.3308 | 81.78% | 18.22% |
| 16 | 0.1377 | 0.0426 | 23.6 | 0.78626 | 0.1572 | 2.5393 | 0.0248 | 1.7424 | 61.14% | 38.86% |
| 17 | 0.1350 | 0.0413 | 23.6 | 0.78626 | 0.1530 | 2.5678 | 0.0229 | 1.7889 | 62.77% | 37.23% |
| 18 | 0.1435 | 0.0437 | 23.6 | 0.78626 | 0.1685 | 2.5796 | 0.0318 | 1.6414 | 57.59% | 42.41% |
| 19 | 0.1328 | 0.0408 | 23.6 | 0.78626 | 0.1578 | 2.5569 | 0.0318 | 1.5860 | 55.65% | 44.35% |
| 20 | 0.1450 | 0.0473 | 23.6 | 0.78626 | 0.1690 | 2.4082 | 0.0305 | 1.5981 | 56.07% | 43.93% |
| 21 | 0.1325 | 0.0411 | 23.6 | 0.78626 | 0.1515 | 2.5325 | 0.0242 | 1.7324 | 60.79% | 39.21% |
| 22 | 0.1369 | 0.0444 | 23.6 | 0.78626 | 0.1469 | 2.4222 | 0.0127 | 1.9773 | 69.38% | 30.62% |
| 23 | 0.1338 | 0.0434 | 23.6 | 0.78626 | 0.1478 | 2.4219 | 0.0178 | 1.8316 | 64.27% | 35.73% |
| 24 | 0.1440 | 0.0543 | 23.6 | 0.78626 | 0.1565 | 2.0835 | 0.0159 | 1.6939 | 59.43% | 40.57% |
| 25 | 0.1352 | 0.0440 | 23.75 | 0.78614 | 0.1547 | 2.4135 | 0.0248 | 1.6728 | 58.69% | 41.31% |
| 26 | 0.1458 | 0.0972 | 23.75 | 0.78614 | 0.1648 | 1.1788 | 0.0242 | 0.9861 | 34.60% | 65.40% |
| 27 | 0.1314 | 0.0458 | 23.75 | 0.78614 | 0.1464 | 2.2536 | 0.0191 | 1.6979 | 59.58% | 40.42% |
| 28 | 0.1381 | 0.0480 | 23.75 | 0.78614 | 0.1571 | 2.2599 | 0.0242 | 1.6194 | 56.82% | 43.18% |
| 29 | 0.1544 | 0.0516 | 23.75 | 0.78614 | 0.1674 | 2.3503 | 0.0165 | 1.8777 | 65.88% | 34.12% |
| 30 | 0.1333 | 0.0469 | 23.75 | 0.78614 | 0.1453 | 2.2325 | 0.0153 | 1.7780 | 62.39% | 37.61% |
| 31 | 0.1322 | 0.0409 | 23.75 | 0.78614 | 0.1552 | 2.5388 | 0.0293 | 1.6255 | 57.03% | 42.97% |
| 32 | 0.1347 | 0.0411 | 23.75 | 0.78614 | 0.1547 | 2.5742 | 0.0254 | 1.7321 | 60.77% | 39.23% |
| 33 | 0.1327 | 0.0396 | 23.75 | 0.78614 | 0.1507 | 2.6320 | 0.0229 | 1.8100 | 63.51% | 36.49% |

| | | | | | | | | | | |
|---|---|---|---|---|---|---|---|---|---|---|
| 34 | 0.1329 | 0.0401 | 23.75 | 0.78614 | 0.1524 | 2.6031 | 0.0248 | 1.7519 | 61.47% | 38.53% |
| 35 | 0.1586 | 0.0508 | 23.75 | 0.78614 | 0.1776 | 2.4522 | 0.0242 | 1.7851 | 62.64% | 37.36% |
| 36 | 0.1401 | 0.0430 | 23.75 | 0.78614 | 0.1636 | 2.5591 | 0.0299 | 1.6553 | 58.08% | 41.92% |
| 37 | 0.1427 | 0.0459 | 23.75 | 0.78614 | 0.1627 | 2.4419 | 0.0254 | 1.7013 | 59.69% | 40.31% |
| 38 | 0.1317 | 0.0399 | 23.75 | 0.78614 | 0.1537 | 2.5925 | 0.0280 | 1.6716 | 58.65% | 41.35% |
| 39 | 0.1463 | 0.0461 | 23.75 | 0.78614 | 0.1703 | 2.4927 | 0.0305 | 1.6397 | 57.53% | 42.47% |
| 40 | 0.1411 | 0.0456 | 23.75 | 0.78614 | 0.1576 | 2.4305 | 0.0210 | 1.7851 | 62.63% | 37.37% |
| 41 | 0.1358 | 0.0467 | 23.75 | 0.78614 | 0.1548 | 2.2841 | 0.0242 | 1.6240 | 56.98% | 43.02% |
| 42 | 0.1426 | 0.0457 | 23.75 | 0.78614 | 0.1626 | 2.4509 | 0.0254 | 1.7053 | 59.83% | 40.17% |
| 43 | 0.1372 | 0.0431 | 23.75 | 0.78614 | 0.1612 | 2.5003 | 0.0305 | 1.6065 | 56.37% | 43.63% |
| 44 | 0.1417 | 0.0492 | 23.75 | 0.78614 | 0.1607 | 2.2623 | 0.0242 | 1.6324 | 57.28% | 42.72% |
| 45 | 0.1363 | 0.0433 | 23.75 | 0.78614 | 0.1553 | 2.4725 | 0.0242 | 1.7189 | 60.31% | 39.69% |

Table A5 and Table A6 include the width, length, and thickness measurements for all the pre-shaped and sintered samples produced using the direct-3DP method with 45-75 µm CPP powder and sintered at 592 and 585°C, respectively. These samples were used in the dimensional analysis and the results are summarized in Section 3.2.3.1.

## Appendix A5: Direct-3DP Dimensional Shrinkage (@ 592°C)

| Sample # | Pre-shaped Dimensions | | | Sintered Dimensions | | | Shrinkage | | | |
|---|---|---|---|---|---|---|---|---|---|---|
| | x (mm) | y (mm) | z (mm) | x (mm) | y (mm) | z (mm) | x (%) | y (%) | z (%) | Overall (%) |
| 1 | 3.40 | 10.06 | 3.11 | 2.83 | 8.59 | 2.53 | 16.91% | 14.66% | 18.65% | 57.68% |
| 2 | 3.33 | 10.04 | 3.03 | 2.59 | 8.46 | 2.76 | 22.37% | 15.74% | 8.91% | 59.58% |
| 3 | 3.22 | 9.98 | 3.07 | 2.72 | 8.38 | 2.53 | 15.53% | 16.08% | 17.75% | 58.30% |
| 4 | 3.34 | 9.96 | 3.08 | 2.73 | 8.42 | 2.36 | 18.41% | 15.46% | 23.38% | 52.85% |
| 5 | 3.20 | 9.86 | 3.03 | 2.62 | 8.20 | 2.16 | 18.13% | 16.84% | 28.88% | 48.43% |
| 6 | 3.36 | 9.87 | 3.03 | 2.50 | 8.35 | 2.59 | 25.60% | 15.40% | 14.52% | 53.81% |
| 7 | 3.36 | 9.97 | 3.12 | 2.79 | 8.83 | 2.01 | 17.11% | 11.43% | 35.74% | 47.17% |
| 8 | 3.22 | 9.91 | 3.02 | 2.51 | 8.57 | 2.00 | 22.05% | 13.52% | 33.77% | 44.64% |

## Appendix A6: Direct-3DP Dimensional Shrinkage (@ 585°C)

| Sample # | Pre-shaped Dimensions | | | Sintered Dimensions | | | Shrinkage | | | |
|---|---|---|---|---|---|---|---|---|---|---|
| | x (mm) | y (mm) | z (mm) | x (mm) | y (mm) | z (mm) | x (%) | y (%) | z (%) | Overall (%) |
| 1 | 3.23 | 10.18 | 3.37 | 2.86 | 8.81 | 2.83 | 11.46% | 13.51% | 16.05% | 64.30% |
| 2 | 3.28 | 10.09 | 3.33 | 2.79 | 8.95 | 2.93 | 14.81% | 11.30% | 11.98% | 66.51% |
| 3 | 3.35 | 10.06 | 3.48 | 2.88 | 8.70 | 3.02 | 14.05% | 13.57% | 13.24% | 64.45% |
| 4 | 3.23 | 10.22 | 3.41 | 2.94 | 9.02 | 2.90 | 8.99% | 11.75% | 14.98% | 68.29% |
| 5 | 2.74 | 8.12 | 3.74 | 2.32 | 7.14 | 3.27 | 15.17% | 12.01% | 12.64% | 65.20% |
| 6 | 3.33 | 10.02 | 3.41 | 2.79 | 8.79 | 2.99 | 16.24% | 12.23% | 12.46% | 64.35% |
| 7 | 3.33 | 10.21 | 3.45 | 3.06 | 9.01 | 2.92 | 7.97% | 11.75% | 15.38% | 68.72% |
| 8 | 3.30 | 10.14 | 3.52 | 2.97 | 9.01 | 2.95 | 10.02% | 11.14% | 16.07% | 67.10% |
| 9 | 3.26 | 10.28 | 3.52 | 2.99 | 8.91 | 2.99 | 8.44% | 13.33% | 15.06% | 67.41% |
| 10 | 2.75 | 12.00 | 3.20 | 2.33 | 10.44 | 2.83 | 15.45% | 12.96% | 11.42% | 65.18% |

| | | | | | | | | | | |
|---|---|---|---|---|---|---|---|---|---|---|
| 11 | 2.75 | 12.07 | 3.16 | 2.37 | 10.64 | 2.69 | 14.00% | 11.89% | 14.74% | 64.61% |

Table A7 and Table A8 include the following measurements: dry weight in air ($W_d$), submersed weight ($W_s$), wet weight ($W_w$), density of the fluid ($\rho_{fl}$), density of the solid ($\rho_{solid}$), volume of pores ($V_{pores}$), and the bulk density ($\rho_{bulk}$) of all the sintered samples produced using the direct-3DP method and sintered at 592 and 585°C, respectively. These samples were used in the density analysis and the results are presented in Section 3.3.3.2.

## Appendix A7: Direct-3DP Density – Archimedes Principle (@ 592°C)

| Sample # | w(a) (g) | G (--) | $T_l$ (°C) | density_l (g/cm$^3$) | W(w) | p_mat'l (g/cm3) | V_eth (cm3) | p_bulk (g/cm3) | % full density | % volume porosity |
|---|---|---|---|---|---|---|---|---|---|---|
| 1 | 0.0803 | 0.0227 | 23.8 | 0.78609 | 0.0922 | 2.7782 | 0.0151 | 1.8233 | 63.97% | 36.03% |
| 2 | 0.0735 | 0.0206 | 23.8 | 0.78609 | 0.0910 | 2.8021 | 0.0223 | 1.5157 | 53.18% | 46.82% |
| 3 | 0.0630 | 0.0177 | 23.9 | 0.78600 | 0.0815 | 2.7950 | 0.0235 | 1.3673 | 47.97% | 52.03% |
| 4 | 0.0738 | 0.0218 | 23.8 | 0.78609 | 0.0868 | 2.6588 | 0.0165 | 1.6661 | 58.46% | 41.54% |
| 5 | 0.0689 | 0.0216 | 23.7 | 0.78618 | 0.0754 | 2.5056 | 0.0083 | 1.9264 | 67.59% | 32.41% |
| 6 | 0.0683 | 0.0202 | 23.7 | 0.78618 | 0.0802 | 2.6558 | 0.0151 | 1.6718 | 58.66% | 41.34% |
| 7 | 0.0783 | 0.0278 | 23.7 | 0.78618 | 0.0803 | 2.2125 | 0.0025 | 2.0641 | 72.43% | 27.57% |
| 8 | 0.0640 | 0.0218 | 23.6 | 0.78626 | 0.0759 | 2.3064 | 0.0151 | 1.4924 | 52.36% | 47.64% |

## Appendix A8: Direcft-3DP Density – Archimedes Principle (@ 585°C)

| Sample # | $W_d$ (g) | $W_d$-$W_s$ (--) | $T_l$ (°C) | $\rho_{fl}$ (g/cm$^3$) | $W_w$ (g) | $\rho_{solid}$ (g/cm3) | $V_{pores}$ (cm3) | $\rho_{bulk}$ (g/cm3) | % Full Density | % Volume Porosity |
|---|---|---|---|---|---|---|---|---|---|---|
| 1 | 0.0777 | 0.0226 | 24.5 | 0.78594 | 0.09520 | 2.6996 | 0.0223 | 1.5221 | 53.41% | 46.59% |
| 2 | 0.0731 | 0.0216 | 24.5 | 0.78566 | 0.09060 | 2.6565 | 0.0223 | 1.4681 | 51.51% | 48.49% |
| 3 | 0.0860 | 0.0257 | 24.3 | 0.78592 | 0.10500 | 2.6276 | 0.0242 | 1.5113 | 53.03% | 46.97% |
| 4 | 0.0779 | 0.0233 | 24.3 | 0.78566 | 0.09540 | 2.6244 | 0.0223 | 1.4993 | 52.61% | 47.39% |
| 5 | 0.0581 | 0.0171 | 24.2 | 0.78575 | 0.07260 | 2.6673 | 0.0185 | 1.4440 | 50.67% | 49.33% |
| 6 | 0.0764 | 0.0221 | 24.0 | 0.78592 | 0.09590 | 2.7144 | 0.0248 | 1.4427 | 50.62% | 49.38% |
| 7 | 0.0879 | 0.0261 | 24.0 | 0.78592 | 0.10540 | 2.6444 | 0.0223 | 1.5836 | 55.56% | 44.44% |
| 8 | 0.0896 | 0.0269 | 24.0 | 0.78592 | 0.10510 | 2.6154 | 0.0197 | 1.6599 | 58.24% | 41.76% |
| 9 | 0.0927 | 0.0284 | 24.1 | 0.78583 | 0.11020 | 2.5627 | 0.0223 | 1.5862 | 55.66% | 44.34% |
| 10 | 0.0687 | 0.0198 | 24.1 | 0.78583 | 0.08770 | 2.7241 | 0.0242 | 1.3908 | 48.80% | 51.20% |
| 11 | 0.0717 | 0.0205 | 24.5 | 0.78594 | 0.09580 | 2.7463 | 0.0307 | 1.2630 | 44.31% | 55.69% |

# Appendix B

Table B1 includes the designed and measured dimensions of parts produced using the ZPrinter® 310 Plus with the default plaster-based powder and aqueous-based binder in use for the achievable dimensional accuracy analysis. The benchmark design used is described in Section 3.4.1. The nominal dimensions of the produced parts vary from 2.0, 2.5, 4.0, 12.0, 15.0, 18.0, to 20.0 mm.

Table B1: Dimensions measured for 3DP accuracy testing.

| Designed | | Measured | | Error | |
|---|---|---|---|---|---|
| x | y (mm) | x (mm) | y (mm) | x (mm) | y (mm) |
| 2 | 2 | 2.04 | 2.11 | 0.04 | 0.11 |
| 2 | 2 | 2.06 | 2.09 | 0.06 | 0.09 |
| 2 | 2 | 2.08 | 2.12 | 0.08 | 0.12 |
| 2 | 2 | 2.11 | 2.12 | 0.11 | 0.12 |
| 2 | 2 | 2.20 | 2.17 | 0.20 | 0.17 |
| 2 | 2 | 2.21 | 2.15 | 0.21 | 0.15 |
| 2 | 2 | 2.14 | 2.08 | 0.14 | 0.08 |
| 2 | 2 | 2.09 | 2.08 | 0.09 | 0.08 |
| 2 | 2 | 2.10 | 2.10 | 0.10 | 0.10 |
| 2 | 2 | 2.13 | 2.14 | 0.13 | 0.14 |
| 2 | 2 | 2.17 | 2.15 | 0.17 | 0.15 |
| 2 | 2 | 2.13 | 2.14 | 0.13 | 0.14 |
| 2 | 2 | 2.13 | 1.98 | 0.13 | -0.02 |
| 2 | 2 | 2.14 | 2.13 | 0.14 | 0.13 |
| 2 | 2 | 2.08 | 2.13 | 0.08 | 0.13 |
| 2 | 2 | 2.14 | 2.12 | 0.14 | 0.12 |
| 2 | 2 | 2.16 | 2.12 | 0.16 | 0.12 |
| 2 | 2 | 2.14 | 2.14 | 0.14 | 0.14 |
| 2 | 2 | 2.13 | 2.15 | 0.13 | 0.15 |
| 2 | 2 | 2.18 | 2.05 | 0.18 | 0.05 |
| 2 | 2 | 2.04 | 2.04 | 0.04 | 0.04 |
| 2 | 2 | 2.02 | 2.00 | 0.02 | 0.00 |
| 2 | 2 | 2.12 | 2.14 | 0.12 | 0.14 |
| 2 | 2 | 2.03 | 2.08 | 0.03 | 0.08 |
| 2 | 2 | 2.09 | 2.15 | 0.09 | 0.15 |
| 2 | 2 | 2.15 | 2.14 | 0.15 | 0.14 |
| 2 | 2 | 2.06 | 2.06 | 0.05 | 0.06 |
| 2 | 2 | 2.09 | 2.09 | 0.09 | 0.09 |
| 2 | 2 | 2.08 | 2.10 | 0.08 | 0.09 |
| 2 | 2 | 2.12 | 2.09 | 0.12 | 0.09 |
| 2.5 | 2.5 | 2.55 | 2.62 | 0.05 | 0.12 |
| 4 | 2 | 4.10 | 2.27 | 0.09 | 0.27 |
| 4 | 2 | 4.00 | 2.31 | 0.00 | 0.31 |
| 4 | 2 | 3.97 | 2.30 | -0.03 | 0.30 |
| 4 | 2 | 4.08 | 2.23 | 0.07 | 0.23 |
| 4 | 2 | 4.19 | 2.10 | 0.19 | 0.10 |
| 4 | 2 | 4.12 | 2.17 | 0.12 | 0.17 |
| 4 | 2 | 4.11 | 2.14 | 0.11 | 0.14 |
| 4 | 2 | 4.15 | 2.15 | 0.15 | 0.15 |
| 4 | 2 | 4.17 | 2.15 | 0.17 | 0.15 |
| 4 | 2 | 4.12 | 2.17 | 0.12 | 0.17 |
| 4 | 2 | 4.13 | 2.27 | 0.13 | 0.27 |
| 4 | 2 | 4.16 | 2.29 | 0.16 | 0.29 |
| 4 | 2 | 4.12 | 2.21 | 0.12 | 0.21 |
| 4 | 2 | 4.14 | 2.19 | 0.14 | 0.19 |
| 4 | 2 | 4.18 | 2.22 | 0.18 | 0.22 |
| 12 | 12 | 12.34 | 12.15 | 0.34 | 0.15 |
| 12 | 12 | 12.30 | 12.30 | 0.30 | 0.30 |
| 12 | 12 | 12.34 | 12.22 | 0.34 | 0.22 |
| 12 | 12 | 12.31 | 12.21 | 0.31 | 0.21 |
| 12 | 12 | 12.62 | 12.39 | 0.62 | 0.39 |
| 12 | 12 | 12.57 | 12.29 | 0.57 | 0.29 |
| 12 | 12 | 12.47 | 12.27 | 0.47 | 0.27 |
| 12 | 12 | 12.35 | 12.22 | 0.35 | 0.22 |
| 12 | 12 | 12.45 | 12.23 | 0.45 | 0.23 |
| 12 | 12 | 12.44 | 12.27 | 0.44 | 0.27 |
| 12 | 12 | 12.39 | 12.33 | 0.39 | 0.33 |
| 12 | 12 | 12.44 | 12.31 | 0.44 | 0.31 |
| 12 | 12 | 12.41 | 12.20 | 0.41 | 0.20 |
| 12 | 12 | 12.42 | 12.31 | 0.42 | 0.31 |
| 12 | 12 | 12.38 | 12.23 | 0.38 | 0.23 |
| 12 | 12 | 12.42 | 12.26 | 0.42 | 0.26 |

| Designed | | Measured | | Error | |
|---|---|---|---|---|---|
| x<br>(mm) | y<br>(mm) | x<br>(mm) | y<br>(mm) | x<br>(mm) | y<br>(mm) |
| 2.5 | 2.5 | 2.60 | 2.59 | 0.10 | 0.09 |
| 2.5 | 2.5 | 2.55 | 2.66 | 0.04 | 0.16 |
| 2.5 | 2.5 | 2.54 | 2.61 | 0.04 | 0.11 |
| 2.5 | 2.5 | 2.48 | 2.60 | -0.02 | 0.10 |
| 2.5 | 2.5 | 2.48 | 2.57 | -0.02 | 0.07 |
| 2.5 | 2.5 | 2.47 | 2.57 | -0.03 | 0.07 |
| 2.5 | 2.5 | 2.56 | 2.60 | 0.06 | 0.10 |
| 2.5 | 2.5 | 2.52 | 2.54 | 0.02 | 0.04 |
| 2.5 | 2.5 | 2.58 | 2.65 | 0.08 | 0.15 |
| 2.5 | 2.5 | 2.65 | 2.61 | 0.15 | 0.11 |
| 2.5 | 2.5 | 2.59 | 2.59 | 0.09 | 0.09 |
| 2.5 | 2.5 | 2.57 | 2.58 | 0.07 | 0.08 |
| 2.5 | 2.5 | 2.55 | 2.63 | 0.05 | 0.13 |
| 2.5 | 2.5 | 2.61 | 2.66 | 0.11 | 0.16 |
| 2.5 | 2.5 | 2.60 | 2.71 | 0.10 | 0.21 |
| 2.5 | 2.5 | 2.49 | 2.64 | -0.01 | 0.14 |
| 2.5 | 2.5 | 2.48 | 2.56 | -0.02 | 0.06 |
| 2.5 | 2.5 | 2.54 | 2.64 | 0.04 | 0.14 |
| 2.5 | 2.5 | 2.53 | 2.65 | 0.03 | 0.15 |
| 2.5 | 2.5 | 2.57 | 2.64 | 0.07 | 0.14 |
| 2.5 | 2.5 | 2.54 | 2.61 | 0.04 | 0.11 |
| 2.5 | 2.5 | 2.61 | 2.49 | 0.11 | -0.01 |
| 2.5 | 2.5 | 2.54 | 2.60 | 0.04 | 0.10 |
| 2.5 | 2.5 | 2.54 | 2.66 | 0.04 | 0.16 |
| 2.5 | 2.5 | 2.57 | 2.82 | 0.06 | 0.32 |
| 2.5 | 2.5 | 2.49 | 2.61 | -0.01 | 0.11 |
| 2.5 | 2.5 | 2.51 | 2.59 | 0.01 | 0.09 |
| 2.5 | 2.5 | 2.68 | 2.63 | 0.18 | 0.13 |
| 2.5 | 2.5 | 2.70 | 2.63 | 0.20 | 0.13 |
| 2.5 | 2.5 | 2.49 | 2.55 | -0.01 | 0.05 |
| 2.5 | 2.5 | 2.58 | 2.59 | 0.08 | 0.09 |
| 2.5 | 2.5 | 2.70 | 2.73 | 0.20 | 0.23 |
| 2.5 | 2.5 | 2.76 | 2.70 | 0.26 | 0.20 |
| 2.5 | 2.5 | 2.64 | 2.62 | 0.14 | 0.12 |
| 2.5 | 2.5 | 2.62 | 2.73 | 0.12 | 0.23 |
| 2.5 | 2.5 | 2.63 | 2.58 | 0.13 | 0.08 |
| 2.5 | 2.5 | 2.69 | 2.76 | 0.19 | 0.26 |
| 2.5 | 2.5 | 2.65 | 2.59 | 0.15 | 0.09 |
| 2.5 | 2.5 | 2.54 | 2.64 | 0.04 | 0.14 |
| 2.5 | 2.5 | 2.63 | 2.70 | 0.13 | 0.20 |
| 2.5 | 2.5 | 2.60 | 2.69 | 0.10 | 0.19 |
| 2.5 | 2.5 | 2.66 | 2.61 | 0.16 | 0.11 |
| 2.5 | 2.5 | 2.64 | 2.72 | 0.14 | 0.22 |
| 2.5 | 2.5 | 2.67 | 2.68 | 0.17 | 0.18 |
| 2.5 | 2.5 | 2.66 | 2.70 | 0.16 | 0.20 |
| 2.5 | 2.5 | 2.67 | 2.71 | 0.17 | 0.21 |

| Designed | | Measured | | Error | |
|---|---|---|---|---|---|
| x | y<br>(mm) | x<br>(mm) | y<br>(mm) | x<br>(mm) | y<br>(mm) |
| 12 | 12 | 12.47 | 12.27 | 0.47 | 0.27 |
| 12 | 12 | 12.48 | 12.29 | 0.48 | 0.29 |
| 12 | 12 | 12.21 | 12.18 | 0.21 | 0.18 |
| 12 | 12 | 12.45 | 12.32 | 0.45 | 0.32 |
| 12 | 12 | 12.20 | 12.19 | 0.20 | 0.19 |
| 12 | 12 | 12.23 | 12.22 | 0.23 | 0.22 |
| 12 | 12 | 12.40 | 12.24 | 0.40 | 0.24 |
| 12 | 12 | 12.35 | 12.23 | 0.35 | 0.23 |
| 12 | 12 | 12.34 | 12.14 | 0.34 | 0.14 |
| 12 | 12 | 12.38 | 12.27 | 0.38 | 0.27 |
| 12 | 12 | 12.39 | 12.13 | 0.39 | 0.13 |
| 12 | 12 | 12.33 | 12.20 | 0.32 | 0.20 |
| 12 | 12 | 12.32 | 12.26 | 0.32 | 0.25 |
| 12 | 12 | 12.44 | 12.14 | 0.43 | 0.14 |
| 15 | 18 | 14.99 | 18.15 | -0.01 | 0.15 |
| 15 | 18 | 15.14 | 18.20 | 0.14 | 0.20 |
| 15 | 18 | 15.21 | 18.20 | 0.21 | 0.20 |
| 15 | 18 | 15.11 | 18.24 | 0.11 | 0.24 |
| 15 | 18 | 15.21 | 18.27 | 0.21 | 0.27 |
| 15 | 18 | 15.22 | 18.35 | 0.22 | 0.35 |
| 15 | 18 | 15.29 | 18.29 | 0.29 | 0.29 |
| 15 | 18 | 15.28 | 18.30 | 0.28 | 0.30 |
| 15 | 18 | 15.20 | 18.12 | 0.20 | 0.12 |
| 15 | 18 | 15.09 | 18.23 | 0.09 | 0.23 |
| 15 | 18 | 15.12 | 18.46 | 0.12 | 0.46 |
| 15 | 18 | 15.11 | 18.25 | 0.11 | 0.25 |
| 15 | 18 | 15.17 | 18.36 | 0.17 | 0.36 |
| 15 | 18 | 14.99 | 18.39 | -0.01 | 0.39 |
| 15 | 18 | 15.11 | 18.35 | 0.11 | 0.35 |
| 15 | 18 | 15.22 | 18.33 | 0.22 | 0.33 |
| 15 | 18 | 15.39 | 18.26 | 0.39 | 0.26 |
| 15 | 18 | 15.36 | 18.36 | 0.36 | 0.36 |
| 15 | 18 | 15.32 | 18.34 | 0.32 | 0.34 |
| 15 | 18 | 15.30 | 18.33 | 0.30 | 0.33 |
| 15 | 18 | 15.15 | 18.28 | 0.15 | 0.28 |
| 15 | 18 | 15.23 | 18.45 | 0.23 | 0.45 |
| 15 | 18 | 15.26 | 18.29 | 0.26 | 0.29 |
| 15 | 18 | 15.05 | 18.30 | 0.05 | 0.30 |
| 18 | 30 | 18.34 | 30.38 | 0.34 | 0.38 |
| 18 | 30 | 18.06 | 30.25 | 0.06 | 0.25 |
| 18 | 30 | 18.14 | 30.46 | 0.14 | 0.46 |
| 18 | 30 | 18.34 | 30.40 | 0.34 | 0.40 |
| 18 | 30 | 17.97 | 30.27 | -0.03 | 0.27 |
| 18 | 30 | 18.09 | 30.13 | 0.09 | 0.13 |
| 18 | 30 | 18.10 | 30.15 | 0.10 | 0.15 |
| 18 | 30 | 18.12 | 30.41 | 0.12 | 0.41 |

| Designed | | Measured | | Error | |
|---|---|---|---|---|---|
| x (mm) | y (mm) | x (mm) | y (mm) | x (mm) | y (mm) |
| 2.5 | 2.5 | 2.64 | 2.58 | 0.14 | 0.08 |
| 2.5 | 2.5 | 2.64 | 2.68 | 0.14 | 0.18 |
| 2.5 | 2.5 | 2.70 | 2.74 | 0.20 | 0.24 |
| 2.5 | 2.5 | 2.63 | 2.63 | 0.13 | 0.13 |
| 2.5 | 2.5 | 2.67 | 2.64 | 0.17 | 0.14 |
| 2.5 | 2.5 | 2.69 | 2.67 | 0.19 | 0.17 |
| 2.5 | 2.5 | 2.65 | 2.69 | 0.15 | 0.19 |
| 2.5 | 2.5 | 2.74 | 2.71 | 0.24 | 0.21 |
| 2.5 | 2.5 | 2.68 | 2.68 | 0.18 | 0.18 |
| 2.5 | 2.5 | 2.66 | 2.67 | 0.16 | 0.17 |
| 2.5 | 2.5 | 2.62 | 2.63 | 0.12 | 0.13 |
| 2.5 | 2.5 | 2.67 | 2.72 | 0.17 | 0.22 |
| 2.5 | 2.5 | 2.67 | 2.68 | 0.17 | 0.18 |
| 2.5 | 2.5 | 2.65 | 2.67 | 0.15 | 0.17 |
| 2.5 | 2.5 | 2.65 | 2.66 | 0.15 | 0.16 |
| 2.5 | 2.5 | 2.61 | 2.71 | 0.11 | 0.21 |
| 2.5 | 2.5 | 2.66 | 2.68 | 0.16 | 0.18 |
| 2.5 | 2.5 | 2.64 | 2.72 | 0.14 | 0.22 |
| 2.5 | 2.5 | 2.62 | 2.68 | 0.12 | 0.18 |
| 2.5 | 2.5 | 2.61 | 2.63 | 0.11 | 0.13 |
| 2.5 | 2.5 | 2.65 | 2.64 | 0.15 | 0.14 |
| 2.5 | 2.5 | 2.65 | 2.66 | 0.15 | 0.16 |
| 2.5 | 2.5 | 2.62 | 2.60 | 0.12 | 0.10 |
| 2.5 | 2.5 | 2.58 | 2.61 | 0.08 | 0.11 |
| 2.5 | 2.5 | 2.62 | 2.60 | 0.12 | 0.10 |
| 2.5 | 2.5 | 2.59 | 2.61 | 0.09 | 0.11 |
| 2.5 | 2.5 | 2.67 | 2.62 | 0.17 | 0.12 |
| 2.5 | 2.5 | 2.67 | 2.61 | 0.17 | 0.11 |
| 2.5 | 2.5 | 2.67 | 2.60 | 0.17 | 0.10 |
| 2.5 | 2.5 | 2.65 | 2.60 | 0.15 | 0.10 |
| 2.5 | 2.5 | 2.69 | 2.57 | 0.19 | 0.07 |
| 4 | 2 | 3.95 | 2.31 | -0.05 | 0.31 |
| 4 | 2 | 4.05 | 2.33 | 0.05 | 0.33 |
| 4 | 2 | 4.02 | 2.25 | 0.02 | 0.25 |
| 4 | 2 | 4.01 | 2.27 | 0.01 | 0.27 |
| 4 | 2 | 4.13 | 2.33 | 0.13 | 0.33 |
| 4 | 2 | 4.05 | 2.26 | 0.05 | 0.26 |
| 4 | 2 | 4.06 | 2.12 | 0.05 | 0.12 |
| 4 | 2 | 4.07 | 2.38 | 0.06 | 0.38 |
| 4 | 2 | 4.04 | 2.35 | 0.04 | 0.35 |
| 4 | 2 | 4.06 | 2.38 | 0.05 | 0.38 |
| 4 | 2 | 4.06 | 2.17 | 0.06 | 0.17 |
| 4 | 2 | 4.07 | 2.20 | 0.07 | 0.20 |
| 4 | 2 | 4.08 | 2.17 | 0.08 | 0.17 |
| 4 | 2 | 4.09 | 2.25 | 0.09 | 0.25 |
| 4 | 2 | 4.13 | 2.34 | 0.13 | 0.34 |

| Designed | | Measured | | Error | |
|---|---|---|---|---|---|
| x (mm) | y (mm) | x (mm) | y (mm) | x (mm) | y (mm) |
| 20 | 20 | 20.09 | 20.33 | 0.09 | 0.33 |
| 20 | 20 | 20.14 | 20.33 | 0.14 | 0.33 |
| 18 | 30 | 18.36 | 30.41 | 0.36 | 0.41 |
| 18 | 30 | 18.33 | 30.40 | 0.33 | 0.40 |
| 18 | 30 | 18.18 | 30.38 | 0.18 | 0.38 |
| 18 | 30 | 18.16 | 30.36 | 0.16 | 0.36 |
| 20 | 20 | 20.17 | 20.30 | 0.17 | 0.30 |
| 20 | 20 | 20.15 | 20.38 | 0.15 | 0.38 |
| 20 | 20 | 20.17 | 20.31 | 0.17 | 0.31 |
| 20 | 20 | 20.19 | 20.38 | 0.19 | 0.38 |
| 20 | 20 | 20.18 | 20.36 | 0.18 | 0.36 |
| 20 | 20 | 20.14 | 20.31 | 0.14 | 0.31 |
| 20 | 20 | 20.19 | 20.34 | 0.19 | 0.34 |
| 20 | 20 | 20.16 | 20.34 | 0.16 | 0.34 |
| 20 | 20 | 20.14 | 20.26 | 0.14 | 0.26 |
| 20 | 20 | 20.14 | 20.25 | 0.14 | 0.25 |
| 20 | 20 | 20.14 | 20.28 | 0.14 | 0.28 |
| 20 | 20 | 20.09 | 20.32 | 0.09 | 0.32 |
| 20 | 20 | 20.09 | 20.26 | 0.09 | 0.26 |
| 20 | 20 | 20.12 | 20.31 | 0.12 | 0.31 |
| 20 | 20 | 20.15 | 20.31 | 0.15 | 0.31 |
| 20 | 20 | 20.16 | 20.26 | 0.16 | 0.26 |
| 20 | 20 | 20.15 | 20.28 | 0.15 | 0.28 |
| 20 | 20 | 20.12 | 20.36 | 0.12 | 0.36 |
| 20 | 20 | 20.14 | 20.25 | 0.14 | 0.25 |
| 20 | 20 | 20.13 | 20.31 | 0.13 | 0.31 |
| 20 | 20 | 20.12 | 20.33 | 0.12 | 0.33 |
| 20 | 20 | 20.11 | 20.28 | 0.11 | 0.28 |
| 20 | 20 | 20.12 | 20.24 | 0.12 | 0.24 |
| 20 | 20 | 20.21 | 20.27 | 0.21 | 0.27 |
| 20 | 20 | 20.11 | 20.14 | 0.11 | 0.14 |
| 20 | 20 | 20.08 | 20.14 | 0.08 | 0.14 |
| 20 | 20 | 20.10 | 20.23 | 0.10 | 0.23 |
| 20 | 20 | 20.19 | 20.14 | 0.19 | 0.14 |
| 20 | 20 | 20.14 | 20.27 | 0.14 | 0.27 |
| 20 | 20 | 20.23 | 20.30 | 0.23 | 0.30 |
| 20 | 20 | 20.27 | 20.18 | 0.27 | 0.18 |
| 20 | 20 | 20.16 | 20.22 | 0.16 | 0.22 |
| 20 | 20 | 20.29 | 20.25 | 0.29 | 0.25 |
| 20 | 20 | 20.24 | 20.19 | 0.24 | 0.19 |
| 35 | 43 | 35.14 | 43.25 | 0.14 | 0.25 |
| 35 | 43 | 35.32 | 43.36 | 0.32 | 0.36 |
| 35 | 43 | 35.42 | 43.30 | 0.42 | 0.30 |
| 35 | 43 | 35.14 | 43.26 | 0.14 | 0.26 |
| 35 | 43 | 35.38 | 43.24 | 0.38 | 0.24 |
| 35 | 43 | 35.38 | 43.36 | 0.38 | 0.36 |

# Appendix C

Table C1 summarizes the measurement obtained during the dynamometer calibration. Sixteen known weights, ranging from 0.8 kg to 4.798 kg were hung and the resulting voltage signals were recorded.

Appendix C1: Dynamometer calibration data

| Applied | | | Y-axis Measured | | | X-axis Measured | | |
|---|---|---|---|---|---|---|---|---|
| Mass (kg) | Force (N) | Volt (V) | Volt (V) | Force (N) | Accuracy (%) | Volt (V) | Force (N) | Accuracy (%) |
| 0.800 | 7.848 | 0.157 | 0.141 | 7.030 | 10.423% | 0.141 | 7.050 | -0.284% |
| 1.190 | 11.674 | 0.233 | 0.222 | 11.095 | 4.959% | 0.203 | 10.158 | 8.450% |
| 1.300 | 12.753 | 0.255 | 0.241 | 12.030 | 5.669% | 0.231 | 11.563 | 3.886% |
| 1.690 | 16.579 | 0.332 | 0.297 | 14.845 | 10.458% | 0.309 | 15.470 | -4.210% |
| 1.800 | 17.658 | 0.353 | 0.325 | 16.250 | 7.974% | 0.325 | 16.253 | -0.015% |
| 2.190 | 21.484 | 0.430 | 0.388 | 19.375 | 9.816% | 0.388 | 19.375 | 0.000% |
| 2.300 | 22.563 | 0.451 | 0.428 | 21.408 | 5.121% | 0.425 | 21.253 | 0.724% |
| 2.690 | 26.389 | 0.528 | 0.481 | 24.065 | 8.806% | 0.488 | 24.378 | -1.299% |
| 2.800 | 27.468 | 0.549 | 0.513 | 25.625 | 6.710% | 0.516 | 25.783 | -0.615% |
| 3.190 | 31.294 | 0.626 | 0.569 | 28.440 | 9.120% | 0.571 | 28.525 | -0.299% |
| 3.298 | 32.353 | 0.647 | 0.616 | 30.783 | 4.855% | 0.594 | 29.688 | 3.557% |
| 3.688 | 36.179 | 0.724 | 0.704 | 35.175 | 2.776% | 0.696 | 34.775 | 1.137% |
| 3.798 | 37.258 | 0.745 | 0.742 | 37.100 | 0.425% | 0.735 | 36.725 | 1.011% |
| 4.188 | 41.084 | 0.822 | 0.774 | 38.675 | 5.864% | 0.735 | 36.725 | 5.042% |
| 4.298 | 42.163 | 0.843 | 0.805 | 40.250 | 4.538% | 0.821 | 41.025 | -1.925% |
| 4.798 | 47.068 | 0.941 | 0.938 | 46.875 | 0.411% | 0.914 | 45.700 | 2.507% |

Table C2 summarizes the average cutting forces measured directly from the oscilloscope, adjusted using Equation (4.12) and (4.13), and adjusted and low-pass filtered. All the tests were conducted using the 2.381 mm (3/32") diameter tungsten carbide flat-end mill on the 3-axis CNC unit as described in Section 4.4.

Appendix C2: Average cutting forces.

| Layer | c (mm/min) | h (mm/tooth) | Measured | | Adjusted | | Adjusted Filtered | |
|---|---|---|---|---|---|---|---|---|
| | | | Fax (N) | Fay (N) | Fax (N) | Fay (N) | Fax (N) | Fay (N) |
| 1 | 200 | 0.0400 | - | - | - | - | - | - |
| 1 | 150 | 0.0300 | - | - | - | - | - | - |
| 1 | 100 | 0.0200 | - | - | - | - | - | - |

| | | | | | | | | |
|---|---|---|---|---|---|---|---|---|
| 1 | 75 | 0.0150 | -1.8815 | 3.0341 | -1.9085 | 3.0809 | -1.904 | 3.0829 |
| 1 | 50 | 0.0100 | -3.2596 | 4.1668 | -3.3219 | 4.2216 | -3.3264 | 4.2106 |
| 1a | 200 | 0.0400 | | | | | | |
| 1a | 100 | 0.0200 | -4.3298 | 2.4665 | -4.4196 | 2.5092 | -4.4104 | 2.5118 |
| 1a | 50 | 0.0100 | -2.5205 | 2.2099 | -2.5639 | 2.2507 | 2.5685 | 2.2532 |
| 2 | 200 | 0.0400 | -6.176 | 17.8533 | -6.3131 | 18.0076 | -6.3307 | 17.994 |
| 2 | 150 | 0.0300 | -12.3488 | 12.3146 | -12.6442 | 12.4287 | -12.6319 | 12.4021 |
| 2 | 100 | 0.0200 | -7.0215 | 6.1557 | -7.1803 | 6.2551 | -7.1855 | 6.2149 |
| 2 | 75 | 0.0150 | -5.413 | 8.975 | -5.5305 | 9.0649 | -5.5304 | 9.081 |
| 2 | 50 | 0.0100 | -4.2992 | 7.8379 | -4.3882 | 7.9195 | -4.3085 | 7.9165 |
| 2a | 200 | 0.0400 | - | - | - | - | - | - |
| 2a | 100 | 0.0200 | -5.371 | 13.4086 | -5.4875 | 13.5306 | -5.5009 | 13.5022 |
| 2a | 50 | 0.0100 | -5.924 | 4.8973 | -6.0547 | 4.7561 | -6.0569 | 4.7855 |
| 3 | 200 | 0.0400 | - | - | - | - | - | - |
| 3 | 150 | 0.0300 | -10.9383 | 17.3225 | -11.1976 | 17.4729 | -11.1932 | 17.4931 |
| 3 | 100 | 0.0200 | -7.5946 | 11.5363 | -7.7681 | 11.6467 | -7.7522 | 11.6716 |
| 3 | 75 | 0.0150 | -3.5617 | 10.2608 | -3.6318 | 10.36 | -3.6407 | 10.361 |
| 3 | 50 | 0.0100 | -8.8313 | 10.9219 | -9.0365 | 11.0259 | -9.0272 | 11.0304 |
| 3a | 200 | 0.0400 | -10.5375 | 13.0211 | -10.7865 | 13.1403 | -10.7785 | 13.1315 |
| 3a | 100 | 0.0200 | -12.0122 | 13.5357 | -12.299 | 13.6586 | -12.2963 | 13.6548 |
| 3a | 50 | 0.0100 | -8.9084 | 4.6332 | -9.1158 | 4.893 | -9.1206 | 4.8933 |
| 4 | 200 | 0.0400 | -3.1884 | 14.5535 | -3.2489 | 14.6838 | -3.2717 | 14.6683 |
| 4 | 150 | 0.0300 | -11.7009 | 12.0464 | -11.9797 | 12.1585 | -11.99 | 12.1894 |
| 4 | 100 | 0.0200 | -8.2921 | 10.8367 | -8.4835 | 10.9401 | -8.475 | 10.9489 |
| 4 | 75 | 0.0150 | -6.5388 | 9.6508 | -6.6852 | 9.7455 | -6.7004 | 9.7033 |
| 4 | 50 | 0.0100 | -4.2784 | 11.7257 | -4.3669 | 11.8356 | -4.3681 | 11.829 |
| 4a | 200 | 0.0400 | -0.49672 | 10.405 | -0.48822 | 10.5053 | -0.50634 | 10.4928 |
| 4a | 100 | 0.0200 | -10.9364 | 10.7034 | -11.1959 | 10.8058 | -11.2154 | 10.7881 |
| 4a | 50 | 0.0100 | -2.9839 | 3.3725 | -3.0391 | 3.4217 | -3.042 | 3.4159 |

Two algorithms were developed in MatLAB to process the measured cutting forces as shown in Table C3 and C4 below.

Table C3: Algorithm used to extract, adjust, and filtered the measured forces from oscilloscope and output the average cutting forces.

```
% ============================================================= %
%                                                               %
% CPP_Avg_F.m      Function to calculate the average milling force   %
%                  It takes data from .CSV files and plot X, Y milling %
%                  forces & output the average forces           %
%                                                               %
% Created By:      Christina Wei
%
% Date created:    Oct 16, 2006                                 %
%                                                               %
```

```
%                                                                    %
% Input:              'FileName.csv'                                 %
%                     Calib_factor                                   %
%                     n (spindle speed)                              %
%                                                                    %
%                                                                    %
% ================================================================== %

clear all;
close all;
clc;

n = 2500;                    % Spindle Speed [rpm]
t2a = n*360/60;              % Convert time to angle [degree/s]
NoRev = 4;                   % No. of revolution [--]
N = 2;
two_tooth_f = N*n/60;        % Tooth pass frequency [Hz]

% Files %
% ================================================================== %
o = cd;
Layer = '1';                 % ENTER layer number
Feed = 200;                  % ENTER feed

FileNo = ['o__', Layer, '__', num2str(Feed), 'fr'];
o = strcat(o,['\',FileNo,'.csv']);

textposx = 120*pi;

textposyx = 30;
textposyy = 30;


% Oscilloscope %
% ================================================================== %
fid = fopen(o);
dummy = fgetl(fid);
check = sscanf(dummy,'%f');
fclose(fid);

fid = fopen(o);
if isempty(check)
    for lines = 1:2
        dummy = fgetl(fid);
```

```
   end
end

oData = fscanf(fid, '%f,%f,%f');
fclose(fid);

oData = reshape(oData,3,length(oData)/3);

% NOTE: the data from oscilloscope is in the order of time, Vy, Vx

otime = oData(1,:)';
Vy = oData(2,:)';
Vx = oData(3,:)';

clear fid dummy check mData;

% Oscillscope Probe 1:1
% Charge Amplifier 1:50 (1-11)
% ---------------------------------------------------------------------- %
calib_factor=50;                    % Calibration factor    [N/V]

Vx_adj = (-Vx + 0.0207) / 0.0195;
Vy_adj = (-Vy + 0.0246) / 0.0199;

Fox_ = calib_factor * Vx;
Foy = calib_factor * Vy;

% Isolate data for NoRev of revolution
% ---------------------------------------------------------------------- %
otStep = ( otime(2)-otime(1) )*t2a;     % angle/time step       [ang]

ioPt = find ( (otime*t2a - (-360+0*NoRev)) <= otStep);
ioPt = length(ioPt);

foPt = find ( (otime*t2a - (-360+360*NoRev)) <= otStep );
foPt = length(foPt);

osample_f = 1/(otime(ioPt)-otime(ioPt-1));

otime = otime(ioPt:foPt);
Fox = Fox(ioPt:foPt);
Foy = Foy(ioPt:foPt);

Fox_adj = Fox_adj(ioPt:foPt);
```

```
Foy_adj = Foy_adj(ioPt:foPt);


% Noise filter
% --------------------------------------------------------------------- %
osample_f = 1/( otime(2)-otime(1) );        % Sample frequency      [Hz] (from data)
fn_o = osample_f / 2;

[b a] = butter(2,5*two_tooth_f/fn_o);
Fox_f = filtfilt(b,a,Fox);
Foy_f = filtfilt(b,a,Foy);

Fox_adj_f = filtfilt(b,a,Fox_adj);
Foy_adj_f = filtfilt(b,a,Foy_adj);


% Average forces
% --------------------------------------------------------------------- %
oFax = sum(Fox)/length(Fox);    % Avg. x force          [N]
oFay = sum(Foy)/length(Foy);    % Avg. y force          [N]

oFax_f = sum(Fox_f)/length(Fox_f);
oFay_f = sum(Foy_f)/length(Foy_f);

oFax_adj = sum(Fox_adj)/length(Fox_adj);
oFay_adj = sum(Foy_adj)/length(Foy_adj);

oFax_adj_f = sum(Fox_adj_f)/length(Fox_adj_f);
oFay_adj_f = sum(Foy_adj_f)/length(Foy_adj_f);


disp(['Oscilloscope Fax = ' num2str(oFax) ' N']);
disp(['Oscilloscope Fay = ' num2str(oFay) ' N']);
disp(['Oscilloscope Fax filtered = ' num2str(oFax_f) ' N']);
disp(['Oscilloscope Fay filtered = ' num2str(oFay_f) ' N']);

disp(['Oscilloscope Fax adjusted = ' num2str(oFax_adj) ' N']);
disp(['Oscilloscope Fay adjusted= ' num2str(oFay_adj) ' N']);
disp(['Oscilloscope Fax adjusted filtered = ' num2str(oFax_adj_f) ' N']);
disp(['Oscilloscope Fay adjusted filtered = ' num2str(oFay_adj_f) ' N']);

% ============================================================ %
figure;
subplot(2,1,1);
```

```
plot (otime*t2a, Fox, 'm', otime*t2a, Fox_f, 'b', otime*t2a, Fox_adj, 'k', otime*t2a,
Fox_adj_f, 'r', 'linewidth',1);

ylabel ('Fx [N]');

title(strcat([Layer, ', ', num2str(Feed), ' mm/min']));

text(textposx,textposyx,...
      ['un f = ',num2str(oFax), '  f = ', num2str(oFax_f),...
      '  adj = ', num2str(oFax_adj), '  adj f = ', num2str(oFax_adj_f) ],...
      'HorizontalAlignment','center',...
      'BackgroundColor',[.7 .9 .7]);

legend('Unfiltered','Filtered', 'Adjusted', 'Adjusted Filtered', 'Orientation','horizontal');

subplot(2,1,2);
plot (otime*t2a, Foy, 'm', otime*t2a, Foy_f, 'b', otime*t2a, Foy_adj, 'k', otime*t2a,
Foy_adj_f, 'r', 'linewidth',1);

text(textposx, textposyy,...
      ['un f = ',num2str(oFay), '  f = ', num2str(oFay_f),...
      '  adj = ', num2str(oFay_adj), '  adj f = ', num2str(oFay_adj_f) ],...
      'HorizontalAlignment','center',...
      'BackgroundColor',[.7 .9 .7]);

ylabel ('Fy [N]');
xlabel ('Angle [deg]');
```

Table C4: Algorithm used to compute $K_{tc}$, $K_{rc}$, $K_{te}$, and $K_{re}$. Based on these coefficients, forces were predicted using the code below as well as using CutPRO. A graph is outputted to display the actual and predicted forces.

```
% ========================================================== %
%                                                            %
% CPP_Avg_F.m       Function to calculate the average milling force   %
% CPP.m             Function to calculate Ktc, Krc, Kte, Kre based on  %
%                   the average x and y forces.              %
%                                                            %
% Created By:       Christina Wei                            %
% Date:             Oct 16, 2006                             %
%                                                            %
% Input:                                                     %
```

```
%                                                                          %
%                   Faxc, Faxe, Fayc, Faye                                 %
%                   Tool parameters: a, N, D, A, feed, n                   %
%                   FileN                                                  %
%                   Cailb_factor                                           %
%                   Select plotting scale (Time or Angle)                  %
%                                                                          %
% ======================================================================== %

% clear all;
close all;
clc;

NoRev = 4;              % No. of Revolution       [--]
r2d = 180/pi;           % Convert radian to deg    [deg/rad]
d2r = pi/180;           % Convert deg to radian    [rad/deg]

% Menu for input
% ======================================================================== %
methods = 0;
while (methods ~= 4)
  methods = input(strcat('MENU \n',...
                '1) Cutting force coefficients \n',...
                '2) Tool Geometry \n',...
                '3) Cutting Conditions \n',...
                '4) None \n\nInput: '));

  switch(methods)
    case(1)
      % Cutting force coefficients

      Faxc = input('Faxc, Average x cutting force coefficient [N]: ');
      Faxe = input('Faxe, Average x edge force coefficient [N/mm): ');
      Fayc = input('Fayc, Average y cutting force coefficient [N]: ');
      Faye = input('Faye, Average y edge force coefficient [N/mm): ');

    case(2)
      %Tool Geometry

      D = input('Diameter [mm]: ');
      N = input('Number of flutes [-]: ');
      n = input('Spindle speed [rpm]: ');

    case(3)
```

```
        % Cutting conditions

        calib_factor = input('Calibraiton factor [N/V]: ');
    end
end

layer = input('Cutting layer (e.g. 1, 2, 3, 1a..): ', 's');
feed = input('Feedrate [mm/min]: ');
offsetx = input('Offset in Osc x [ang]: ');
offsety = input('Offset in Osc y [ang]: ');

t2a = n*360/60;
two_tooth_f = N*n/60;              % 2 x tooth passing frequency [Hz]

% Calculate Ktc, Kte, Krc, Kre
% ============================================================ %
phi_st = 0*d2r;                 % Start angle [rad]
phi_ex = 180*d2r;               % Exit angle [rad]

A = D/2;                        % Axial depth of cut [mm]

P = A*N/(2*pi)*(cos(2*phi_ex)-cos(2*phi_st));
Q = A*N/(2*pi)*((2*phi_ex-sin(2*phi_ex))-(2*phi_st - sin(2*phi_st)));
S = A*N/(2*pi)*(sin(phi_ex)-sin(phi_st));
T = A*N/(2*pi)*(cos(phi_ex)-cos(phi_st));

Ktc = 4*(Faxc*P + Fayc*Q)/(P^2 + Q^2);  % [N/mm^2]
Krc = (Ktc*P - 4*Faxc)/Q;               % [N/mm]
Kte = -(Faxe*S + Faye*T)/(S^2 + T^2);   % [N/mm^2]
Kre = (Kte*S + Faxe)/T;                 % [N/mm]

if Kte < 0;
   Kte = 0;
end

if Kre < 0;
   Kre = 0;
end

disp(['Ktc = ' num2str(Ktc) ' N/mm^2']);
disp(['Kte = ' num2str(Kte) ' N/mm']);
disp(['Krc = ' num2str(Krc) ' N/mm^2']);
disp(['Kre = ' num2str(Kre) ' N/mm']);
```

```
% Oscilliscope
% ============================================================ %
o = cd;
o = strcat(o,['\o__L',layer,'__',num2str(feed),'fr.csv']);

fid1 = fopen(o);
dummy = fgetl(fid1);
check = sscanf(dummy, '%f');
fclose(fid1);

fid1 = fopen(o);
if isempty(check)
   for lines = 1:2
      dummy = fgetl(fid1);
   end
end

oData = fscanf(fid1, '%f, %f, %f');
fclose(fid1);

oData = reshape(oData, 3, length(oData)/3);
otime = oData(1,:)';
Vx = oData(3,:)';
Vy = oData(2,:)';

clear fid1 dummy check oData;

Vx_adj = (-Vx + 0.0207) / 0.0195;
Vy_adj = (-Vy + 0.0246) / 0.0199;

Fox_ = calib_factor * Vx;
Foy = calib_factor * Vy;


% noise filter @ 5 x tooth passing frequency %
% ---------------------------------------------------------------------- %
osamplef = 1 / ( otime(2) - otime(1) );    % oscilloscope sample freq [Hz]
fn_o = osamplef / 2;

[b a] = butter (2, 5*two_tooth_f/fn_o);
Fox = filtfilt (b,a,Fox);
Foy = filtfilt (b,a,Foy);
```

```
% Isolate data for NoRev of revolution
% ---------------------------------------------------------------------- %
otStep = ( otime(2)-otime(1) )*t2a;     % angle/time step       [ang]

ioPt = find ( (otime*t2a - (-360+0*NoRev)) <= otStep);
ioPt = length(ioPt);

foPt = find ( (otime*t2a - (-360+360*NoRev)) <= otStep );
foPt = length(foPt);

otime = otime(ioPt:foPt);
Fox = Fox(ioPt:foPt);
Foy = Foy(ioPt:foPt);


% MatLAB Simulated Forces
% ==================================================================== %
% Cutting Condition Inputs
% ---------------------------------------------------------------------- %
% Tool Geometry
beta = 30*(pi/180);             % Helix angle [rad]
c = feed/n/N;                   % Feed per tooth [mm/tooth]

% Start/Exit angle
phi_st = 0*d2r;                 % start angle [rad]
phi_ex = 180*d2r;               % full immersion

% ---------------------------------------------------------------------- %
% Intergraion Constant
delta_phi = 1*d2r;              % Integration angle [rad]
delta_a = A/500;                % Integration height [mm]

% Force Calculation
V = pi*D*n/60;                  % Cutting force [mm/s]
phi_p = 2*pi/N;                 % Pitch angle [rad]
K = 6*pi/delta_phi;             % No. angular increment [-]
L = A/delta_a;                  % No. vertical increment [-]

% Angular Integration Loop
for i = 1:K

   phi(i) = phi_st + i*delta_phi;
   Fsx(i) = 0.0;
```

```
   Fsy(i) = 0.0;
   Fst(i) = 0.0;

   for k=1:N
      phi_1 = mod(phi(i) + (k-1)*phi_p, 2*pi);
      phi_2 = phi_1;

      for j=1:L
         a(j) = j*delta_a;
         phi_2 = mod(phi_1 - (2*tan(beta)/D)*a(j), 2*pi);

         if (phi_st <= phi_2) & (phi_2 <= phi_ex);

            h = c*sin(phi_2);

            dFt = delta_a*(Ktc*h + Kte);
            dFr = delta_a*(Krc*h + Kre);
            dFx = -dFt*cos(phi_2) - dFr*sin(phi_2);
            dFy = dFt*sin(phi_2) - dFr*cos(phi_2);

            Fsx(i) = Fsx(i) + dFx;
            Fsy(i) = Fsy(i) + dFy;
            Fst(i) = Fst(i) + dFt;

         end
      end
   end
end



% CutPRO Simulated force
% =========================================================== %
cp = cd;
cp = strcat(cp, ['\cp__',num2str(feed),'fr__o.dat']);

fid3 = fopen(cp);
cpData = fscanf(fid3, '%f %f %f %f %f %f %f %f');
fclose(fid3);

cpData = reshape(cpData, 8, length(cpData)/8);
cptime = cpData(1,:)';
Fcpx = cpData(3,:)';
Fcpy = cpData(4,:)';
```

```
cptStep = ( cptime(2)-cptime(1) )*t2a;      % angle/time step       [ang]

icpPt = find ( (cptime*t2a - 0*NoRev) <= cptStep);
icpPt = length(icpPt)+1;

fcpPt = find ( (cptime*t2a - 360*NoRev) <= cptStep);
fcpPt = length (fcpPt);

cptime = cptime(icpPt:fcpPt);
Fcpx = Fcpx(icpPt:fcpPt);
Fcpy = Fcpy(icpPt:fcpPt);


% Plotting
% ========================================================= %
figure;
subplot(2,1,1);

plot (phi*r2d, Fsx, 'm--', cptime*t2a, Fcpx, 'k:', otime*t2a+360+offsetx, Fox, 'b');
ylabel ('Fx [N]');

title(['L', layer, ', ' num2str(feed) ' mm/min']);

subplot(2,1,2);
plot (phi*r2d, Fsy, 'm--', cptime*t2a, Fcpy, 'k:', otime*t2a+360+offsety, Foy, 'b');
ylabel ('Fy [N]');
xlabel ('Angle [deg]');
legend ('MatLAB Simulated', 'CutPRO', 'Oscilloscope', 'Orientation','horizontal');

clear offsetx offsety;
```

Figure C1 below displays similar data as Figure 4-9 in Section 4.4.4. The figure shows the variation of average cutting forces in the x-direction against varying feed rates and across the cross section of CPP.

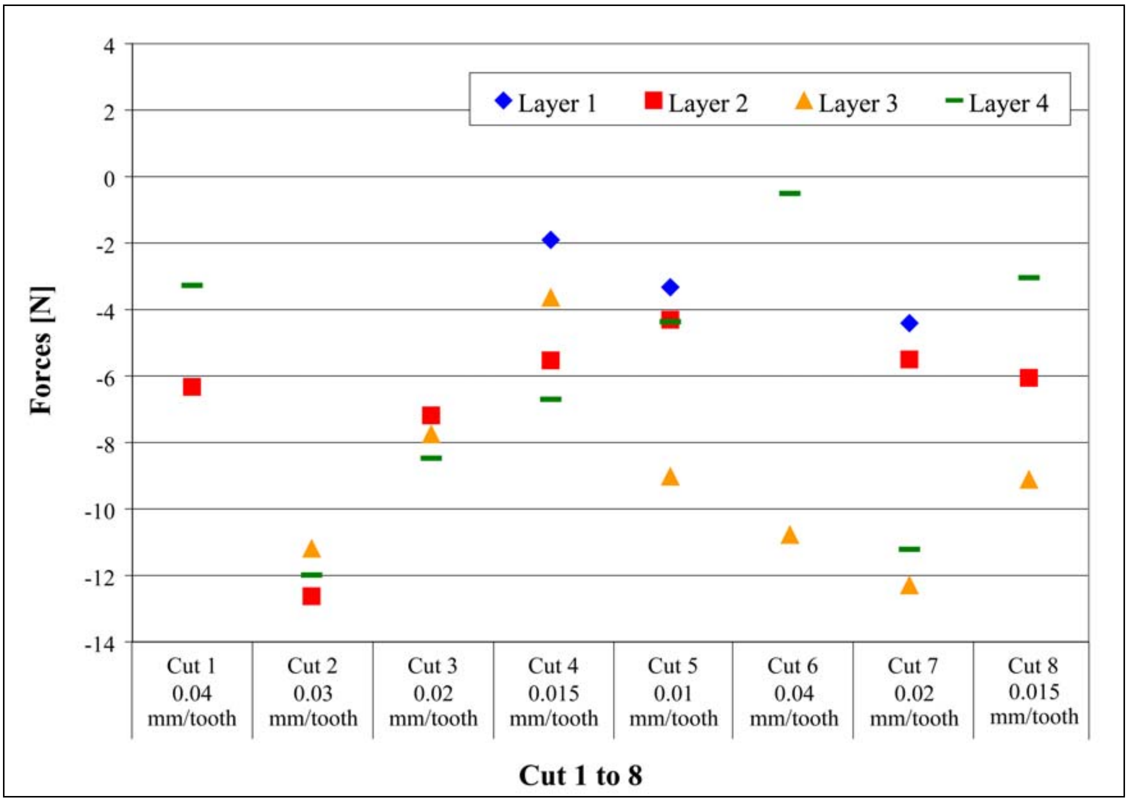

Figure C1: Average x-direction cutting forces showing variation vertically and horizontally across the material blank for cutting 75% dense CPP block at *n* = 2500 rpm and *a* = 1.190625 mm.